Studies on slow gas flows in the near-continuum regime

Carl-Johan Tor Laneryd

2007

Contents

Chapter 1

Introduction

The kinetic theory of gases seeks to explain the physics of heat and mass transfer in gas flows by the translational motion of molecules. Although today the theory has achieved more-or-less universal acceptance as the correct model at a microscopic level, such was not always the case. Even today, the difficulties inherent in a rigorous mathematical approach are daunting, and direct implementation of numerical methods for solving kinetic equations are computationally very expensive. Some might question if these complications are even necessary when considering gas flows in or near the continuum limit. For suitably large length- and time-scales, it might seem reasonable to assume that kinetic effects will be negligible. Thus we can read in a recently published textbook on fluid dynamics [1]:

> Continuum properties may be interpreted as averages of events involving a great number of microscopic particles. The construction of such interpretation falls into the disciplines of statistical thermodynamics (statistical mechanics) and kinetic theory. From time to time we shall discuss some of the simpler microscopic models that are used for continuum events. This aids in a deeper understanding of continuum properties, but in no way does it make the ideas "truer." The fundamental assumptions of continuum mechanics stand by themselves without reference to the microscopic world.

This viewpoint is understandable considering that both Leonhard Euler (1707-83) and George Gabriel Stokes (1819-1903) derived the fundamental governing equations of classical fluid dynamics using a continuum approach. In comparison, it is interesting to note that Jean Baptiste Joseph Fourier (1768-1830) used a model of intermolecular interactions based on the caloric theory of heat when he derived the equation of heat conduction, as did Claude-Louis-Marie-Henri Navier (1785-1836) when he derived the Navier-Stokes equation decades before Stokes. With the demise of the caloric theory of

heat, the continuum approach has reigned supreme to explain slow, steady behaviour of a gas at a macroscopic level. Despite the great success with which the kinetic theory was able to explain the fundamental properties of gases in the mid-ninteenth century, scepticism remained until it was shown through the Chapman-Enskog expansion that the fundamental equations of classical fluid dynamics could be recovered, and even then it did not bring into question the soundness of starting out from continuum assumptions.

However, recent developments in kinetic theory has given strong reason to question the accuracy of the continuum approach as a starting point for investigations on flow behaviour, even in the so-called continuum limit. Before expounding on that point, let us briefly review the history of the kinetic theory of gas and its connection to the classic fluid dynamics.

The history of the kinetic theory of gas might be said to start with Daniel Bernoulli, who formulated an early version of the theory in his *Hydronamica* published in 1738. Although this book was both popular and influential among contemporary scientists, the chapter on kinetic theory was almost completely ignored. A century later researchers working in the field and obtaining remarkable results could not even get their work published in serious scientific journals. Both John Herapath (1790-1868) and John James Waterston (1811-83) submitted significant papers to the Royal Society of London for the Improvement of Natural Knowledge, but were refused publication. Herapath managed to distribute his work by other means, but Waterston's paper lay unpublished for 47 years in the Royal Society's archives before it was finally discovered by Lord Rayleigh.

Prevalent theories about the constitution of matter in the first half of the 19th century were based on the assumption of atoms that were suspended in ether and could not move freely through space. Heat was either considered to be a substance (the caloric theory of heat) or atomic vibrations (the wave theory of heat). An early

accomplishment of Bernoulli's kinetic theory of gases was that it provided an explanation for Boyle's Law, i.e. that pressure is inversely proportional to volume. However, Isaac Newton (1643-1727) had already sketched out an alternative explanation involving repulsive forces between stationary atoms. Even though this description had some serious flaws, it was accepted without question, and thus the explanation provided by kinetic theory did not in itself lead to any further recognition of the kinetic theory. On the other hand, Amedo Avogadro's (1776-1856) observation that equal volumes of different gases contain the same number of molecules could not be adequately explained by the other theories, but it follows directly from kinetic theory. The significance of this evidence was not recognized at the time.

However, the tide was about to change. The experimentalist James Prescott Joule (1818-1889) discovered Herapath's papers and published work building on them. Independently, August Karl Krönig (1822-79) published a short paper on kinetic theory in 1856. Since both Joule and Krönig were already established scientists, this helped the theory become respectable, thus allowing Rudolf Clausius (1822-88), James Clerk Maxwell (1831-79) and Ludwig Boltzmann (1844-1906) to make their important contributions. For example, Clausius came up with the concept of the mean free path, Maxwell introduced the statistical approach and the velocity distribution function, and Boltzmann derived the fundamental transport equation that bears his name.

Early on, even the chief researchers working in the field were not wholly convinced. In the course of his mathematical calculations, Maxwell obtained the startling result that the viscosity and heat conduction coefficient of a gas are independent of pressure. This seemed counterintuitive, and existing experimental evidence did not seem to support it. Nevertheless, Maxwell decided to carry out his own experiments, which rather than refuting the theory turned out to confirm the predictions.

Before Maxwell, researchers in kinetic theory had mainly used the hard-sphere molecular model. Maxwell instead chose a intermolecular force varying with the in-

verse distance to the fifth power. This model is now known as Maxwell molecules. Although Maxwell did provide some experimental justification for this choice, the main reason was to simplify the mathematical calculations. Incidentally, the restriction to inverse 5th-power intermolecular forces prevented the scientists of the nineteenth century to discover the important physical phenomena of thermal diffusion, i.e. diffusion in a gas mixture caused by a temperature gradient, because the relevant coefficient turns out to be zero for Maxwell molecules. Thermal diffusion was later discovered by Enskog and Chapman.

The mounting evidence in favor of the kinetic theory convinced the scientific establishment that there was some truth in it. However, a countermovement also arose that preferred a positivistic, phenomenological approach. With the discovery of the electron and the advent of quantum mechanics, many scientists became convinced that nothing useful could be gained by studying kinetic theory until the properties of atoms were better understood. Some distinguished researchers like Ernst Mach (1838-1916) and Wilhelm Ostwald (1853-1952) even opposed atomism itself.

It would prove to be just a temporary setback for kinetic theory. With the discovery of Brownian motion, there was no longer any reasonable doubt about the validity of the atomic hypothesis. Progress in the theory of integral equations also opened the path for important results in connecting the kinetic theory of gases with the accepted equations of fluid mechanics. David Hilbert (1862-1943) introduced an expansion of the velocity distribution function and the macroscopic variables in a power-series of the Knudsen number that made it possible to recover the Euler equation. David Enskog (1884-1947) and Sydney Chapman (1888-1970) independently developed another expansion that yielded the Euler equations at the leading order, the compressible Navier-Stokes equations at the second order, and the Burnett equations at the third order.

Now that a connection between the kinetic theory of gases and classical fluid-dynamic equations had been proven, it might have been tempting to jump to the conclusion that kinetic theory is useful at small length scales, but unnecessary in the continuum limit. However, that would leave some important questions about the expansions left unanswered. For example, is it obvious that the expansion should be cut off at the Navier-Stokes level, rather than going to higher order (ignoring for the moment potential pitfalls inherent in these higher order equations)? To answer that question it is helpful to consider the specific physical problem first from a kinetic point of view, identify the appropriate scaling of the physical variables, and on that basis carry out the expansion.

Acting on that strategy, research in the kinetic theory of gases during the latter part of the twentieth century once again produced a startling result. Under some circumstances, slow flows that would vanish in the continuum limit could still produce a finite effect on the behaviour of the gas in this limit. This has been dubbed *ghost effect*, to illustrate the point that something unseen is somehow influencing the world around us.

However, this fluid-dynamic-type system derived through the systematic asymptotic analysis of the Boltzmann equation has additional usefulness. For slightly rarefied gases, the flow is slow but quantifiable. In microflows the geometric length scales become comparable to the mean free path of the gas molecules, and rarefaction effects such as thermal creep or thermal diffusion can be employed in the design of devices such as gas separators or pumps without moving parts. Although it would certainly be preferable to implement a numerical solution scheme based directly on the kinetic theory without taking the extra step through asymptotic theory and the continuum limit, the computational power that is currently available sets strict limitations on how much can be achieved using this approach. By applying the fluid-dynamic-system, the computational requirements can be reduced by several orders of magnitude. The

important point here is that the fluid-dynamic-type system has been derived taking into account kinetic effects from the very beginning. An approach taking the Navier-Stokes equation as its starting point and just adding empirically obtained boundary conditions does not yield correct results.

In the present study we will describe the correct fluid-dynamic-systems for slow, steady flows in a slightly rarefied gas or mixture of gases, enclosed in a channel with large temperature and density variations on the boundary, and no imposed pressure gradient. We will explain how the fluid-dynamic-type equations with the relevant boundary conditions has been obtained through systematic asymptotic analysis of the Boltzmann equation. We will discuss the similarity between these fluid-dynamic-type systems and the incompressible Navier-Stokes set of equations, and we will present a numerical solution method of this system based on the finite volume method and the well-known SIMPLE algorithm, which allows us to quickly obtain results even for complicated geometries. We will do all of this first for a single-component gas (chapter 2), and then for a binary gas mixture consisting of a vapor and a noncondensable gas (chapter 3). Finally, we will also show the close correspondence between the solutions of our fluid-mechanic-type system, and solutions obtained by direct simulation Monte Carlo at vastly higher computational expense.

References

[1] Panton, R. L. *Incompressible Flow*, (John Wiley & Sons, Hoboken, 2005).

[2] Brush, S. G. *The Kind of Motion We Call Heat*, (North-Holland, Amsterdam, 1976).

[3] Y. Sone, *Kinetic Theory and Fluid Dynamics*, Modeling and Simulation in Science, Engineering and Technology (Birkhäuser, Boston, 2002).

[4] C. Cercignani, *The Boltzmann Equation and Its Applications*, (Springer-Verlag, Berlin, 1988).

[5] J. D. Anderson, *A History of Aerodynamics*, (Cambridge University Press, Cambridge, 1997).

Chapter 2

Thermal creep of a slightly rarefied gas through a channel with curved boundary

2.1 Introduction

Thermal creep is a flow of a slightly rarefied gas caused by the temperature gradient along a wall. Although it is one of the classical phenomena in rarefied gas dynamics [1, 2], its importance was revived in recent years in connection with micro gas flows [3]. It is often analyzed by using the incompressible Navier–Stokes equations with the velocity slip in proportion to the temperature gradient along the wall. However, in order to derive correct fluid-dynamic-type systems, one has to carry out a systematic asymptotic analysis of the Boltzmann kinetic system for small Knudsen numbers based on a careful parameter setting [4]. For instance, when the temperature variation along the wall is large (more precisely, when the maximum temperature difference divided by a reference temperature is of the order of unity), some non Navier–Stokes terms should be included in the fluid-dynamic-type equations. The correct fluid-dynamic-type system (fluid-dynamic-type equations, their boundary conditions, and the correction inside the Knudsen layer) describing the thermal creep flow for large temperature variations has been derived in [4]. The aim of the present study is to apply this system to the thermal creep flows, caused by large temperature variations, in a channel with curved boundary. Our interest lies in the possibility of causing one-way flows in a channel with a periodic structure, which are relevant to the Knudsen compressor (cf. [5, 6, 7]).

It should be mentioned that the original purpose of deriving this system in [4] was to show the *ghost effect* in the continuum limit. That is, in spite of the fact that the

flows caused by the effect of gas rarefaction (such as the thermal creep flow) vanish in this limit, their trace has a finite effect on the temperature field in the limit. A series of comprehensive studies of this effect has been performed by Sone and coworkers (see, e.g., [5, 6, 8]).

2.2 Problem and basic equation

Let us consider a rarefied gas inside a channel with a curved wall and with a given temperature distribution (the shape of the channel and the temperature distribution will be specified later). We investigate the behaviour of the gas on the basis of kinetic theory under the following assumptions:

(i) No pressure gradient is imposed in the gas.

(ii) The Knudsen number is small (i.e., the mean free path of the gas molecules is much smaller than any characteristic length in the system, e.g., the distance between the boundaries or the radius of curvature of the boundary).

(iii) The temperature variation along the channel wall is finite (i.e., the maximum temperature difference divided by a reference temperature is of the order of unity).

(iv) The gas molecules are hard spheres and undergo diffuse reflection on the channel wall.

We investigate steady flows in the channel on the basis of the fluid-dynamic-type system that covers the present situation and was derived through systematic asymptotic analysis from the Boltzmann system [4, 6].

We begin by summarizing the main notation to appear in what follows. The symbol X_i denotes the rectangular coordinate system in space, T the temperature, p the pressure, $\rho = p/RT$ the density (where R is the specific gas constant), and v_i the flow velocity.

The reference quantities are denoted by the subscript 0. Let T_0 and p_0 be, respectively, the temperature and pressure of the gas in the reference equilibrium state at rest, $\rho_0 = p_0/RT_0$ the reference density, D_0 the reference length of the system, ℓ_0 the mean free path of the gas molecules at the reference state, and Kn the Knudsen number defined as $\mathrm{Kn} = \ell_0/D_0$. For a hard-sphere gas,

$$\ell_0 = \frac{m_0}{\sqrt{2}\pi d_0^2 \rho_0}, \tag{2.1}$$

where d_0 and m_0 are, respectively, the reference molecular diameter and the reference molecular mass. The symbol n_i denotes the unit normal vector of the boundary pointing into the gas, whereas t_i denotes a tangential vector of the boundary. Furthermore, the temperature of the boundary is denoted by T_{w}.

Then, we introduce the dimensionless quantities:

$$\begin{aligned} x_i &= X_i/D_0, & \hat{T} &= T/T_0, \\ \hat{\rho} &= \rho/\rho_0, & \hat{p} &= p/p_0, \\ \hat{v}_i &= v_i/(2RT_0)^{1/2}, & \hat{T}_{\mathrm{w}} &= T_{\mathrm{w}}/T_0. \end{aligned}$$

Thus $\hat{p} = \hat{\rho}\hat{T}$ holds.

According to [6], the overall behaviour of the gas in the present situation can be described as follows. Any of the macroscopic quantities h of the gas (say, $h = \hat{T}$, $\hat{p}$, $\hat{\rho}$, or $\hat{v}_i$) can be expanded in a power series of a small parameter $\varepsilon = (\sqrt{\pi}/2)\mathrm{Kn}$:

$$h = h_{(0)} + h_{(1)}\varepsilon + h_{(2)}\varepsilon^2 + \cdots, \tag{2.2}$$

where

$$\hat{v}_{i(0)} \equiv 0. \tag{2.3}$$

The equations for the first two terms in the expansion of $\hat{p}$ are simply

$$\frac{\partial \hat{p}_{(0)}}{\partial x_i} = 0, \qquad \frac{\partial \hat{p}_{(1)}}{\partial x_i} = 0. \tag{2.4}$$

The constants $\hat{p}_{(0)}$ and $\hat{p}_{(1)}$ are to be determined from conditions proper to each problem.

The leading nontrivial terms of the expansions ($\hat{T}_{(0)}$, $\hat{\rho}_{(0)}$, $\hat{v}_{i(1)}$, and $\hat{p}_{(2)}$) are governed by the following fluid-dynamic-type equations:

$$\frac{\partial}{\partial x_i}\left(\hat{\rho}_{(0)}\hat{v}_{i(1)}\right) = 0, \tag{2.5a}$$

$$\begin{aligned}\hat{\rho}_{(0)}\hat{v}_{j(1)}\frac{\partial \hat{v}_{i(1)}}{\partial x_j} = & -\frac{1}{2}\frac{\partial \hat{p}_{(2)}}{\partial x_i} + \frac{1}{2}\frac{\partial}{\partial x_j}\left[\hat{\gamma}_1 \hat{T}_{(0)}^{1/2}\left(\frac{\partial \hat{v}_{i(1)}}{\partial x_j} + \frac{\partial \hat{v}_{j(1)}}{\partial x_i} - \frac{2}{3}\frac{\partial \hat{v}_{k(1)}}{\partial x_k}\delta_{ij}\right)\right] \\ & -\frac{1}{2\hat{p}_{(0)}}\frac{\partial}{\partial x_j}\left\{\hat{\gamma}_7\left[\frac{\partial \hat{T}_{(0)}}{\partial x_i}\frac{\partial \hat{T}_{(0)}}{\partial x_j} - \frac{1}{3}\left(\frac{\partial \hat{T}_{(0)}}{\partial x_k}\right)^2\delta_{ij}\right]\right\} \\ & -\frac{1}{2\hat{p}_{(0)}}\frac{\partial}{\partial x_j}\left[\hat{\gamma}_3\hat{T}_{(0)}\left(\frac{\partial^2 \hat{T}_{(0)}}{\partial x_i \partial x_j} - \frac{1}{3}\frac{\partial^2 \hat{T}_{(0)}}{\partial x_k^2}\delta_{ij}\right)\right],\end{aligned} \tag{2.5b}$$

$$\hat{\rho}_{(0)}\hat{v}_{i(1)}\frac{\partial \hat{T}_{(0)}}{\partial x_i} = \frac{1}{2}\frac{\partial}{\partial x_i}\left(\hat{\gamma}_2 \hat{T}_{(0)}^{1/2}\frac{\partial \hat{T}_{(0)}}{\partial x_i}\right), \tag{2.5c}$$

which corresponds to the form given in [4]. The coefficients $\hat{\gamma}_1$, $\hat{\gamma}_2$, $\hat{\gamma}_3$ and $\hat{\gamma}_7$ will in the general case be functions of $\hat{T}_{(0)}$, but for a hard-sphere gas they are constants. Their values are given in Table 2.1.

The thermal stress term contains third-order differential, which in general would require more boundary conditions than those available. However, as is shown in [6], the thermal stress term can be rewritten by introducing the modified pressure $\hat{p}^{\sharp}_{(2)}$

$$\hat{p}^{\sharp}_{(2)} = \hat{p}_{(2)} + \frac{2\hat{\gamma}_3}{3\hat{p}_{(0)}}\frac{\partial}{\partial x_i}\left(\hat{T}_{(0)}\frac{\partial T_{(0)}}{\partial x_i}\right) - \frac{\mathit{\Gamma}_7}{6\hat{p}_{(0)}}\left(\frac{\partial \hat{T}_{(0)}}{\partial x_i}\right)^2, \tag{2.6}$$

with the new coefficient $\mathit{\Gamma}_7$

$$\mathit{\Gamma}_7 = \frac{\mathrm{d}}{\mathrm{d}\hat{T}_{(0)}}\left(\hat{\gamma}_3\hat{T}_{(0)}\right) - \hat{\gamma}_7. \tag{2.7}$$

TABLE 2.1: Value of coefficients for two different molecular models. In this study we make the assumption that we are dealing with a hard-sphere gas, but Eqs. (2.5a)–(2.5c) are valid for more general molecular models, so for comparison the values for the BGK model are also shown.

label	hard-sphere	BGK-model
$\hat{\gamma}_1$	1.270042427	$\hat{T}_{(0)}^{1/2}$
$\hat{\gamma}_2$	1.922284066	$\hat{T}_{(0)}^{1/2}$
$\hat{\gamma}_3$	1.947906335	$\hat{T}_{(0)}$
$\hat{\gamma}_7$	0.189201	$\hat{T}_{(0)}$
$\mathit{\Gamma}_7$	1.758705	$\hat{T}_{(0)}$
$\hat{K}_1$	-0.6463	-0.38316 $\hat{T}_{(0)}^{1/2}$

With these definitions and making use of the assumption that we are dealing with a hard-sphere gas, the momentum equation becomes

$$\begin{aligned}\hat{\rho}_{(0)}\hat{v}_{j(1)}\frac{\partial \hat{v}_{i(1)}}{\partial x_j} &= -\frac{1}{2}\frac{\partial \hat{p}^{\natural}_{(2)}}{\partial x_i} + \frac{\hat{\gamma}_1}{2}\frac{\partial}{\partial x_j}\left[\hat{T}_{(0)}^{1/2}\left(\frac{\partial \hat{v}_{i(1)}}{\partial x_j} + \frac{\partial \hat{v}_{j(1)}}{\partial x_i} - \frac{2}{3}\frac{\partial \hat{v}_{k(1)}}{\partial x_k}\delta_{ij}\right)\right] \\ &\quad + \left[\frac{\mathit{\Gamma}_7}{\hat{\gamma}_2}\frac{\hat{v}_{j(1)}}{\hat{T}_{(0)}^{3/2}}\frac{\partial \hat{T}_{(0)}}{\partial x_j} - \frac{\mathit{\Gamma}_7}{4\hat{p}_{(0)}\hat{T}_{(0)}}\left(\frac{\partial \hat{T}_{(0)}}{\partial x_j}\right)^2\right]\frac{\partial \hat{T}_{(0)}}{\partial x_i}, \qquad (2.8)\end{aligned}$$

which, incidentally, is also valid for the BGK molecular model. The density $\hat{\rho}_{(0)}$ and temperature $\hat{T}_{(0)}$ are related through the equation of state,

$$\hat{\rho}_{(0)} = \frac{\hat{p}_{(0)}}{\hat{T}_{(0)}}. \qquad (2.9)$$

The boundary conditions on the wall for the fluid-dynamic-type equations Eqs. (2.5a)–(2.5c) are obtained by analyzing the Knudsen layer, the thin layer adjacent to the wall with a thickness of the order of the mean free path. The boundary conditions taken from [4] are summarized as follows:

$$\hat{T}_{(0)} = \hat{T}_{\mathrm{w}}, \qquad (2.10a)$$

$$\hat{v}_{i(1)} = -\frac{\hat{K}_1\hat{T}_{\mathrm{w}}^{1/2}}{\hat{p}_{(0)}}\frac{\partial \hat{T}_{\mathrm{w}}}{\partial x_j}(\delta_{ij} - n_i n_j), \qquad (2.10b)$$

with $K_1 = -0.6463$ where δ_{ij} is the Kronecker delta. The constants $p_{(0)}$ and $p_{(1)}$ are to be chosen appropriately in each specific problem [note that $p_{(1)}$ does not affect

Eqs. (2.5a)–(2.5c)].

The solution to the above fluid-dynamic-type system undergoes a correction in the Knudsen layer (a thin layer with thickness of a few mean free paths adjacent to the channel wall), the formula of which is omitted here.

2.3 Numerical method

The fluid-dynamic-type equations (2.5a)–(2.5c) bear a strong resemblance to the incompressible Navier–Stokes set of equations, since there is no obvious equation to solve to obtain the modified pressure $\hat{p}^{\sharp}_{(2)}$ whose gradient appears in the momentum equation. The main differences are that the momentum equation contains an additional term corresponding to thermal stress, $\hat{\rho}_{(0)}$ is not constant, and the boundary condition for $\hat{v}_{i(1)}$ is of slip type. Previous numerical studies of the equations (2.5a)-(2.5c) has used a streamfunction-vorticity finite difference method [4, 9]. In the present study, however, we adopt a finite-volume approach because of its flexibility in application to complex geometries. Following [10] and some other appropriate references, we have adopted the finite-volume method for the incompressible Navier–Stokes system to the present fluid-dynamic-type system.

2.3.A Finite Volume Method

Let us note that Eqs. (2.5b) and (2.5c) can be expressed in the following concise form:

$$\frac{\partial}{\partial x_j}\left(\hat{\rho}_{(0)}\hat{v}_{j(0)}\phi\right) = \frac{\partial}{\partial x_j}\left(\frac{\hat{\gamma}}{2}\hat{T}^{1/2}_{(0)}\frac{\partial \phi}{\partial x_j}\right) + q, \tag{2.11}$$

where ϕ stands for $\hat{T}_{(0)}$ or the individual components of $\hat{v}_{i(1)}$. The values for $\hat{\gamma}$ and q in each case is given in Table 2.2. We call the left-hand side of Eq. (2.11) the convection term and the first term on the right the diffusion term.

We try to solve Eq. (2.11) using the iteration scheme

$$\frac{\partial}{\partial x_j}\left(\hat{\rho}^{m-1}_{(0)}\hat{v}^{m-1}_{j(0)}\phi^{m}\right) = \frac{\partial}{\partial x_j}\left(\frac{\hat{\gamma}}{2}\sqrt{\hat{T}^{m-1}_{(0)}}\frac{\partial \phi^{m}}{\partial x_j}\right) + q^{m-1}, \tag{2.12}$$

under the boundary conditions (2.10) with appropriate discretization. Here, ϕ^m denotes ϕ at the mth iteration, and the superscript $m-1$ means that the variable is evaluated by using $\hat{T}_{(0)}$, $\hat{v}_{i(1)}$, and $\hat{p}^{\sharp}_{(2)}$ at the $(m-1)$th iteration. More specifically, we construct a sequence $\{\phi^1, \phi^2, ...\}$, which is expected to converge, on the basis of Eq. (2.12) with an appropriate initial function ϕ^0 and regard the limit (i.e., ϕ^m with a sufficiently large m) as an approximate solution of Eq. (2.11). Note that Eq. (2.12) is linear in each iteration process.

The computational domain is divided into a number of small control volumes. Let us consider a single control volume Ω with boundary $\partial\Omega$. If we integrate Eq. (2.12) over this control volume, we obtain, after application of Gauss' theorem,

$$\int_{\partial\Omega} \bar{n}_j \hat{\rho}^{m-1}_{(0)} \hat{v}^{m-1}_{j(0)} \phi^m \, \mathrm{d}S = \int_{\partial\Omega} \bar{n}_j \frac{\hat{\gamma}}{2} \sqrt{\hat{T}^{m-1}_{(0)}} \frac{\partial \phi^m}{\partial x_j} \mathrm{d}S + \int_{\Omega} q^{m-1} \, \mathrm{d}V, \tag{2.13}$$

where $\bar{n}_i$ is the outward unit normal vector to the surface $\partial\Omega$, $\mathrm{d}S$ is the surface element on $\partial\Omega$ in the dimensionless x_i space, and $\mathrm{d}V$ is the volume element in the same space. For simplicity, we explain the discretization of Eq. (2.13) in the case of two-dimensional problems (i.e., the problems where the physical quantities are independent of x_3 and $\hat{v}_3 = 0$). The generalization to three-dimensional problems is straightforward.

We consider a two-dimensional control volume Ω (with boundary $\partial\Omega$) depicted in Fig. 2.1. The center of this control volume is denoted by P, and the centers of the

TABLE 2.2: Symbols in the generic convection-diffusion equation, Eq. (2.11).

$\phi =$	$\hat{T}_{(0)}$	$\hat{v}_{i(0)}$
$\hat{\gamma} =$	$\hat{\gamma}_2$	$\hat{\gamma}_1$
$q =$	0	$-\frac{1}{2}\frac{\partial \hat{p}^{\sharp}_{(2)}}{\partial x_i} + \frac{1}{2}\frac{\partial}{\partial x_j}\left(\hat{\gamma}_1 \hat{T}^{1/2}_{(0)} \frac{\partial \hat{v}_{j(0)}}{\partial x_i}\right) - \frac{1}{3}\frac{\partial}{\partial x_i}\left(\hat{\gamma}_1 \hat{T}^{1/2}_{(0)} \frac{\partial \hat{v}_{j(0)}}{\partial x_j}\right) + \left[\frac{\Gamma_7}{\hat{\gamma}_2 \hat{T}^{1/2}_{(0)}} \frac{\hat{v}_{j(0)}}{\hat{T}_{(0)}} \frac{\partial \hat{T}_{(0)}}{\partial x_j} - \frac{\Gamma_7}{4\hat{p}_{(0)}\hat{T}_{(0)}} \left(\frac{\partial \hat{T}_{(0)}}{\partial x_j}\right)^2\right] \frac{\partial T}{\partial x_i}$

neighboring control volumes are denoted by E, W, N and S. The physical quantities are stored at the grid points located at the centers of the control volumes. To save space,

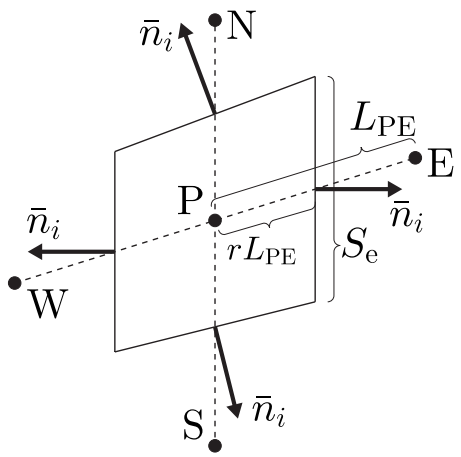

FIGURE 2.1: A control volume.

the method of discretization for the surface integrals in Eq. (2.13) will be described only for the cell face $\partial\Omega_{\mathrm{e}}$ between points P and E, but it is done analogously for other cell faces. We denote by L_{PE} the distance between grid points P and E and by S_{e} the area (the length times the unit width in the x_3 direction) of the surface $\partial\Omega_{\mathrm{e}}$.

The diffusion term is discretized using a central-difference approximation. On a non-cartesian grid, the normal vector at a cell surface does not in general coincide with the line connecting two nodes crossing this surface. On the other hand, we wish to avoid using more node values than necessary for this approximation. This can be achieved by the deferred correction approach suggested by Muzaferija [16]. If ξ_i is the unit vector pointing from node P to node E, then the diffusion term on $\partial\Omega_{\mathrm{e}}$ is approximated as

$$\begin{aligned}\int_{\partial\Omega_{\mathrm{e}}} \bar{n}_j \frac{\hat{\gamma}}{2}\sqrt{\hat{T}^{m-1}_{(0)}}\frac{\partial\phi^m}{\partial x_j}\mathrm{d}S &= S_{\mathrm{e}}\frac{\hat{\gamma}}{2}\left.\sqrt{\hat{T}^{m-1}_{(0)}}\right|_{\mathrm{e}}\frac{\phi^m_{\mathrm{E}}-\phi^m_{\mathrm{P}}}{L_{\mathrm{PE}}} \\ &+ S_{\mathrm{e}}\frac{\hat{\gamma}}{2}\left.\sqrt{\hat{T}^{m-1}_{(0)}}\right|_{\mathrm{e}}(\bar{n}_j-\xi_j)\left(\frac{\partial\phi^{m-1}}{\partial x_j}\right)_{\mathrm{e}}\end{aligned} \tag{2.14}$$

where ϕ^m_{P} and ϕ^m_{E} are the values of ϕ^m at node points P and E, and the subscript e means that the stored value has been interpolated to the cell surface at its intersection

with the line PE. The gradient term $(\partial\phi^{m-1}/\partial x_j)_{\rm e}$ on the surface $\partial\Omega_{\rm e}$ is obtained by interpolation using the corresponding gradient terms at cell centers. The latter terms are computed by taking the average over the control volume, with the integral rewritten using Gauss' theorem so that it can be expressed through grid point values interpolated to cell surfaces. For example, in the x_1-direction we obtain

$$\left(\frac{\partial\phi^{m-1}}{\partial x_1}\right)_{\rm P} = \frac{1}{\Delta\Omega}\int_\Omega \frac{\partial}{\partial x_j}\phi^{m-1}\delta_{1j}{\rm d}\Omega$$
$$= \frac{1}{\Delta\Omega}\int_{\partial\Omega} \phi^{m-1}n_1{\rm d}S. \tag{2.15}$$

Here, $\Delta\Omega$ is the cell volume (the area times the unit width in the x_3-direction in the present two-dimensional case.)

Although technically the central-difference approximation is of only first-order accuracy on a non-uniform grid (and non-uniformness is required because high accuracy demands smaller cells in some parts of the computational domain, e.g. in the vicinity of walls), the approximation is asymptotically of second order, as demonstrated in [10].

The convection term on $\partial\Omega_{\rm e}$ is discretized through linear interpolation,

$$\int_{\partial\Omega_{\rm e}} \bar{n}_j\hat{\rho}^{m-1}_{(0)}\hat{v}^{m-1}_{j(0)}\phi^m\,{\rm d}S = S_{\rm e}\bar{n}_j\left[\hat{\rho}^{m-1}_{(0)}\hat{v}^{m-1}_{j(0)}\right]_{\rm e}\left(r\phi^m_{\rm E} + (1-r)\phi^m_{\rm P}\right), \tag{2.16}$$

where r is a parameter associated with the non-uniformity of the grid ($0 < r < 1$; $r = 0.5$ for a uniform grid), and where the subscript e indicates that the node point values have been interpolated to the point where the line between nodes P and E crosses the cell surface.

The source term in Eq. (2.13) is approximated by taking the values at the grid point multiplied by the cell volume, i.e.,

$$\int_\Omega q^{m-1}\,{\rm d}V = \Delta\Omega\, q^{m-1}_{\rm P}. \tag{2.17}$$

After the discretization described above, Eq. (2.13) can be written on the form

$$a_{\mathrm{P}}^{m-1}\phi_{\mathrm{P}}^{m} = (a_{\mathrm{E}}^{m-1}\phi_{\mathrm{E}}^{m} + a_{\mathrm{W}}^{m-1}\phi_{\mathrm{W}}^{m} + a_{\mathrm{N}}^{m-1}\phi_{\mathrm{N}}^{m} + a_{\mathrm{S}}^{m-1}\phi_{\mathrm{S}}^{m}) + Q^{m-1}, \tag{2.18}$$

where each of the coefficients a_{P}^{m-1}, a_{E}^{m-1}, a_{W}^{m-1}, a_{N}^{m-1}, and a_{S}^{m-1} and the source term B^{m-1} are evaluated by the use of the values of the physical quantities at the previous step [$(m-1)$th step] at the nodes {P, E, W, N, S}. Equation (2.18) is also valid at boundary control volumes if the coefficients a_{E}^{m-1}, ..., a_{S}^{m-1} that correspond to boundary nodes are set to be zero, and the boundary conditions are implemented by incorporating them in Q^{m-1}. Thus the linear system of equations obtained by writing (2.18) for each control volume is closed and can be solved by standard numerical methods. In this way, a discretized solution ϕ^m for the mth step is obtained.

So far we have described how to construct the mth approximation of $\hat{T}_{(0)}$ and $\hat{v}_{i(1)}$ from their $(m-1)$th approximation using Eqs. (2.5c), and (2.8). Now we must also deal with the modified pressure $\hat{p}^{\sharp}_{(2)}$. However, there is no equation dominated by $\hat{p}^{\sharp}_{(2)}$; in fact the only occurrence of $\hat{p}^{\sharp}_{(2)}$ is in the form of a gradient in the momentum equation (2.8). This is a feature that the fluid-dynamic-type equations in this paper share with the incompressible Navier–Stokes equation, so it is suitable to attempt similar solution techniques. A well-known method is the SIMPLE algorithm. In its original formulation [14], it was described for a staggered grid, i.e., flow velocities were stored at cell surfaces rather than cell centers. For complicated geometries, however, it is more suitable to use a colocated grid, i.e., a grid system where all variables are stored at cell centers. A description of how to construct a solution method for a colocated grid in the case of the incompressible Navier–Stokes equation is found in [10].

The main idea is to use the continuity equation, Eq. (2.5a), to derive an equation from which an updated value of $\hat{p}^{\sharp}_{(2)}$ can be obtained. We assume that from the previous step in the iterative process we already have a velocity field $\hat{v}_{i(1)}^{m-1}$ satisfying

continuity, and a corresponding modified pressure field $\hat{p}^{\sharp m-1}_{(2)}$. Using these values to calculate the relevant coefficients and solving the linear algebraic system [Eq. (2.18) with P running all nodes], we obtain a velocity field $\hat{v}^{*}_{i(1)}$ that cannot be expected to satisfy continuity. Therefore we introduce corrections $\hat{p}^{\sharp\prime}_{(2)}$ and $\hat{v}'_{i(1)}$ and set

$$\hat{p}^{\sharp m}_{(2)} = \hat{p}^{\sharp m-1}_{(2)} + \hat{p}^{\sharp\prime}_{(2)}, \tag{2.19a}$$

$$\hat{v}^{m}_{i(1)} = \hat{v}^{*}_{i(1)} + \hat{v}'_{i(1)}. \tag{2.19b}$$

Then, we assume that Eq. (2.5a) is satisfied with $\hat{\rho}_{(0)} = \hat{\rho}^{m-1}_{(0)}$ and $\hat{v}_{i(1)} = \hat{v}^{m}_{i(1)}$ and integrate it over a control volume to obtain

$$\int_{\partial\Omega} \bar{n}_j \, \hat{\rho}^{m-1}_{(0)} \hat{v}^{m}_{j(1)} \, \mathrm{d}S = 0. \tag{2.20}$$

If we assume that there is a relation between the velocity correction and the pressure correction, for example, of the form

$$\hat{v}'_{i(1)} = c \frac{\partial \hat{p}^{\sharp\prime}_{(2)}}{\partial x_i}, \tag{2.21}$$

then we have, from Eqs. (2.19b) and (2.20),

$$0 = c \int_{\partial\Omega} \bar{n}_j \, \hat{\rho}^{m-1}_{(0)} \frac{\partial \hat{p}^{\sharp\prime}_{(2)}}{\partial x_j} \mathrm{d}S + \int_{\partial\Omega} \bar{n}_j \, \hat{\rho}^{m-1}_{(0)} \hat{v}^{*}_{j(1)} \, \mathrm{d}S \tag{2.22}$$

This relation, which is similar to Eq. (2.13), leads to a linear algebraic system for the values of $\hat{p}^{\sharp\prime}_{(2)}$ at the grid points. However, the matrix for the resulting algebraic system is symmetric, and in addition it should be solved with high accuracy in each iteration to ensure convergence, so that in actual implementation it might be more appropriate to use a different solver for the linear algebraic system.

There is some freedom to choose a suitable relation (2.21) because for the converged solution the corrections should all go to zero. However, since we also want the velocity field to satisfy the conservation of momentum, a reasonable choice could be a relation based on the momentum equation. If we insert Eqs. (2.19a) and (2.19b) into the

discretized momentum equation, Eq. (2.18) with $\phi = \hat{v}_{i(1)}$, and neglect the influence of the velocity corrections at the neighbouring nodes, then we have the relation

$$\hat{v}'_{i(1)} = -\frac{\Delta\Omega}{2a_{\mathrm{P}}^{m-1}(\hat{v}_{k(1)})}\frac{\partial \hat{p}^{\sharp\prime}_{(2)}}{\partial x_i}, \tag{2.23}$$

where $a_{\mathrm{P}}^{m-1}(\hat{v}_k)$ indicates a_{P}^{m-1} [see Eq. (2.18)] when $\phi = \hat{v}_k$. Note that a_{P}^{m-1} should be equal for $\hat{v}_{1(1)}$ and $\hat{v}_{2(1)}$ for computational efficiency. In particular, this should be kept in mind in implementation of the boundary conditions. Equation (2.23) is known as the SIMPLE approximation. In the present study, we use Eq. (2.23) as the relation (2.21).

Ideally, the same discretization of the pressure gradient term should be used in both the momentum equation (2.8) and the pressure correction equation (2.22). Unfortunately, doing this on a colocated grid gives rise to oscillations in the pressure field. To avoid these oscillations, the pressure-velocity coupling of Rhie and Chow [15] can be used instead. In that case the velocity field $\hat{v}^*_{j(1)}$ interpolated to cell surfaces is approximated by

$$\begin{aligned}\bar{n}_j \left[v^*_{j(1)}\right]_{\mathrm{e}} \approx{}& \bar{n}_j \left(r \left[v^*_{j(1)}\right]_{\mathrm{E}} + (1-r)\left[v^*_{j(1)}\right]_{\mathrm{P}}\right) \\ &+ \left[\frac{\Delta\Omega}{2a_{\mathrm{P}}^{m-1}(\hat{v}_{k(1)})}\right]_{\mathrm{e}} \xi_j \left(r\left[\frac{\partial p^{\sharp m-1}}{\partial x_j}\right]_{\mathrm{E}} + (1-r)\left[\frac{\partial p^{\sharp m-1}}{\partial x_j}\right]_{\mathrm{P}}\right) \\ &- \left[\frac{\Delta\Omega}{2a_{\mathrm{P}}^{m-1}(\hat{v}_{k(1)})}\right]_{\mathrm{e}} \frac{p_{\mathrm{E}}^{\sharp m-1} - p_{\mathrm{P}}^{\sharp m-1}}{L_{\mathrm{PE}}}\end{aligned} \tag{2.24}$$

The two extra terms smooth out oscillations, and go to zero as the grid is refined.

2.4 Result and discussion

In the present section, we show some results for the thermal creep flow obtained by numerically solving the fluid-dynamic-type system, Eqs. (2.5a), (2.5c) and (2.8), with boundary conditions (2.10). We consider only two-dimensional channels in the (X_1, X_2) plane. We choose ρ_0 in such a way that the average of $\hat{\rho}_{(0)}$ over the computational domain in the x_i-space (see below) is unity.

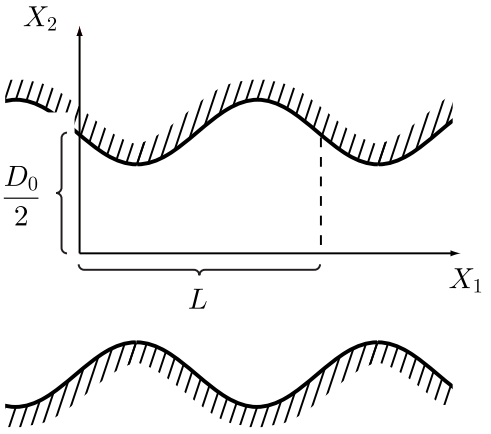

FIGURE 2.2: A sinusoidal channel.

2.4.A One-way flow in a channel with sinusoidal walls

We first consider a gas in a two-dimensional channel with sinusoidal walls located at

$$X_2 = \pm\frac{D_0}{2}\left(1 - \frac{d}{D_0}\sin\frac{2\pi X_1}{L}\right), \tag{2.25}$$

where $0 \le d < D_0$. We assume that the wall temperature, which is common to both walls, has a sinusoidal distribution

$$T_{\rm w} = T_0\left(1 - \hat{T}_{\rm c}\cos\frac{2\pi X_1}{L}\right), \tag{2.26}$$

where $0 < \hat{T}_{\rm c} < 1$. In terms of the dimensionless variables, Eqs. (2.25) and (2.26) become

$$x_2 = \pm\frac{1}{2}\left(1 - \frac{d}{D_0}\sin\frac{2\pi x_1 D_0}{L}\right), \tag{2.27a}$$

$$\hat{T}_{\rm w} = \left(1 - \hat{T}_{\rm c}\cos\frac{2\pi x_1 D_0}{L}\right). \tag{2.27b}$$

When the symmetry and periodicity of the flow field is taken into account, the computational domain can be reduced to the area given by $0 \le x_1 \le L/D_0$ and $0 \le x_2 \le (1/2)\left[1 + (d/D_0)\cos\left(2\pi x_1 D_0/L\right)\right]$, with the periodic condition at $x_2 = 0$ and L/D_0, and the symmetry condition at $x_1 = 0$.

This geometry corresponds to a variant of the Knudsen compressor (see [5, 6, 7]), so that a global unidirectional flow toward the right is expected to be induced when

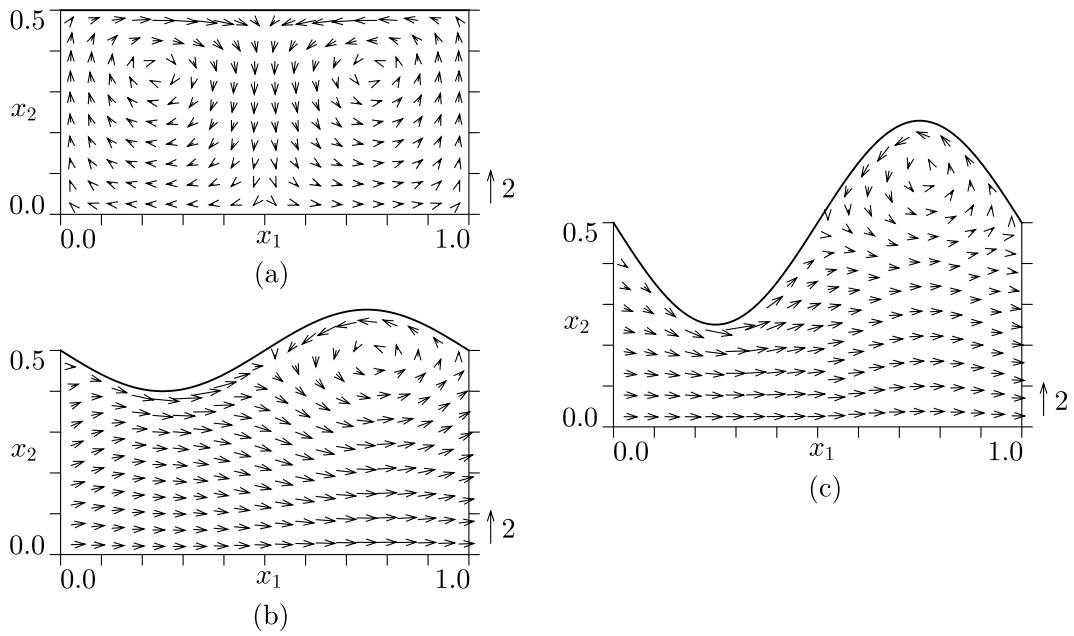

FIGURE 2.3: One-way flow through a channel with sinusoidal walls illustrated through arrows indicating the flow velocity vector $\hat{v}_i$ in the x_1-x_2 plane at their starting point, with the scale shown at the side. All subfigures are drawn for parameter values $L/D_0 = 1$ and $T_c/T_0 = 0.5$, whereas in (a) $d/D_0 = 0.0$, in (b) $d/D_0 = 0.2$, and in (c) $d/D_0 = 0.5$.

$d > 0$. Figures 2.3, 2.4, 2.5, and 2.6 show, respectively, the flow velocity $\hat{v}_{i(1)}$, the isolines of $\hat{T}_{(0)}$, and those of $\hat{p}^{\sharp}_{(2)}$ in the case of $L/D_0 = 1$ and $\hat{T}_c = 0.5$, with d/D_0 taking on the values $\{0, 0.2, 0.5\}$. In Fig. 2.3, the arrow indicates the vector $\hat{v}_{i(1)}$ at its starting point, and its scale is shown in the figure. We will comment on the dotted line in Fig. 2.5 in the last paragraph. Since $\hat{p}^{\sharp}_{(2)}$ (or $\hat{p}_{(2)}$) is determined only up to an additive constant at this stage, the constant in Fig. 2.6 has been chosen in such a way that the average of $\hat{p}^{\sharp}_{(2)}$ over the domain is zero. Therefore, Fig. 2.6 provides only information about the gradient field of $\hat{p}^{\sharp}_{(2)}$. The temperature gradient along the wall is leftward in the wider part and rightward in the narrower part. Therefore, the flow induced along the wall is leftward in the former part and rightward in the latter. However, the resultant flow is rightward in the bulk of the channel, and a counterclockwise circulating flow is formed near the wall in the wider part. Near the point of maximum channel width, there arises a very steep gradient of $\hat{p}^{\sharp}_{(2)}$, which

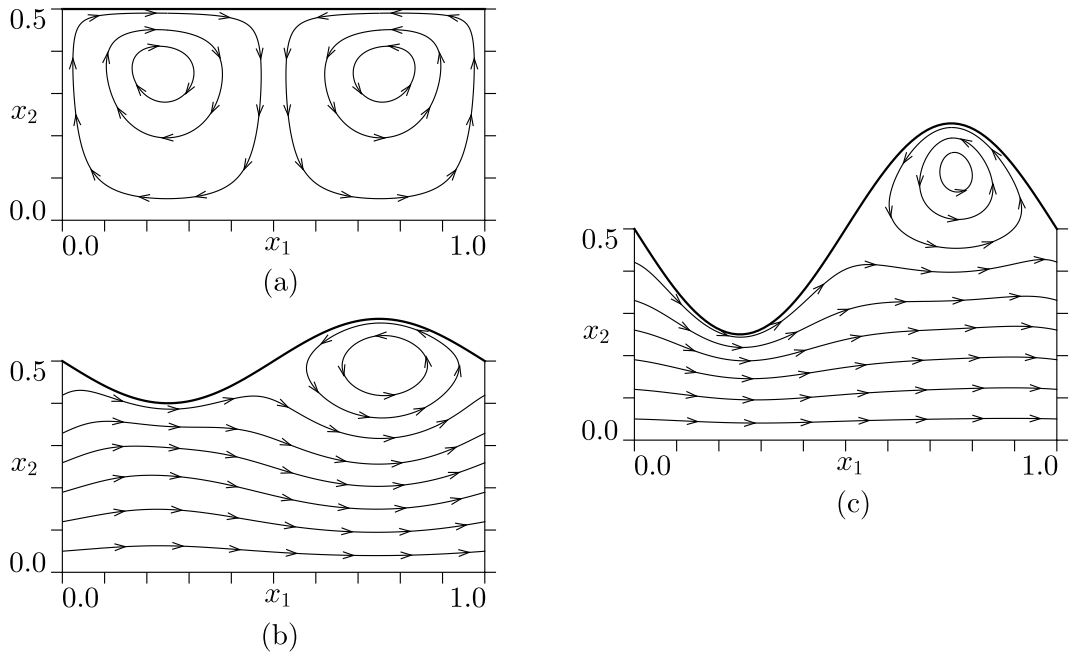

FIGURE 2.4: One-way flow through a channel with sinusoidal walls illustrated through streamlines of the flow velocity $\hat{v}_i$. All subfigures are drawn for parameter values $L/D_0 = 1$ and $T_c/T_0 = 0.5$, whereas in (a) $d/D_0 = 0.0$, in (b) $d/D_0 = 0.2$, and in (c) $d/D_0 = 0.5$.

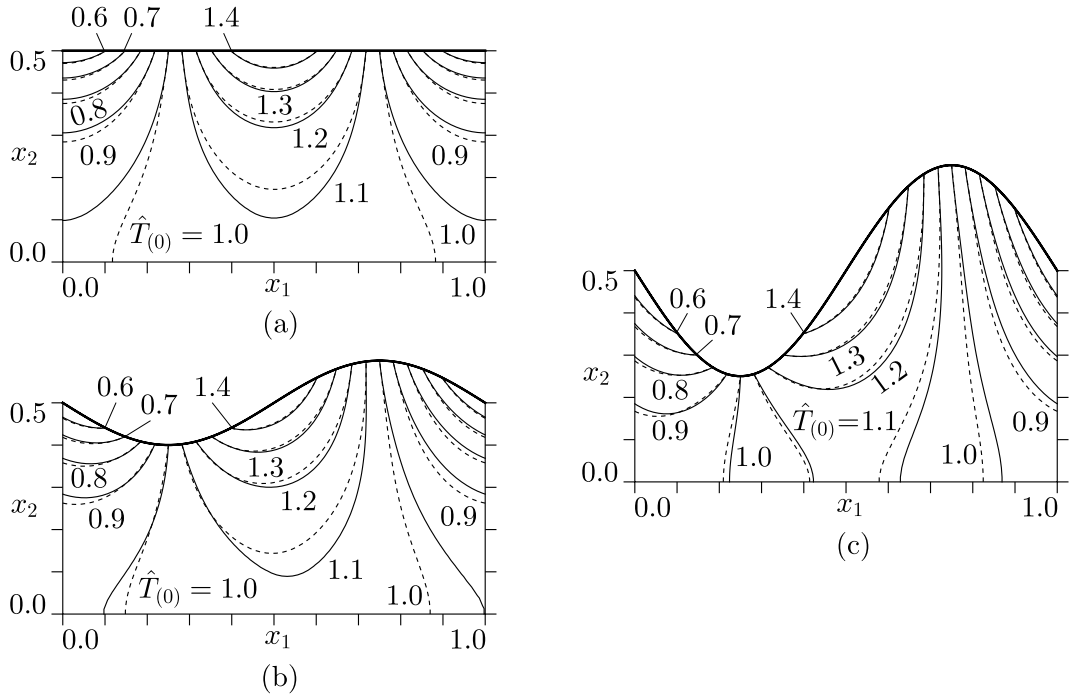

FIGURE 2.5: Temperature field in a channel with sinusoidal walls, represented by a solid line. All subfigures are drawn for parameter values $L/D_0 = 1$ and $T_c/T_0 = 0.5$, whereas in (a) $d/D_0 = 0.0$, in (b) $d/D_0 = 0.2$, and in (c) $d/D_0 = 0.5$. A dashed line is also shown, representing the solution of the heat-conduction equation.

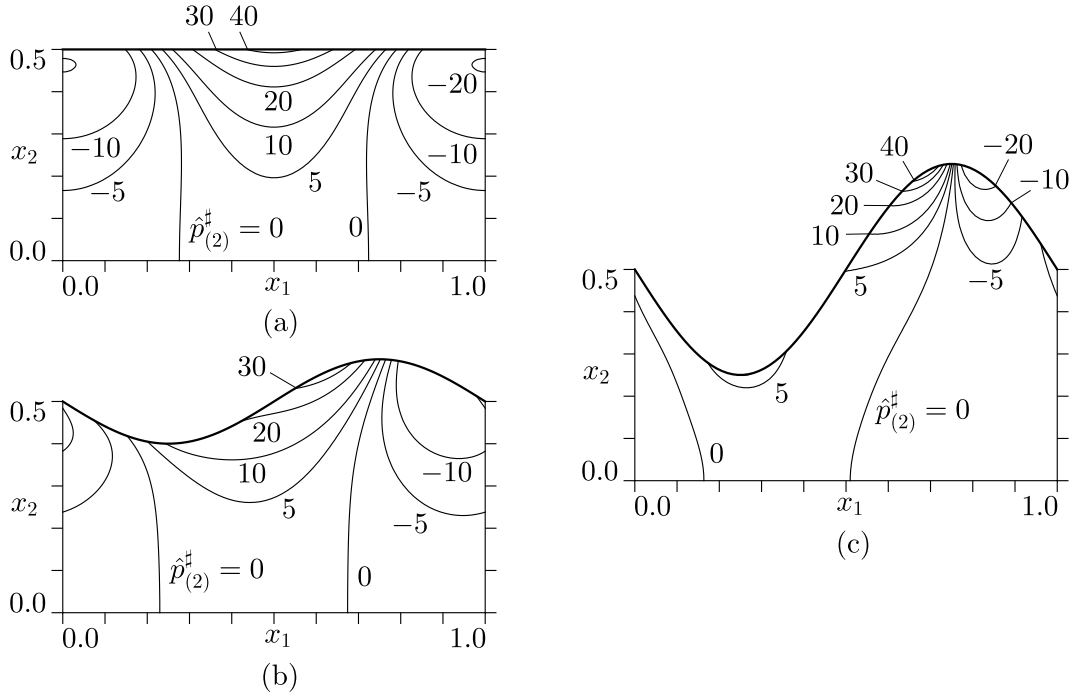

FIGURE 2.6: Isocurves of $p^{\sharp}_{(2)}$ in a channel with sinusoidal walls. All subfigures are drawn for parameter values $L/D_0 = 1$ and $T_c/T_0 = 0.5$, whereas in (a) $d/D_0 = 0.0$, in (b) $d/D_0 = 0.2$, and in (c) $d/D_0 = 0.5$.

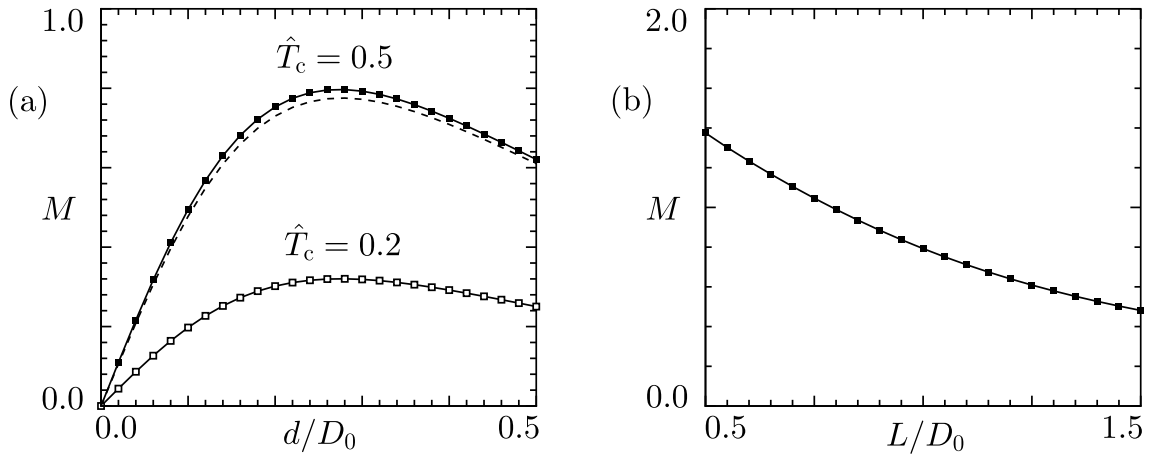

FIGURE 2.7: Parameter dependence of one-way mass flow M for a sinusoidal channel. (a) shows dependence on d/D_0 for $L/D_0 = 2$. Black dots represent $T_c/T_0 = 0.5$, white dots $T_c/T_0 = 0.2$, and the dashed line the corresponding result for $T_c/T_0 = 0.5$ without the non-Navier–Stokes terms. (b) shows dependence on L/D_0 for $d/D_0 = 0.3$ and $T_c/T_0 = 0.5$.

creates difficulties for the numerical solution method.

Let M be defined as

$$M = 2 \int_0^{1+(d/D_0)\cos(2\pi X_1/L)} \hat{\rho}_{(0)}\, \hat{u}_{1(1)} \mathrm{d}x_2 \tag{2.28}$$

which is independent of x_2. Then, $M\varepsilon$ is the leading-order dimensionless mass-flow rate in the x_1 direction [the Knudsen layer correction to $\hat{v}_{1(1)}$, which is confined in a layer with thickness of $O(\varepsilon)$, contributes to the mass-flow rate only in the next order in ε]. The corresponding dimensional mass-flow rate (per unit thickness of the channel and per unit time) is given by $\rho_0(2RT_0)^{1/2}D_0 M\varepsilon$. Figure 2.7(a) shows M versus d/D_0 for $\hat{T}_c = 0.5$ and 0.2 in the case of $L/D_0 = 1$, and Fig. 2.7(b) shows M versus L/D_0 for $d/D_0 = 0.3$ and $\hat{T}_c = 0.5$. It can be seen that there is an optimal choice of d to maximize the mass-flow rate. The dashed line in Fig. 2.7(a) shows the result for $\hat{T}_c = 0.5$ based on Eqs. (2.5a)–(2.5c) without the non-Navier–Stokes stress term (i.e., with $\hat{\gamma}_3 = \Gamma_7 = 0$). The difference is small in the present problem but still visible.

If we consider the continuum limit $\varepsilon \to 0$, then the flow in the channel vanishes because of $\hat{v}_{k(0)} \equiv 0$ [cf. Eq. (2.2)]. Therefore, the temperature field in the gas

reduces to that of a stationary gas, which is known to be described by the steady heat-conduction equation. The isolines of the corresponding solution of the steady heat-conduction equation is shown by the dotted line in Fig. 2.5. On the other hand, the solution $\hat{T}_{(0)}$ of the present fluid-dynamic-type system is nothing else than the temperature field in the continuum limit [cf. Eq. (2.2)]. However, it does not coincide with the solution of the heat-conduction equation. This discrepancy is caused by the infinitesimal velocity field, and it turns out that the heat-conduction equation, which does not contain this effect, cannot describe the temperature field in the stationary gas correctly. This is the ghost effect mentioned in the introduction, and the present problem is one example. The reader is referred to [5, 6, 8] for detailed information about this effect. Equations similar to Eqs. (2.5a)–(2.5c) had been derived in [11] in a more intuitive way for the purpose of demonstrating the convection caused by the thermal stress, but the ghost effect was not noticed there.

2.4.B One-way flow in a channel of snaky shape

We next consider a two-dimensional channel of a periodic snaky shape, composed of alternating pieces of curved segments and straight segments as shown in Fig. 2.8. The temperature of the channel walls, which will be specified later, is also periodic with the same period as the channel shape. Let us consider the basic unit composed of a curved and a straight segment defined as follows: The curved segment is defined by

$$X_1 = -\sqrt{(b + D_0)^2 - X_2^2} \qquad \text{(outer wall)}, \tag{2.29a}$$

$$X_1 = -\frac{1}{a}\sqrt{1 - \frac{X_2^2}{b^2}} \qquad \text{(inner wall)}, \tag{2.29b}$$

where D_0 is the channel width at the widest point, and $2a$ and $2b$ is the major and minor axis, respectively, of the half-elliptic inner wall (assuming that $a \geq b$); the

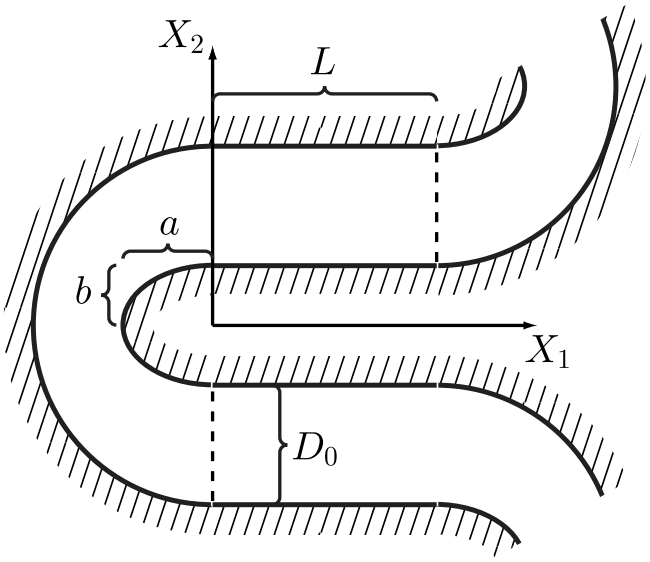

FIGURE 2.8: Channel of snaky shape.

straight segment is defined by

$$0 \le X_1 \le L;\ X_2 = b + D_0 \qquad \text{(outer wall)}, \tag{2.30a}$$

$$0 \le X_1 \le L;\ X_2 = b \qquad \text{(inner wall)}. \tag{2.30b}$$

We assume that the wall temperature of the basic unit is highest at the connection of the two segments, i.e., at $(0,\ b)$ and $(0,\ b + D_0)$, and lowest at both ends, i.e., at $(0,\ -b)$ and $(0,\ -b - D_0)$ and at $(L,\ b)$ and $(L,\ b + D_0)$ and that it varies sinusoidally along the wall in each segment. That is, the wall temperature $T_{\rm w}$ is given by

$$T_{\rm w} = T_0 \left(1 + \hat{T}_{\rm c} \frac{X_2}{\sqrt{X_1^2 + X_2^2}} \right) \qquad \text{(curved segment)}, \tag{2.31a}$$

$$T_{\rm w} = T_0 \left(1 + \hat{T}_{\rm c} \cos \frac{\pi X_1}{L} \right) \qquad \text{(straight segment)}. \tag{2.31b}$$

It is clear that the original periodic channel is geometrically composed of the above basic unit and its mirror image (with respect to X_2 axis) with appropriate translation. We assume that the wall temperature of the original channel is also determined in the same way. Then, because of the periodicity and symmetry, we can solve the problem considering only the basic unit by imposing appropriate conditions at both ends.

The present problem is motivated by recent attempts to make a Knudsen-type compressor using the change of curvature of the channel instead of the change of the channel width (cf. the problem in the previous subsection) [12, 13]. Therefore the basic unit under consideration is the one where the inner wall is semi-circular, i.e. $a = b$. For a similar setting, a DSMC computation [12] as well as a deterministic computation [13] based on the BGK model has been performed, and a fluid-dynamic model has also been derived [13]. These computations show that a one-way net mass flow is caused for intermediate Knudsen numbers. However, since the mass-flow rate is smaller than the case of using the width change and, moreover, the induced flow becomes slower for smaller Knudsen numbers, it becomes increasingly difficult to confirm the one-way net mass flow with the decrease of the Knudsen number by

means of the direct numerical computations. Therefore, the present study provides some pieces of information about the possibility of the one-way net mass flow for small Knudsen numbers. In Figs. 2.9(b), 2.9(c), and 2.9(d), we show, respectively, the flow velocity $u_{k(1)}$, the isolines of $\hat{T}_{(0)}$, and those of $\hat{p}^{\sharp}_{(2)}$ in the case of $d/D_0 = 1.5$, $L/D_0 = \pi/2$, and $\hat{T}_{\rm c} = 0.5$. In Fig. 2.9(a), the arrow indicates the vector $u_{k(1)}$ at its starting point, and its scale is shown in the figure. In Fig. 2.9(d), the additive constant of $p^{\sharp}_{(2)}$ is chosen in the same way as in Fig. 2.6. From Fig. 2.9(a), it is not clear whether there is a net one-way mass flow or not.

As in the previous problem, let $\rho_0(2RT_0)^{1/2}D_0\,M\varepsilon$ be the dimensional mass-flow rate (per unit thickness of the channel and per unit time) in the clockwise direction in the basic unit (i.e., in the X_1 direction in the straight segment). Figure 2.11(a) shows M versus b/D_0 for $L/D_0 = \pi(b/D_0 + 1)$ (the case where the length of the straight segment is the same as that of the outer wall of the semi-circular segment) and $L/D_0 = \pi b/D_0$ (the case where the length of the straight segment is the same as that of the inner wall of the semi-circular segment) when $\hat{T}_{\rm c} = 0.5$. Figure 2.11(b) shows M versus L/D_0 for $b/D_0 = 0.5$ and $\hat{T}_{\rm c} = 0.5$. These figures confirm that there is a net one-way mass flow, which is larger for a shorter straight segment. However, the mass-flow rate is much smaller than for the channel with sinusoidal walls.

We may incorporate the effect of the change of the width (cf. the first problem) to enhance the one-way mass flow. If we replace the inner wall of the semi-circular segment with a semi-ellipse to reduce the width at $X_2 = 0$ by one half, i.e. setting $a/D_0 \to 1.0$ and keeping $b/D_0 = 0.5$, $L/D_0 = \pi b/D_0$ and $\hat{T}_{\rm c} = 0.5$, the mass flow rate can be increased about three times ($2.05 \times 10^{-2} \to 6.62 \times 10^{-2}$). The flow field is displayed in Fig. 2.10. The increase in mass flow rate not so large as might be expected from the first problem. This may be due to the fact that the curved channel impedes the resulting one-way flow. However, the smaller mass-flow rate does not necessarily mean that the pumping effect is equally small when the channel is used

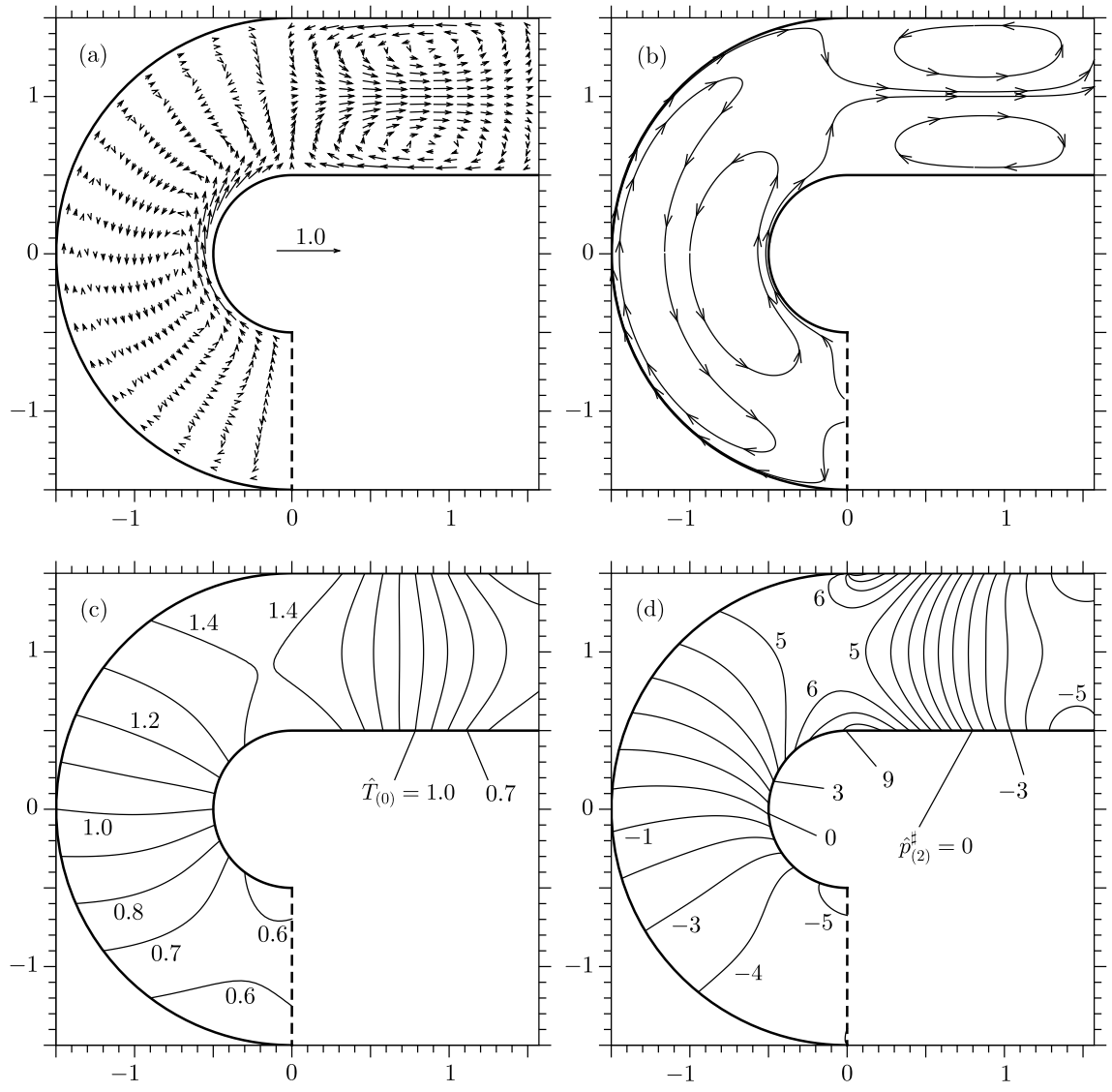

FIGURE 2.9: One-way flow through a channel of snaky shape and uniform width. Subfigures (a), (b), (c) and (d) show the flow field for parameter values $a/D_0 = b/D_0 = 0.5$, $L/D_0 = \pi/2$, and $\hat{T}_c = 0.5$. (a) shows the flow velocity field with arrows indicating the vector $(\hat{v}_{1(1)}, \hat{v}_{2(1)})$ at its starting point. (b) shows streamlines of the flow velocity field. (c) shows isocurves of $\hat{T}_{(0)}$. (d) shows isocurves of $\hat{p}^{\sharp}_{(2)}$

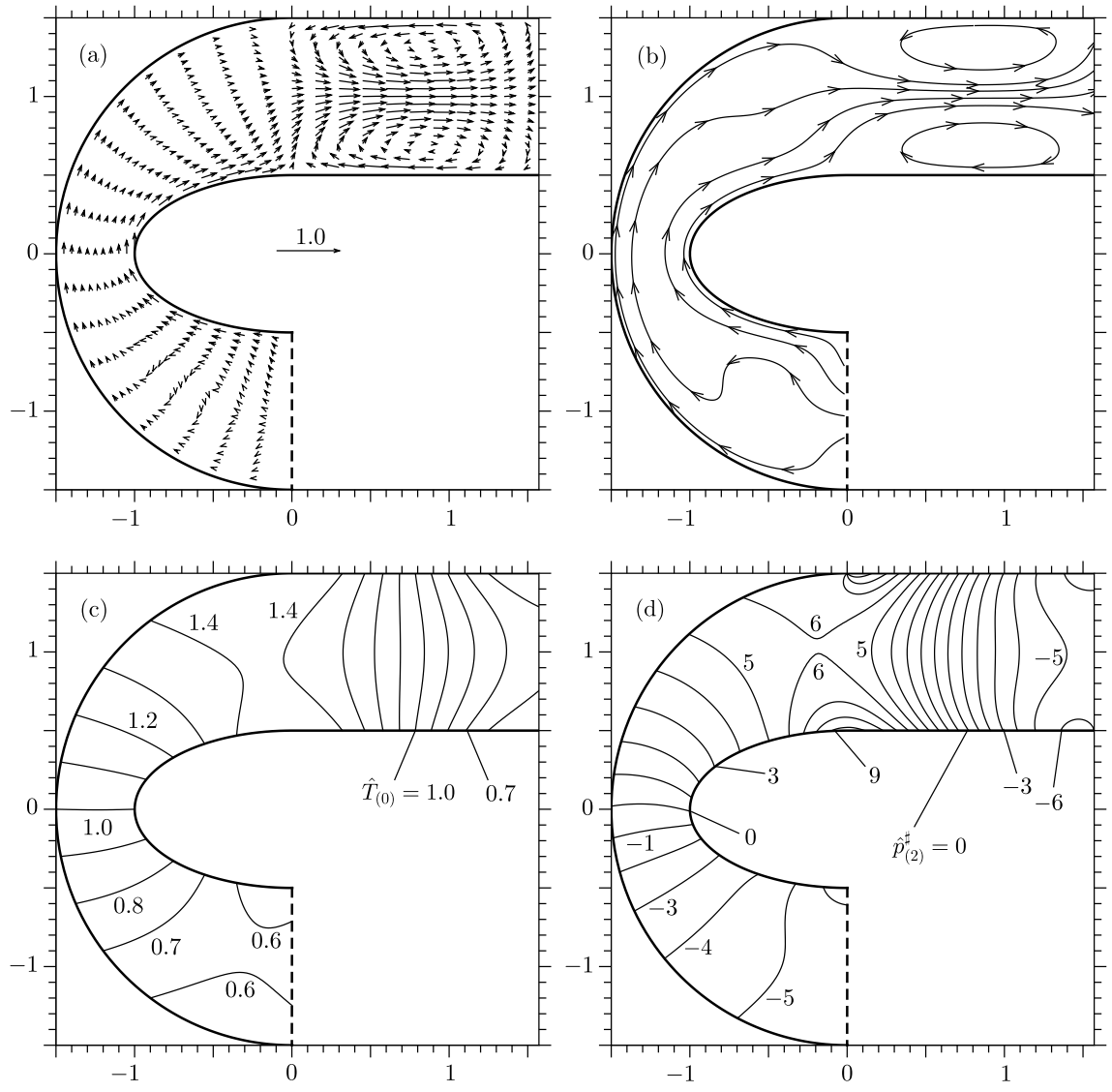

FIGURE 2.10: One-way flow through a channel of snaky shape and variable width. Subfigures (a), (b), (c) and (d) show the flow field for parameter values $a/D_0 = 1.0$, $b/D_0 = 0.5$, $L/D_0 = \pi/2$, and $\hat{T}_c = 0.5$. (a) shows the flow velocity field with arrows indicating the vector $(\hat{v}_{1(1)}, \hat{v}_{2(1)})$ at its starting point. (b) shows streamlines of the flow velocity field. (c) shows isocurves of $\hat{T}_{(0)}$. (d) shows isocurves of $\hat{p}^{\sharp}_{(2)}$

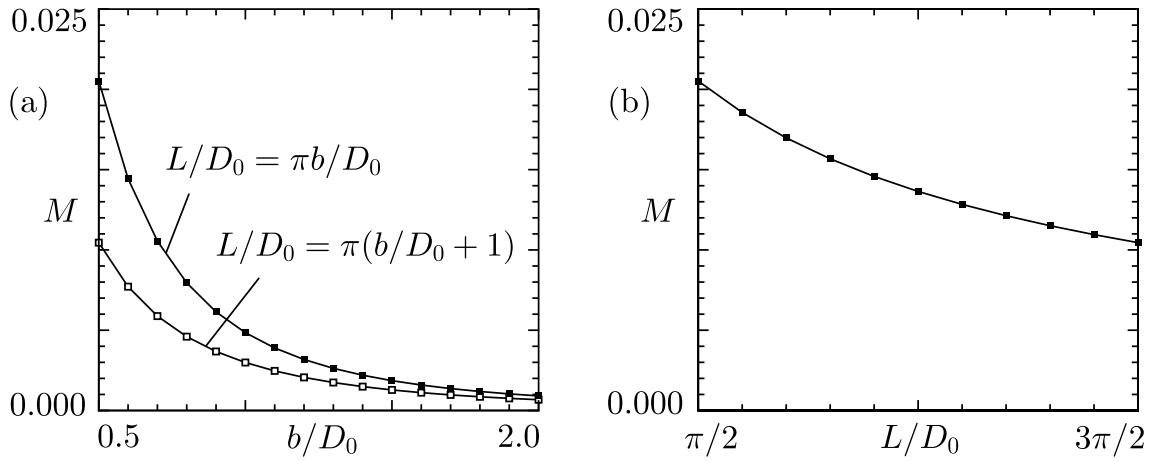

FIGURE 2.11: Parameter dependence of one-way mass flow m for a snake-shaped channel. (a) shows dependence on b/D_0 for $\hat{T}_c = 0.5$. Black dots represent $L/D_0 = \pi b/D_0$, and white dots $L/D_0 = \pi(b/D_0 + 1)$. (b) shows dependence on L/D_0 for $b/D_0 = 0.5$ and $\hat{T}_c = 0.5$. In all cases $a = b$.

as a Knudsen-type pump.

2.5 Concluding remarks

In this chapter, we investigated the thermal creep induced one-way mass flow of a slightly rarefied gas in a periodic channel with curved boundaries. We assumed that there was a finite temperature variation on the channel wall and no imposed pressure gradient, and we further assumed the gas to consist of hard-spheres undergoing diffuse reflection at the walls. We described how the correct fluid-dynamic-type system could be derived for this problem using systematic asymptotic analysis of the Boltzmann system, by expanding the macroscopic quantities in a power series of the Knudsen number. We discussed how the higher-order temperature gradient terms could be eliminated by introducing a modifed second order pressure.

Next, we discussed the numerical solution method for the fluid-dynamic-type system, noting the similarites with the incompressible Navier-Stokes system due to the pressure gradient term only appearing in the momentum equation. Because of geometrical complexity the streamfunction-vorticity finite difference method used in

previous numerical studies was considered inadequate for the present purpose, and a new method was developed, based on a colocated finite volume approach, with the SIMPLE algorithm for handling the second order pressure.

We described two different geometrical configurations through which one-way mass flow could be induced. First through the varying width of a channel, and second through the varying curvature of a channel. The channel of varying width is a form of Knudsen compressor, a concept developed by Danish physicist Martin Knudsen a century ago, but which has received much interest in the last decade for its application to microflows as a pump without moving parts. The channel with varying curvature is a more recent concept, attractive because of its simplicity - it could be constructed just by the bending of a straight pipe.

The numerical results showed the effiency of the first concept, and the somewhat lesser efficiency of the second concept, to induce a large one way mass flow. We note however that this does not necessarily mean that the pumping effect will be small for the varying curvature pipe.

We also mentioned briefly about the ghost effect, describing how the temperature field obtained through the systematic asymptotic analysis of the Boltzmann system is not the same as that which would have been obtained if the usual classical fluid dynamic assumptions had been applied from the outset.

References

[1] Sone, Y., "Thermal creep in rarefied gas," J. Phys. Soc. Japan **21**, 1836 (1966).

[2] Ohwada, T., Sone, Y., and Aoki, K., "Numerical analysis of the shear and thermal creep flows of a rarefied gas over a plane wall on the basis of the linearized Boltzmann equation for hard-sphere molecules," Phys. Fluids A **1**, 1588 (1989).

[3] Karniadakis, G., Beskok, A., and Aluru, N., *Microflows and Nanoflows: Fundamentals and Simulation* (Springer Science+Business Media, New York, 2005).

[4] Sone, Y., Aoki, K., Takata, S., Sugimoto, H., and Bobylev, A. V., "Inappropriateness of the heat-conduction equation for description of a temperature field of a stationary gas in

the continuum limit: Examination by asymptotic analysis and numerical computation of the Boltzmann equation," Phys. Fluids **8**, 628 (1996); erratum *ibid.* **8**, 841 (1996).

[5] Sone, Y., "Flows induced by temperature fields in a rarefied gas and their ghost effect on the behavior of a gas in the continuum limit," Annu. Rev. Fluid Mech. **32**, 779 (2000).

[6] Sone, Y., *Kinetic Theory and Fluid Dynamics*, Birkhäuser, Boston, 2002.

[7] Sone, Y. and Sugimoto, H., "Vacuum Pump without a Moving Part and its Performance," in *Rarefied Gas Dynamics* (AIP, Melville, 2003), p. 1041.

[8] Sone, Y., *Molecular Gas Dynamics: Theory, Techniques, and Applications* Birkhäuser, Boston, 2006.

[9] Sone, Y., Handa, M. and Doi, T., "Ghost effect and bifurcation in a gas between coaxial circular cylinders with different temperatures," Phys. Fluids **15**, 2903 (2003).

[10] Ferziger, J. H. and Perić, M., *Computational Methods for Fluid Dynamics*, Springer-Verlag, Berlin, 2002.

[11] Galkin, V. S., Kogan, M. N., and Friedlander, O. G., Izv. Akad. Nauk SSSR, Mekhanika Zhidkosti i Gaza **3**, 98 (1971).

[12] Aoki, K., Degond, P., Mieussens, L., Nishioka, M., and Takata, S., "Numerical simulation of a Knudsen pump using the effect of curvature of the channel," in *Rarefied Gas Dynamics* (AIP, Melville, 2007).

[13] Aoki, K., Degond, P., Mieussens, L., Takata, S., and Yoshida, H., "A diffusion model for rarefied flows in curved channels," Multiscale Model. Simul. (submitted)

[14] S. V. Patankar, D. B. Spalding, "A Calculation Procedure for Heat, Mass and Momentum Transfer in Three-dimensional Parabolic Flows," Int. J. Heat Mass Transfer, 15:1787-1806 (1972).

[15] C. M. Rhie, W. L. Chow, "A numerical study of the turbulent flow past an isolated airfoil with trailing edge separation," AIAA J., 21:1525-1532 (1983).

[16] S. Muzaferija, "Adaptive finite volume method for flow predictions using unstructured meshes and multigrid approach," PhD Thesis, University of London, 1994.

Chapter 3

Slow flows of a vapor-gas mixture in the near-continuum regime

3.1 Introduction

Study of vapor flows with evaporation and condensation on the boundary has been one of the important subjects in kinetic theory of gases in the last four decades (see, e.g., Refs. [1, 2, 3, 4, 5, 6]). Let us restrict ourselves to the near continuum regime in which the Knudsen number, defined by the ratio of the mean free path of the vapor molecules to the characteristic length of the system, is small. In this case, fluid-dynamic-type systems, composed of fluid-dynamic-type equations and appropriate slip and jump boundary conditions, that describe steady flows of the vapor have been derived by systematic asymptotic analysis based on the system of the Boltzmann or its model equations.[7, 8, 9, 10, 5, 6] Some of these fluid-dynamic-type systems were extended to the vapor flows in the presence of a noncondensable gas, which neither evaporates nor condenses on the boundary, for model Boltzmann equations.[11, 12] However, some interesting phenomena for the mixture of the vapor and the noncondensable gas in the near continuum regime (in particular in the continuum limit) were clarified rather recently.[13, 14, 15, 16, 17, 18]

In Ref. [16], the following rather general situation was considered: the amount of the noncondensable gas contained in the system is of the same order of magnitude as that of the vapor; the temperature variation along the boundary may be large; and the boundary is at rest, and there is no flow at infinity when an infinite domain is considered (see Sec. 3.2 for a more precise statement). The fluid-dynamic-type system that describes the steady behavior of the vapor and noncondensable gas in

this situation was derived from the Boltzmann system. In this reference, interest was focused on the ghost effect [19, 20, 21, 5, 6] in the continuum limit where the Knudsen number goes to zero. That is, it was shown that (i) the flow of the vapor caused by evaporation and condensation vanishes in the continuum limit; however, (ii) the macroscopic flow field in the limit is affected by the invisible or infinitesimal flow. This seemingly paradoxical result is of fundamental interest and importance.

On the other hand, the fluid-dynamic-type system derived in Ref. [16] is also of practical importance because it describes slow flows (with Mach number of the order of the Knudsen number) of the vapor and noncondensable gas, mainly caused by evaporation and condensation of the vapor, at small Knudsen numbers in the situation described at the beginning of the preceding paragraph. In other words, the fluid-dynamic-type system provides a tool of analysis of such flows without going back to the Boltzmann system that is much more complicated than the former system. The fluid-dynamic-type equations are not the Navier–Stokes equations but contain additional terms, the so-called Burnett terms.[22, 23] These equations as well as their boundary conditions can be derived only by kinetic considerations based on the Boltzmann system and are not obvious at all if one adheres only to macroscopic considerations.

The aim of the present paper is to show the usefulness of the fluid-dynamic-type system of Ref. [16] for practical analysis. Although the system was derived more than five years ago, its application to practical problems was not possible because it contained some coefficients in the equations as well as the boundary conditions whose numerical data were not available at that time. In the mean time, these coefficients were obtained and their databases were constructed in separate papers.[24, 25] Therefore, the fluid-dynamic-type system has been completed and is available for practical computations. The construction of a convenient numerical method for the system is also an important purpose of the present paper.

The paper is organized as follows. In Sec. 3.2, the physical problem considered in

this paper is described in a general setting. In Sec. 3.3, the fluid-dynamic-type system of Ref. [16] is summarized with the help of Appendices 3.7 and 3.8. In Sec. 3.4, a numerical solution method based on the finite-volume method [26] is constructed for the fluid-dynamic-type system. In Sec. 3.5, the fluid-dynamic-type system is applied to a physical problem, and its numerical solution is presented together with some comparisons with the numerical solution of the Boltzmann system by the direct simulation Monte Carlo (DSMC) method. [27, 28] Finally in Sec. 3.6, short concluding remarks are given.

3.2 Problem and assumption

Let us consider a binary mixture of a vapor (A-component) and a noncondensable gas (B-component) in contact with the boundary with arbitrary (but smooth) shape, made of the condensed phase (liquid or solid) of the vapor. Therefore, evaporation and condensation of the vapor may take place on the boundary. We investigate the steady flow of the mixture, mainly caused by evaporation and condensation on the boundary, on the basis of kinetic theory under the following assumptions:

(i) The amount of the noncondensable gas contained in the system is of the same order of magnitude as that of the vapor.

(ii) The behavior of the mixture is described by the Boltzmann equation for binary gas mixtures.

(iii) The vapor molecules leaving the surface of the condensed phase are distributed according to the half-range Maxwellian with temperature, flow velocity, and molecular number density equal to the temperature of the surface, the velocity of the surface, and the saturation number density of the vapor at the surface temperature.

(iv) The molecules of the noncondensable gas reflected on the surface are distributed

according to the half-range Maxwellian with temperature and flow velocity equal to the temperature and the velocity of the surface in such a way that the net molecular flux vanishes (diffuse reflection).

(v) The molecules of the vapor and those of the noncondensable gas are hard spheres.

(vi) The Knudsen number is small.

(vii) The variation of the temperature of the boundary may be large.

(viii) The boundary is at rest or moving (without motion in the normal direction) with a low speed, its Mach number being as small as the Knudsen number.

(ix) In the case of an infinite domain, the vapor as well as the noncondensable gas is at rest at infinity or flowing with a low speed, its Mach number being as small as the Knudsen number.

In this situation, the behavior of the vapor and the noncondensable gas can be described by a fluid-dynamic-type system, which will be summarized in the next section.

3.3 Fluid-dynamic-type system

In Ref. [16], a systematic asymptotic analysis for small Knudsen numbers based on the Boltzmann system was carried out in the situation described in Sec. 3.2, and a fluid-dynamic-type system was derived. The analysis is along the lines of the asymptotic theory [29, 30, 9] for a single-component gas that has been developed by Sone over the last four decades. The reader is referred to Refs. [5] and [6] for the details of the theory. In this section, we summarize the fluid-dynamic-type system derived in Ref. [16].

To begin with, we summarize the main notation appearing in what follows.

The symbol X_i denotes the rectangular coordinate system in space; n^{A}, p^{A}, v_i^{A}, m^{A}, and d^{A} denote the molecular number density, pressure, flow velocity, molecular mass, and molecular diameter of the vapor, respectively, and n^{B}, p^{B}, v_i^{B}, m^{B}, and d^{B} the corresponding quantities of the noncondensable gas; n, ρ, T, p, and v_i are the molecular number density, mass density, temperature, pressure, and barycentric flow velocity of the total mixture, respectively ($p = knT$, where k is the Boltzmann constant). The reference quantities are denoted by the subscript 0, i.e., L_0 is the reference length of the system, m_0 the reference molecular mass, d_0 the reference molecular diameter, T_0 the reference temperature, n_0 the reference molecular number density, ρ_0 the reference mass density ($\rho_0 = m_0 n_0$), p_0 ($= kn_0T_0$) the reference pressure, l_0 the reference mean free path ($l_0 = 1/\sqrt{2}\pi d_0^2 n_0$), and $\mathrm{Kn} = l_0/L_0$ the Knudsen number. The symbols n_i and t_i denote, respectively, the unit normal vector (pointing into the gases) and a unit tangential vector to the boundary, T_{w} and $v_{\mathrm{w}i}$ are the temperature and velocity of the boundary ($v_{\mathrm{w}i}n_i = 0$), and $n_{\mathrm{w}}^{\mathrm{A}}$ and $p_{\mathrm{w}}^{\mathrm{A}}$ ($= kn_{\mathrm{w}}^{\mathrm{A}}T_{\mathrm{w}}$) are the saturation number density and pressure of the vapor at temperature T_{w}. Assumption (viii) requires that $v_{\mathrm{w}i}/(2kT_0/m_0)^{1/2}$ is of the order of Kn. The Greek letter α is used to express the labels A and B of the component gases (α-component, n^α, T^α, etc.).

Then, we introduce the following dimensionless quantities:

$$
\begin{aligned}
&x_i = X_i/L_0, \qquad \hat{m}^\alpha = m^\alpha/m_0,\\
&\hat{d}^\alpha = d^\alpha/d_0, \qquad \hat{n}^\alpha = n^\alpha/n_0,\\
&\hat{p}^\alpha = p^\alpha/p_0, \qquad \hat{v}_i^\alpha = v_i^\alpha/(2kT_0/m_0)^{1/2},\\
&\hat{n} = n/n_0, \qquad \hat{\rho} = \rho/\rho_0, \qquad \hat{p} = p/p_0,\\
&\hat{v}_i = v_i/(2kT_0/m_0)^{1/2}, \qquad \hat{T} = T/T_0,\\
&\hat{T}_{\mathrm{w}} = T_{\mathrm{w}}/T_0, \qquad \hat{v}_{\mathrm{w}i} = v_{\mathrm{w}i}/(2kT_0/m_0)^{1/2},\\
&\hat{n}_{\mathrm{w}}^{\mathrm{A}} = n_{\mathrm{w}}^{\mathrm{A}}/n_0, \qquad \hat{p}_{\mathrm{w}}^{\mathrm{A}} = p_{\mathrm{w}}^{\mathrm{A}}/p_0,
\end{aligned}
\tag{3.1}
$$

where $\hat{v}_{\mathrm{w}i}$ is a quantity of the order of Kn. Thus, $\hat{p} = \hat{n}\hat{T}$ and $\hat{p}_{\mathrm{w}}^{\mathrm{A}} = \hat{n}_{\mathrm{w}}^{\mathrm{A}}\hat{T}_{\mathrm{w}}$ hold.

3.3.A Fluid-dynamic-type equations

According to Ref. [16], the physical quantities are expanded in power series of a small parameter $\epsilon = (\sqrt{\pi}/2)\mathrm{Kn}$. To be more specific, let h stand for any of $\hat{n}^\alpha$, $\hat{p}^\alpha$, $\hat{v}_i^\alpha$ ($\alpha = \mathrm{A}, \mathrm{B}$), $\hat{n}$, $\hat{\rho}$, $\hat{p}$, $\hat{v}_i$, and $\hat{T}$, then

$$h = h_{(0)} + h_{(1)}\epsilon + h_{(2)}\epsilon^2 \cdots , \tag{3.2}$$

where

$$\hat{v}_{i(0)}^\alpha = \hat{v}_{i(0)} \equiv 0. \tag{3.3}$$

It should be noted that the expansion for the velocities $\hat{v}_i^\alpha$ and $\hat{v}_i$ starts from the first order. The coefficients $h_{(0)}$, $h_{(1)}$, ... are governed by the fluid-dynamic-type equations.

The equations for the first two terms of the expansion for $\hat{p}$ are simply

$$\frac{\partial \hat{p}_{(0)}}{\partial x_i} = 0, \qquad \frac{\partial \hat{p}_{(1)}}{\partial x_i} = 0. \tag{3.4}$$

The constants $\hat{p}_{(0)}$ and $\hat{p}_{(1)}$ are to be determined from conditions proper to each problem.

The first non-trivial set of the fluid-dynamic-type equations are as follows:

$$\frac{\partial}{\partial x_j}(\hat{n}_{(0)}^{\mathrm{A}}\hat{v}_{j(1)}^{\mathrm{A}}) = 0, \tag{3.5a}$$

$$\frac{\partial}{\partial x_j}(\hat{n}_{(0)}^{\mathrm{B}}\hat{v}_{j(1)}^{\mathrm{B}}) = 0, \tag{3.5b}$$

$$
\begin{aligned}
2\hat{\rho}_{(0)}\hat{v}_{j(1)}\frac{\partial \hat{v}_{i(1)}}{\partial x_j} = & -\frac{\partial \hat{p}_{(2)}}{\partial x_i} \\
& + \frac{\partial}{\partial x_j}\left(\hat{\mu}\hat{T}_{(0)}^{1/2}\,\overline{\frac{\partial \hat{v}_{i(1)}}{\partial x_j}}\right) \\
& - \frac{\partial}{\partial x_j}\left(\frac{\hat{\Upsilon}_1}{\hat{p}_{(0)}}\,\overline{\frac{\partial \hat{T}_{(0)}}{\partial x_i}\frac{\partial \hat{T}_{(0)}}{\partial x_j}}\right) \\
& - \frac{\partial}{\partial x_j}\left[\frac{1}{\hat{n}_{(0)}}\,\overline{\frac{\partial}{\partial x_j}\left(\hat{\Upsilon}_2\frac{\partial \hat{T}_{(0)}}{\partial x_i}\right)}\right] \\
& - \frac{\partial}{\partial x_j}\left(\hat{\Upsilon}_3\frac{\hat{T}_{(0)}}{\hat{n}_{(0)}}\,\overline{\frac{\partial X^{\mathrm{A}}}{\partial x_i}\frac{\partial X^{\mathrm{A}}}{\partial x_j}}\right) \\
& - \frac{\partial}{\partial x_j}\left(\frac{\hat{\Upsilon}_4}{\hat{n}_{(0)}}\,\overline{\frac{\partial X^{\mathrm{A}}}{\partial x_j}\frac{\partial \hat{T}_{(0)}}{\partial x_i}}\right) \\
& - \frac{\partial}{\partial x_j}\left[\frac{\hat{T}_{(0)}}{\hat{n}_{(0)}}\,\overline{\frac{\partial}{\partial x_j}\left(\hat{\Upsilon}_5\frac{\partial X^{\mathrm{A}}}{\partial x_i}\right)}\right], \qquad (3.5c)
\end{aligned}
$$

$$
\begin{aligned}
\frac{\partial}{\partial x_j}\left(\hat{\lambda}\hat{T}_{(0)}^{1/2}\frac{\partial \hat{T}_{(0)}}{\partial x_j}\right) & - \frac{\partial}{\partial x_j}[k_T\,\hat{p}_{(0)}\,(\hat{v}^{\mathrm{A}}_{j(1)} - \hat{v}^{\mathrm{B}}_{j(1)})] \\
& - \frac{5}{2}(\hat{n}^{\mathrm{A}}_{(0)}\hat{v}^{\mathrm{A}}_{j(1)} + \hat{n}^{\mathrm{B}}_{(0)}\hat{v}^{\mathrm{B}}_{j(1)})\frac{\partial \hat{T}_{(0)}}{\partial x_j} = 0, \qquad (3.5d)
\end{aligned}
$$

$$
\hat{v}^{\mathrm{A}}_{i(1)} - \hat{v}^{\mathrm{B}}_{i(1)} = -\frac{\hat{T}_{(0)}^{1/2}}{\hat{n}_{(0)}}\frac{\hat{D}_{\mathrm{AB}}}{X^{\mathrm{A}}X^{\mathrm{B}}}\left(\frac{\partial X^{\mathrm{A}}}{\partial x_i} + k_T\frac{\partial \ln \hat{T}_{(0)}}{\partial x_i}\right), \qquad (3.5e)
$$

where

$$
\hat{n}_{(0)} = \hat{n}^{\mathrm{A}}_{(0)} + \hat{n}^{\mathrm{B}}_{(0)}, \qquad (3.6a)
$$

$$
\hat{\rho}_{(0)} = \hat{m}^{\mathrm{A}}\hat{n}^{\mathrm{A}}_{(0)} + \hat{m}^{\mathrm{B}}\hat{n}^{\mathrm{B}}_{(0)}, \qquad (3.6b)
$$

$$
\hat{v}_{i(1)} = (\hat{m}^{\mathrm{A}}\hat{n}^{\mathrm{A}}_{(0)}\hat{v}^{\mathrm{A}}_{i(1)} + \hat{m}^{\mathrm{B}}\hat{n}^{\mathrm{B}}_{(0)}\hat{v}^{\mathrm{B}}_{i(1)})/\hat{\rho}_{(0)}, \qquad (3.6c)
$$

$$
\hat{p}_{(0)} = \hat{n}_{(0)}\hat{T}_{(0)}, \qquad (3.6d)
$$

$$
X^{\alpha} = \hat{n}^{\alpha}_{(0)}/\hat{n}_{(0)}, \qquad (3.6e)
$$

$$
\overline{A_{ij}} = A_{ij} + A_{ji} - (2/3)A_{kk}\delta_{ij}. \qquad (3.6f)
$$

Here, X^{α} is the local concentration of the α–component in the zeroth order ($X^{\mathrm{A}} + X^{\mathrm{B}} = 1$). The coefficients $\hat{\mu}$, $\hat{\lambda}$, $\hat{D}_{\mathrm{AB}}$, k_T, $\hat{\Upsilon}_1$, $\hat{\Upsilon}_2$, $\hat{\Upsilon}_3$, $\hat{\Upsilon}_4$, and $\hat{\Upsilon}_5$ (transport co-

efficients for short), which depend on $\hat{m}^\alpha$ and $\hat{d}^\alpha$, are functions of the local concentration $X^{\rm A}$. The $\hat{\mu}$, $\hat{\lambda}$, and $\hat{D}_{\rm AB}$ correspond to the viscosity μ, thermal conductivity λ, and mutual-diffusion coefficient $D_{\rm AB}$; more specifically, they are related as $\mu = (\sqrt{\pi}/2)(2kT_0/m_0)^{-1/2}\ p_0 l_0 \hat{T}_{(0)}^{1/2}\hat{\mu}$, $\lambda = (\sqrt{\pi}k/m_0)(2kT_0/m_0)^{-1/2} p_0 l_0 \hat{T}_{(0)}^{1/2}\hat{\lambda}$, and $D_{\rm AB} = (\sqrt{\pi}/2)(2kT_0/m_0)^{1/2} l_0 (\hat{T}_{(0)}^{1/2}/\hat{n}_{(0)})\hat{D}_{\rm AB}$. The k_T is the thermal-diffusion ratio, i.e., the ratio of the thermal-diffusion coefficient to the mutual-diffusion coefficient. The definitions of these transport coefficients are given in Appendix 3.7.

Equations (3.5a)–(3.5e), with the help of Eqs. (3.6a)–(3.6e), form a closed set of equations for $\hat{n}_{(0)}^{\rm A}$, $\hat{n}_{(0)}^{\rm B}$, $\hat{n}_{(0)}$, $X^{\rm A}$, $X^{\rm B}$, $\hat{\rho}_{(0)}$, $\hat{T}_{(0)}$, $\hat{v}_{i(1)}^{\rm A}$, $\hat{v}_{i(1)}^{\rm B}$, $\hat{v}_{i(1)}$, and $\hat{p}_{(2)}$, which can finally be reduced to a set of partial differential equations for $\hat{n}_{(0)}^{\rm A}$ (or $X^{\rm A}$), $\hat{T}_{(0)}$, $\hat{v}_{i(1)}$, and $\hat{p}_{(2)}$. The partial pressure $\hat{p}_{(0)}^\alpha$ of each component is then given by

$$\hat{p}_{(0)}^\alpha = \hat{n}_{(0)}^\alpha \hat{T}_{(0)}. \tag{3.7}$$

It should be remarked here that the functional forms of the transport coefficients $\hat{\mu}$, $\hat{\lambda}$, $\hat{D}_{\rm AB}$, k_T, $\hat{\Upsilon}_1$, $\hat{\Upsilon}_2$, $\hat{\Upsilon}_3$, $\hat{\Upsilon}_4$, and $\hat{\Upsilon}_5$, as functions of the local concentration $X^{\rm A}$ of the vapor, cannot be obtained explicitly. However, for application of Eqs. (3.5a)–(3.5e) to practical problems, the functional forms are indispensable. Therefore, in Ref. [24], the functional forms were obtained numerically, and their database was constructed. By making use of the database, Eqs. (3.5a)–(3.5e) become applicable to concrete problems at least at the numerical level.

It should be mentioned that equations similar to Eqs. (3.5a)–(3.5e) had been derived from the so-called Burnett equations for a mixture of noncondensable gases in a more intuitive way in Ref. [23], where convection is shown to be induced by the imbalance of the concentration stress.

3.3.B Boundary conditions

The boundary conditions on the surface of the condensed phase for the fluid-dynamic-type equations (3.5a)–(3.5e) are obtained by analyzing the Knudsen layer, the thin

layer of thickness of the order of the mean free path adjacent to the surface. The boundary conditions taken from Ref. [16] are summarized as follows:

$$\hat{n}^{\mathrm{A}}_{(0)} = \hat{n}^{\mathrm{A}}_{\mathrm{w}} \ (= \hat{p}^{\mathrm{A}}_{\mathrm{w}}/\hat{T}_{\mathrm{w}}), \tag{3.8a}$$

$$\hat{T}_{(0)} = \hat{T}_{\mathrm{w}}, \tag{3.8b}$$

$$\hat{v}^{\mathrm{B}}_{i(1)} n_i = 0, \tag{3.8c}$$

$$(\hat{v}_{i(1)} - \hat{U}_i) t_i = -\hat{T}^{1/2}_{(0)} \left(b_7 \frac{1}{\hat{p}_{(0)}} \frac{\partial \hat{T}_{(0)}}{\partial x_i} t_i + b_9 \frac{1}{\hat{n}_{(0)}} \frac{\partial X^{\mathrm{A}}}{\partial x_i} t_i \right). \tag{3.8d}$$

Here, the velocity of the boundary $\hat{v}_{\mathrm{w}i}$ has been written as

$$\hat{v}_{\mathrm{w}i} = \hat{U}_i \epsilon, \tag{3.9}$$

with $\hat{U}_i$ being of $O(1)$, and b_7 and b_9, which depend on $\hat{m}^\alpha$ and $\hat{d}^\alpha$, are functions of the local concentration X^{A} of the vapor. The term containing b_7 in Eq. (3.8d) indicates the velocity slip due to the temperature variation along the boundary (the thermal slip or thermal creep), whereas the term containing b_9 the velocity slip due to the variation of the local concentration of the vapor along the boundary (the diffusion slip). The b_7 (thermal-slip coefficient) and b_9 (diffusion-slip coefficient) were obtained by the analysis of the two fundamental half-space problems of the linearized Boltzmann equation.[25] Note that (b_7, b_9) (here and in Ref. [16]) = ($-b_I$, $-b_{II}$) (Ref. [25]). In this reference, a database from which accurate values of b_7 and b_9 can be obtained instantaneously for a given X^{A} is constructed. The details are summarized in Appendix 3.8.

The thermal slip is a classical phenomenon in kinetic theory[31, 32] and has been investigated by many authors. Here, we only refer to a few papers that seem to be of some importance out of many existing works: Refs. [21] and [32, 33, 34, 35, 36, 37] for a single-component gas and Refs. [25] and [38, 39, 40, 41, 42] for a gaseous mixture. The diffusion slip, which is peculiar to a gaseous mixture, is also a classical problem, about which we refer to Refs. [25], [38], [40], [42] and [43, 44, 45, 46].

3.3.C Remarks on continuum limit

In this subsection, we give a short remark on the continuum limit where Kn or ϵ vanishes. In this limit, the macroscopic variables $\hat{n}^{\mathrm{A}}$, $\hat{n}^{\mathrm{B}}$, $\hat{n}$, $\hat{T}$, $\hat{v}_i^{\mathrm{A}}$, $\hat{v}_i^{\mathrm{B}}$, $\hat{v}_i$, $\hat{p}$, etc. reduce to their respective leading-order terms in the expansion (3.2), for instance, ($\hat{n}^{\mathrm{A}}$, $\hat{n}^{\mathrm{B}}$, $\hat{T}$, $\hat{p}$) $\to$ ($\hat{n}^{\mathrm{A}}_{(0)}$, $\hat{n}^{\mathrm{B}}_{(0)}$, $\hat{T}_{(0)}$, $\hat{p}_{(0)}$) and ($\hat{v}_i^{\mathrm{A}}$, $\hat{v}_i^{\mathrm{B}}$, $\hat{v}_i$) $\to$ (0, 0, 0) [cf. Eq. (3.3)]. That is, in this limit, the flow velocity vanishes, and thus evaporation and condensation of the vapor stop. Therefore, one might expect that the temperature field in this limit is given by the steady heat-conduction equation (for a binary mixture) with the no-jump boundary condition, which is considered to describe the temperature field in a stationary gas in the continuum limit. However, this is not the case. The leading-order terms $\hat{n}^{\mathrm{A}}_{(0)}$, $\hat{n}^{\mathrm{B}}_{(0)}$, and $\hat{T}_{(0)}$ are determined together with the first-order velocity fields $\hat{v}^{\mathrm{A}}_{i(1)}$ and $\hat{v}^{\mathrm{B}}_{i(1)}$ (and $\hat{v}_{i(1)}$) by the fluid-dynamic-type system described in Secs. 3.3.A and 3.3.B, which is different from the heat-conduction equation. An example demonstrating this discrepancy will be shown in Fig. 3.10(d) in Sec. 3.5.B. This means that, in spite of the fact that there is no flow, the temperature and density fields in the continuum limit are affected by the infinitesimal flow [note that $\hat{v}_i^{\alpha} = \hat{v}^{\alpha}_{i(1)}\epsilon + \cdots \to 0$, but $\hat{v}^{\alpha}_{i(1)}$ is of $O(1)$]. This is an example of the *ghost effect*.[19] Since this effect has been discussed in many places, we avoid repeating the discussion, referring to the literature, such as Refs. [20], [21], [5], [47], [48], and [6] and the references in Refs. [5] and [6] (for a gas mixture, see Refs. [15], [16], [49], and [50]). We just mention that the ghost effect associated with the present fluid-dynamic-type system is discussed in detail in Ref. [16].

3.4 Numerical method

3.4.A Preliminaries

We first rewrite the fluid-dynamic-type equations in a different form that is more convenient for our numerical method.

The continuity equation for each component can be combined to obtain a continuity equation for the barycentric velocity merely by using the definition of $\hat{\rho}_{(0)}$,

$$\frac{\partial}{\partial x_i}\left(\hat{\rho}_{(0)}\hat{v}_{i(1)}\right) = 0. \tag{3.10}$$

Using the definition of the barycentric velocity and Eq. (3.5e), we can write each velocity component as

$$\hat{v}^{\mathrm{A}}_{i(1)} = \hat{v}_{i(1)} - \frac{\hat{m}^{\mathrm{B}}\hat{D}_{\mathrm{AB}}\hat{T}^{1/2}_{(0)}}{\hat{\rho}_{(0)}X^{\mathrm{A}}}\left(\frac{\partial X^{\mathrm{A}}}{\partial x_i} + \frac{k_T}{\hat{T}_{(0)}}\frac{\partial \hat{T}_{(0)}}{\partial x_i}\right), \tag{3.11a}$$

$$\hat{v}^{\mathrm{B}}_{i(1)} = \hat{v}_{i(1)} + \frac{\hat{m}^{\mathrm{A}}\hat{D}_{\mathrm{AB}}\hat{T}^{1/2}_{(0)}}{\hat{\rho}_{(0)}(1-X^{\mathrm{A}})}\left(\frac{\partial X^{\mathrm{A}}}{\partial x_i} + \frac{k_T}{\hat{T}_{(0)}}\frac{\partial \hat{T}_{(0)}}{\partial x_i}\right). \tag{3.11b}$$

With expression (3.11a) the vapor continuity equation (3.5a) can be rewritten as

$$\frac{\partial}{\partial x_i}\left(\frac{\hat{p}_{(0)}}{\hat{T}_{(0)}}\hat{v}_{i(1)}X^{\mathrm{A}}\right) = \frac{\partial}{\partial x_i}\left[\frac{\hat{D}_{\mathrm{AB}}\hat{T}^{1/2}_{(0)}}{(\hat{m}^{\mathrm{A}}/\hat{m}^{\mathrm{B}}-1)X^{\mathrm{A}}+1}\left(\frac{\partial X^{\mathrm{A}}}{\partial x_i} + \frac{k_T}{\hat{T}_{(0)}}\frac{\partial \hat{T}_{(0)}}{\partial x_i}\right)\right]. \tag{3.12}$$

Similarly, the energy equation (3.5d) can be rewritten as

$$\frac{\partial}{\partial x_i}\left(\frac{5}{2}\frac{\hat{p}_{(0)}}{\hat{T}_{(0)}}\hat{v}_{i(1)}\hat{T}_{(0)}\right) = \frac{\partial}{\partial x_i}\left[\hat{\lambda}\hat{T}^{1/2}_{(0)}\frac{\partial \hat{T}_{(0)}}{\partial x_i}\right] - \frac{\partial}{\partial x_i}\left[\gamma\hat{T}^{3/2}_{(0)}\left(\frac{\partial X^{\mathrm{A}}}{\partial x_i} + \frac{k_T}{\hat{T}_{(0)}}\frac{\partial \hat{T}_{(0)}}{\partial x_i}\right)\right], \tag{3.13}$$

where an additional coefficient γ has been defined, related to the other coefficients as

$$\gamma \equiv \hat{D}_{\mathrm{AB}}\left[\frac{5}{2}\frac{\hat{m}^{\mathrm{A}}/\hat{m}^{\mathrm{B}}-1}{(\hat{m}^{\mathrm{A}}/\hat{m}^{\mathrm{B}}-1)X^{\mathrm{A}}+1} - \frac{k_T}{X^{\mathrm{A}}(1-X^{\mathrm{A}})}\right]. \tag{3.14}$$

Like the other coefficients it depends only on the molecular properties $\hat{m}^{\alpha}$ and $\hat{d}^{\alpha}$ and the local concentration X^{A}. Note that the definition of k_T is such that γ retains a finite value even when the gas concentration of either component approaches zero.

The equation of motion (3.5c) can be rewritten as (see Sec. 5.3 in Ref. [21])

$$\begin{aligned}\frac{\partial}{\partial x_j}\left(\hat{\rho}_{(0)}\hat{v}_{j(1)}\hat{v}_{i(1)}\right) = &-\frac{1}{2}\frac{\partial \hat{p}^{\sharp}_{(2)}}{\partial x_i}+\frac{1}{2}\frac{\partial}{\partial x_j}\left[\hat{\mu}\hat{T}_{(0)}^{1/2}\frac{\partial \hat{v}_{i(1)}}{\partial x_j}\right]\\ &+\frac{1}{2}\frac{\partial}{\partial x_j}\left[\hat{\mu}\hat{T}_{(0)}^{1/2}\frac{\partial \hat{v}_{j(1)}}{\partial x_i}\right]-\frac{1}{3}\frac{\partial}{\partial x_i}\left[\hat{\mu}\hat{T}_{(0)}^{1/2}\frac{\partial \hat{v}_{j(1)}}{\partial x_j}\right]\\ &+\frac{1}{2}\frac{\partial}{\partial x_j}\left[2\frac{\hat{\Upsilon}_1-\hat{\Upsilon}_2}{\hat{p}_{(0)}}\frac{\partial \hat{T}_{(0)}}{\partial x_i}\frac{\partial \hat{T}_{(0)}}{\partial x_j}+2\hat{\Upsilon}_3\frac{\hat{T}_{(0)}^2}{\hat{p}_{(0)}}\frac{\partial X^{\mathrm{A}}}{\partial x_i}\frac{\partial X^{\mathrm{A}}}{\partial x_j}\right.\\ &+\frac{\hat{T}_{(0)}}{\hat{p}_{(0)}}\left(\hat{\Upsilon}_4+\frac{\mathrm{d}\hat{\Upsilon}_2}{\mathrm{d}X^{\mathrm{A}}}-4\hat{\Upsilon}_5\right)\frac{\partial X^{\mathrm{A}}}{\partial x_j}\frac{\partial \hat{T}_{(0)}}{\partial x_i}\\ &\left.+\frac{\hat{T}_{(0)}}{\hat{p}_{(0)}}\left(\hat{\Upsilon}_4-\frac{\mathrm{d}\hat{\Upsilon}_2}{\mathrm{d}X^{\mathrm{A}}}\right)\frac{\partial X^{\mathrm{A}}}{\partial x_i}\frac{\partial \hat{T}_{(0)}}{\partial x_j}\right],\end{aligned} \tag{3.15}$$

by using the chain rule to expand the derivatives, and defining a modified pressure $\hat{p}^{\sharp}_{(2)}$:

$$\begin{aligned}\hat{p}^{\sharp}_{(2)} \equiv &\hat{p}_{(2)}+\frac{2}{3}\frac{\hat{\Upsilon}_1}{\hat{p}_{(0)}}\left(\frac{\partial \hat{T}_{(0)}}{\partial x_j}\right)^2\\ &-\frac{4}{3}\frac{\hat{T}_{(0)}}{\hat{p}_{(0)}}\frac{\partial}{\partial x_j}\left(\hat{\Upsilon}_2\frac{\partial \hat{T}_{(0)}}{\partial x_j}\right)-\frac{2\hat{\Upsilon}_2}{\hat{p}_{(0)}}\left(\frac{\partial \hat{T}_{(0)}}{\partial x_j}\right)^2\\ &+\frac{2}{3}\hat{\Upsilon}_3\frac{\hat{T}_{(0)}^2}{\hat{p}_{(0)}}\left(\frac{\partial X^{\mathrm{A}}}{\partial x_j}\right)^2+\frac{2}{3}\hat{\Upsilon}_4\frac{\hat{T}_{(0)}}{\hat{p}_{(0)}}\frac{\partial \hat{T}_{(0)}}{\partial x_j}\frac{\partial X^{\mathrm{A}}}{\partial x_j}\\ &-\frac{4}{3}\frac{\hat{T}_{(0)}^2}{\hat{p}_{(0)}}\frac{\partial}{\partial x_j}\left(\hat{\Upsilon}_5\frac{\partial X^{\mathrm{A}}}{\partial x_j}\right)-\frac{4\hat{T}_{(0)}\hat{\Upsilon}_5}{\hat{p}_{(0)}}\frac{\partial \hat{T}_{(0)}}{\partial x_j}\frac{\partial X^{\mathrm{A}}}{\partial x_j}.\end{aligned} \tag{3.16}$$

That is, the terms of gradient form arising from the non-Navier–Stokes terms are put inside $\hat{p}^{\sharp}_{(2)}$. By introducing the modified pressure, the apparent third-order derivatives of $\hat{T}_{(0)}$ and X^{A} in Eq. (3.5c) are eliminated, and the number of derivative terms to be approximated numerically is reduced.

In summary, we are going to solve, instead of Eqs. (3.5a)–(3.5e), the equation system (3.10), (3.12), (3.13), and (3.15), the unknowns of which are $\hat{v}_{i(1)}$, $\hat{T}_{(0)}$, X^{A} and $\hat{p}^{\sharp}_{(2)}$. The variable $\hat{\rho}_{(0)}$ is not counted among the unknowns since it depends on X^{A} and $\hat{T}_{(0)}$ as

$$\hat{\rho}_{(0)} = \frac{\hat{p}_{(0)}}{\hat{T}_{(0)}}\left[(\hat{m}^{\mathrm{A}}-\hat{m}^{\mathrm{B}})X^{\mathrm{A}}+\hat{m}^{\mathrm{B}}\right]. \tag{3.17}$$

Nevertheless, it is retained in the equations to keep the resemblance to the equations of conventional gas dynamics.

3.4.B Finite-Volume Method

Let us note that Eqs. (3.12), (3.13), and (3.15) can be expressed in the following concise form:

$$\frac{\partial}{\partial x_j}\left(M_j\phi\right) = \frac{\partial}{\partial x_j}\left(\Gamma\frac{\partial\phi}{\partial x_j}\right) + b, \tag{3.18}$$

where ϕ stands for X^{A}, $\hat{T}_{(0)}$, or the individual components of $\hat{v}_{i(1)}$, and M_i, Γ, and b, in general, depend on X^{A}, $\hat{T}_{(0)}$, and $\hat{v}_{i(1)}$ [and $\hat{p}^{\sharp}_{(2)}$ in Eq. (3.15)]. To be more specific,

$$\begin{aligned} &\phi = X^{\mathrm{A}}, \quad M_j = (\hat{p}_{(0)}/\hat{T}_{(0)})\hat{v}_{j(1)}, \\ &\Gamma = \hat{D}_{\mathrm{AB}}\hat{T}_{(0)}^{1/2}[(\hat{m}^{\mathrm{A}}/\hat{m}^{\mathrm{B}} - 1)X^{\mathrm{A}} + 1]^{-1}, \end{aligned} \tag{3.19}$$

for Eq. (3.12),

$$\begin{aligned} &\phi = \hat{T}_{(0)}, \quad M_j = (5/2)(\hat{p}_{(0)}/\hat{T}_{(0)})\hat{v}_{j(1)}, \\ &\Gamma = \hat{\lambda}\hat{T}_{(0)}^{1/2}, \end{aligned} \tag{3.20}$$

for Eq. (3.13), and

$$\begin{aligned} &\phi = \hat{v}_{i(1)}, \quad M_j = \hat{\rho}_{(0)}\hat{v}_{j(1)}, \\ &\Gamma = (1/2)\hat{\mu}\hat{T}_{(0)}^{1/2}, \end{aligned} \tag{3.21}$$

for Eq. (3.15); b's are the rest of the terms in the respective equations.

We try to solve Eq. (3.18) using the iteration scheme

$$\frac{\partial}{\partial x_j}\left(M_j^{m-1}\phi^m\right) = \frac{\partial}{\partial x_j}\left(\Gamma^{m-1}\frac{\partial\phi^m}{\partial x_j}\right) + b^{m-1}, \tag{3.22}$$

under the boundary conditions (3.8) with appropriate discretization. Here, ϕ^m denotes ϕ at the mth iteration, and M_j^{m-1}, Γ^{m-1}, and b^{m-1} mean M_j, Γ, and b evaluated by using X^{A}, $\hat{T}_{(0)}$, $\hat{v}_{i(1)}$, and $\hat{p}^{\sharp}_{(2)}$ at the $(m-1)$th iteration. More specifically, we construct a sequence $\{\phi^1, \phi^2, ...\}$, which is expected to converge, on the basis of Eq. (3.22) with an appropriate initial function ϕ^0 and regard the limit (i.e., ϕ^m with a sufficiently

large m) as an approximate solution of Eq. (3.18). Note that Eq. (3.22) is linear in each step in the iteration process. Also note that to ensure speedy convergence appropriate under-relaxation of ϕ^m should be used. The optimum under-relaxation factors are problem dependent, and we omit further discussion of them here.

The computational domain is divided into a number of small control volumes. Let us consider a single control volume Ω with boundary $\partial\Omega$. If we integrate Eq. (3.22) over this control volume, we obtain, after application of Gauss' theorem,

$$\int_{\partial\Omega} \bar{n}_j M_j^{m-1} \phi^m \, \mathrm{d}S = \int_{\partial\Omega} \bar{n}_j \Gamma^{m-1} \frac{\partial \phi^m}{\partial x_j} \mathrm{d}S + \int_{\Omega} b^{m-1} \, \mathrm{d}V, \tag{3.23}$$

where $\bar{n}_i$ is the outward unit normal vector to the surface $\partial\Omega$, $\mathrm{d}S$ is the surface element on $\partial\Omega$ in the dimensionless x_i space, and $\mathrm{d}V$ is the volume element in the same space. For simplicity, we explain the discretization of Eq. (3.23) in the case of two-dimensional problems (i.e., the problems where the physical quantities are independent of x_3 and $\hat{v}_{3(1)} = 0$). The generalization to three-dimensional problems is straightforward.

We consider a two-dimensional control volume Ω (with boundary $\partial\Omega$), which is assumed to be a quadrilateral, as depicted in Fig. 3.1. The center (barycenter) of this control volume is denoted by P, and the centers of the neighboring control volumes are denoted by E, W, N and S. The physical quantities are stored at the grid points located at the centers of the control volumes.

To save space, the method of discretization for the surface integrals in Eq. (3.23) will be described only for the cell face $\partial\Omega_{\mathrm{e}}$ between points P and E, but it is done analogously for other cell faces. We denote by L_{PE} the distance between grid points P and E and by S_{e} the area (the length times the unit width in the x_3 direction) of the surface $\partial\Omega_{\mathrm{e}}$.

We first consider the first term on the right-hand side of Eq. (3.23). In the case of a Cartesian grid, the term $\bar{n}_j(\partial\phi^m/\partial x_j)$ can be approximated by a finite difference using the values of ϕ^m at the nodes E and P. On a non-Cartesian grid, however, since the

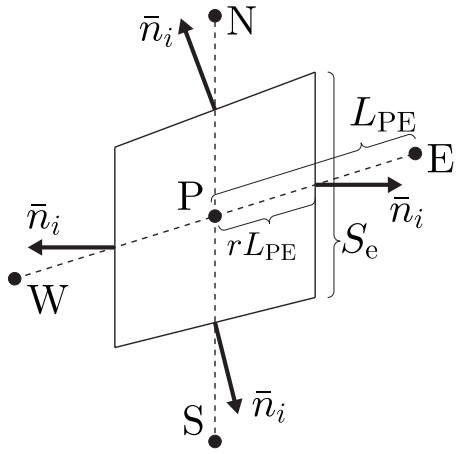

FIGURE 3.1: A control volume.

normal vector at the cell surface does not in general coincide with the line connecting E and P, we need to incorporate the values of ϕ^m at other nodes to approximate the derivative $\bar{n}_j(\partial\phi^m/\partial x_j)$. On the other hand, we wish to avoid using more node values than necessary for this approximation. This can be achieved by the deferred correction approach suggested by Muzaferija.[53] That is, if ξ_i is the unit vector pointing from node P to node E, then the term under consideration on $\partial\Omega_{\mathrm{e}}$ is approximated as

$$\int_{\partial\Omega_{\mathrm{e}}} \bar{n}_j \Gamma^{m-1} \frac{\partial\phi^m}{\partial x_j} \mathrm{d}S = S_{\mathrm{e}} \Gamma_{\mathrm{e}}^{m-1} \frac{\phi_{\mathrm{E}}^m - \phi_{\mathrm{P}}^m}{L_{\mathrm{PE}}} + S_{\mathrm{e}} \Gamma_{\mathrm{e}}^{m-1} \left(\bar{n}_j - \xi_j\right) \left(\frac{\partial\phi^{m-1}}{\partial x_j}\right)_{\mathrm{e}}, \qquad (3.24)$$

where ϕ_{P}^m and ϕ_{E}^m are the values of ϕ^m at node points P and E, and the subscript e means that the stored value has been interpolated to the cell surface at its intersection with the line PE. The point here is that the correction term required when $\bar{n}_i \neq \xi_i$ is evaluated using the value of $(\partial\phi^{m-1}/\partial x_j)_{\mathrm{e}}$ at the $(m-1)$th iteration. The term $(\partial\phi^{m-1}/\partial x_j)_{\mathrm{e}}$ on the surface $\partial\Omega_{\mathrm{e}}$ is obtained by interpolation using the corresponding gradient terms at cell centers. The latter terms are computed by taking the average over the control volume, with the integral rewritten using Gauss' theorem so that it can be expressed through grid point values interpolated to cell surfaces. For example,

in the x_1-direction we obtain

$$\left(\frac{\partial \phi^{m-1}}{\partial x_1}\right)_{\mathrm{P}} = \frac{1}{\Delta\Omega}\int_{\Omega}\frac{\partial}{\partial x_j}\phi^{m-1}\delta_{1j}\mathrm{d}\Omega$$
$$= \frac{1}{\Delta\Omega}\int_{\partial\Omega}\phi^{m-1}\bar{n}_1\mathrm{d}S. \tag{3.25}$$

Here, $\Delta\Omega$ is the cell volume (the area times the unit width in the x_3-direction in the present two-dimensional case).

Although technically the approximation (3.24) is of only first-order accuracy on a non-uniform grid (and non-uniformness is required because high accuracy demands smaller cells in some parts of the computational domain, e.g. in the vicinity of walls), the approximation is asymptotically of second order, as demonstrated in Ref. [26].

The left-hand side of Eq. (3.23) on $\partial\Omega_{\mathrm{e}}$ is discretized through linear interpolation,

$$\int_{\partial\Omega_{\mathrm{e}}}\bar{n}_j M_j^{m-1}\phi^m\,\mathrm{d}S = S_{\mathrm{e}}M_{\mathrm{e}}^{m-1}\left[r\phi_{\mathrm{E}}^m + (1-r)\phi_{\mathrm{P}}^m\right], \tag{3.26}$$

where r is a parameter associated with the non-uniformity of the grid ($0 < r < 1$; $r = 0.5$ for a uniform grid; see Fig. 3.1), and M_{e}^{m-1} indicates $\bar{n}_j M_j^{m-1}$ at the point where the line between nodes P and E crosses the cell surface.

On the other hand, the source term (the second term on the right-hand side) in Eq. (3.23) is approximated by taking the values at the grid point multiplied by the cell volume, i.e.,

$$\int_{\Omega} b^{m-1}\,\mathrm{d}V = \Delta\Omega\, b_{\mathrm{P}}^{m-1}. \tag{3.27}$$

After the discretization described above, Eq. (3.23) can be written in the form

$$a_{\mathrm{P}}^{m-1}\phi_{\mathrm{P}}^m = (a_{\mathrm{E}}^{m-1}\phi_{\mathrm{E}}^m + a_{\mathrm{W}}^{m-1}\phi_{\mathrm{W}}^m$$
$$+ a_{\mathrm{N}}^{m-1}\phi_{\mathrm{N}}^m + a_{\mathrm{S}}^{m-1}\phi_{\mathrm{S}}^m) + B^{m-1}, \tag{3.28}$$

where each of the coefficients a_{P}^{m-1}, a_{E}^{m-1}, a_{W}^{m-1}, a_{N}^{m-1}, and a_{S}^{m-1} and the source term B^{m-1} are evaluated by the use of the values of the physical quantities at the previous step [$(m-1)$th step] at the nodes {P, E, W, N, S}. Equation (3.28) is also valid

at boundary control volumes if the coefficients a_{E}^{m-1}, ..., a_{S}^{m-1} that correspond to boundary nodes are set to be zero, and the boundary conditions are implemented by incorporating them in B^{m-1} (the treatment of the boundary condition will be discussed in Sec. 3.4.C). Thus the linear system of equations obtained by writing (3.28) for each control volume is closed and can be solved by standard numerical methods. In this way, a discretized solution ϕ^m for the mth step is obtained.

So far we have described how to construct the mth approximation of X^{A}, $\hat{T}_{(0)}$ and $\hat{v}_{i(1)}$ from their $(m-1)$th approximation using Eqs. (3.12), (3.13), and (3.15). Now we must also deal with the modified pressure $\hat{p}^\sharp_{(2)}$. However, there is no equation dominated by $\hat{p}^\sharp_{(2)}$; in fact the only occurrence of $\hat{p}^\sharp_{(2)}$ is in the form of a gradient in the momentum equation (3.15). This is a feature that the fluid-dynamic-type equations in this paper share with the incompressible Navier–Stokes equation, so it is suitable to attempt similar solution techniques. A well-known method is the SIMPLE algorithm.[26, 51, 52] In its original formulation,[51] it was described for a staggered grid, i.e., flow velocities were stored at cell surfaces rather than cell centers. For complicated geometries, however, it is more suitable to use a colocated grid, i.e., a grid system where all variables are stored at cell centers. A description of how to construct a solution method for a colocated grid in the case of the incompressible Navier–Stokes equation is found in Ref. [26].

The main idea is to use the continuity equation, Eq. (3.10), to derive an equation from which an updated value of $\hat{p}^\sharp_{(2)}$ can be obtained. We assume that from the previous step in the iterative process we already have a velocity field $\hat{v}_{i(1)}^{m-1}$ satisfying continuity, and a corresponding modified pressure field $\hat{p}^{\sharp m-1}_{(2)}$. Using these values to calculate the relevant coefficients and solving the linear algebraic system [Eq. (3.28) with P running all nodes], we obtain a velocity field $\hat{v}^*_{i(1)}$ that cannot be expected to

satisfy continuity. Therefore we introduce corrections $\hat{p}^{\sharp\prime}_{(2)}$ and $\hat{v}'_{i(1)}$, and set

$$\hat{p}^{\sharp m}_{(2)} = \hat{p}^{\sharp m-1}_{(2)} + \hat{p}^{\sharp\prime}_{(2)}, \tag{3.29a}$$

$$\hat{v}^{m}_{i(1)} = \hat{v}^{*}_{i(1)} + \hat{v}'_{i(1)}. \tag{3.29b}$$

Then, we assume that Eq. (3.10) is satisfied with $\hat{\rho}_{(0)} = \hat{\rho}^{m-1}_{(0)}$ [$(m-1)$th approximation of $\hat{\rho}_{(0)}$] and $\hat{v}_{i(1)} = \hat{v}^{m}_{i(1)}$ and integrate it over a control volume to obtain

$$\int_{\partial\Omega} \bar{n}_j \, \hat{\rho}^{m-1}_{(0)} \hat{v}^{m}_{j(1)} \, \mathrm{d}S = 0. \tag{3.30}$$

If we assume that there is a relation between the velocity correction and the pressure correction, for example, of the form

$$\hat{v}'_{i(1)} = c \frac{\partial \hat{p}^{\sharp\prime}_{(2)}}{\partial x_i}, \tag{3.31}$$

then we have, from Eqs. (3.29b) and (3.30),

$$\int_{\partial\Omega} \bar{n}_j \, \hat{\rho}^{m-1}_{(0)} \hat{v}^{*}_{j(1)} \, \mathrm{d}S + c \int_{\partial\Omega} \bar{n}_j \, \hat{\rho}^{m-1}_{(0)} \frac{\partial \hat{p}^{\sharp\prime}_{(2)}}{\partial x_j} \mathrm{d}S = 0. \tag{3.32}$$

This relation, which is similar to Eq. (3.23), leads to a linear algebraic system for the values of $\hat{p}^{\sharp\prime}_{(2)}$ at the grid points. However, the matrix for the resulting algebraic system is symmetric, and in addition it should be solved with high accuracy in each iteration to ensure convergence, so that in actual implementation it might be more appropriate to use a different solver for the linear algebraic system.

There is some freedom to choose a suitable relation (3.31) because for the converged solution the corrections should all go to zero. However, since we also want the velocity field to satisfy the conservation of momentum, a reasonable choice could be a relation based on the momentum equation. If we insert Eqs. (3.29a) and (3.29b) into the discretized momentum equation, Eq. (3.28) with $\phi = \hat{v}_{i(1)}$, and neglect the influence of the velocity corrections at the neighbouring nodes, then we have the relation

$$\hat{v}'_{i(1)} = -\frac{\Delta\Omega}{2a^{m-1}_{\mathrm{P}}(\hat{v}_{k(1)})} \frac{\partial \hat{p}^{\sharp\prime}_{(2)}}{\partial x_i}, \tag{3.33}$$

where $a_{\mathrm{P}}^{m-1}(\hat{v}_k)$ indicates a_{P}^{m-1} [see Eq. (3.28)] when $\phi = \hat{v}_k$. Note that a_{P}^{m-1} should be equal for $\hat{v}_{1(1)}$ and $\hat{v}_{2(1)}$ for computational efficiency. In particular, this should be kept in mind in implementation of the boundary conditions. Equation (3.33) is known as the SIMPLE approximation. In the present study, we use Eq. (3.33) as the relation (3.31).

Ideally, the same discretization of the pressure gradient term should be used in both the momentum equation (3.15) and the pressure correction equation (3.32). Unfortunately, doing this on a colocated grid gives rise to oscillations in the pressure field. To avoid these oscillations, we adopt the pressure-velocity coupling of Rhie and Chow.[54] The details are omitted here (see Ref. [26]).

3.4.C Boundary Conditions

The solution process described in Sec. 3.4.B is performed under the boundary conditions (3.8). The boundary conditions for X^{A}, $\hat{T}_{(0)}$, and the tangential component of $\hat{v}_{i(1)}$ can be straightforwardly implemented from Eq. (3.8) after substituting $\hat{n}_{(0)} = \hat{p}_{(0)}/\hat{T}_{(0)}$ and $X^{\mathrm{A}} = \hat{n}_{(0)}^{\mathrm{A}}/\hat{n}_{(0)}$. For example, Eqs. (3.8a) and (3.8b) give the condition for X^{A}, i.e.,

$$X^{\mathrm{A}} = \hat{p}_{\mathrm{w}}^{\mathrm{A}}/\hat{p}_{(0)}. \tag{3.34}$$

On the other hand, the boundary condition for the normal component of the barycentric velocity can be obtained from Eq. (3.8c) in combination with Eqs. (3.6c) and (3.5e):

$$n_i \hat{v}_{i(1)} = -\frac{\hat{m}^{\mathrm{A}} \hat{D}_{\mathrm{AB}} \hat{T}_{(0)}^{1/2}}{\hat{\rho}_{(0)}\,(1 - X^{\mathrm{A}})} n_i \left(\frac{\partial X^{\mathrm{A}}}{\partial x_i} + \frac{k_T}{\hat{T}_{(0)}} \frac{\partial \hat{T}_{(0)}}{\partial x_i} \right). \tag{3.35}$$

When the mixture is confined in a closed domain V, it may be more natural to specify the average amount of the noncondensable gas inside the domain, rather than to specify the constant $\hat{p}_{(0)}$ directly. As the former quantity, we choose a dimensionless parameter $n_{\mathrm{av}}^{\mathrm{B}}/n_0$, where $n_{\mathrm{av}}^{\mathrm{B}}$ is the (dimensional) average number density of the

noncondensable gas in the domain, which is expressed as

$$\frac{n_{\mathrm{av}}^{\mathrm{B}}}{n_0} = \frac{1}{V}\int_{\mathrm{V}} \hat{n}_{(0)}^{\mathrm{B}} \mathrm{d}V, \tag{3.36}$$

with the condition $\int_{\mathrm{V}} \hat{n}_{(m)}^{\mathrm{B}} \mathrm{d}V = 0$ $(m \geq 1)$, where V is the volume of V in the x_i space. Then, $\hat{p}_{(0)}$ is expressed in the following form:

$$\hat{p}_{(0)} = \left(\int \frac{1}{\hat{T}_{(0)}} \left(1 - X^{\mathrm{A}}\right) \mathrm{d}V \right)^{-1} V \frac{n_{\mathrm{av}}^{\mathrm{B}}}{n_0}. \tag{3.37}$$

Therefore, $\hat{p}_{(0)}$ is computed as a part of the iterative process.

It should be noted that a factor $(1 - X^{\mathrm{A}})$ is contained in the denominator in Eq. (3.35). The expression is theoretically sound even in the case where the local concentration of noncondensable gas approaches zero, because the concentration gradient and the coefficient k_T both also go to zero in the limit. However, when the expression is discretized in the course of numerical analysis, the induced error could be large and cause divergence. This is more likely to occur for small values of $n_{\mathrm{av}}^{\mathrm{B}}$. In fact, if $\hat{p}_{(0)}$ is computed from Eq. (3.37) during the iteration process, it is quite possible that at some point $\hat{p}_{(0)} < \hat{p}_{\mathrm{w}}^{\mathrm{A}}$ which unphysically implies that $X^{\mathrm{A}} > 1$. Although this will cause trouble for the boundary condition (3.35), the rest of the equations are not greatly affected, and will still converge towards a solution. If in the final solution $X^{\mathrm{A}} \leq 1$ everywhere, we can overlook the fact that somewhere during the solution process there was an unphysical solution. It is therefore enough to find an alternate boundary condition for the normal flow velocity in the case where X^{A} is close to unity, for example by setting the boundary normal velocity so that the continuity equation is satisfied in the control volume next to the wall.

Furthermore, our treatment of pressure requires continuity to be satisfied globally in each iteration, and thus the normal velocity boundary condition must be consistent with continuity. The evaporation and condensation should balance each other exactly. In the general case it cannot be known beforehand exactly where on the boundary evaporation takes place and where condensation takes place. The part of the wall that

has condensation can be identified by checking where the normal velocity is directed towards the wall. Integrating the normal velocity across this area, the total amount of condensation C_{tot} is obtained. In a similar way, the total amount of evaporation E_{tot} can be obtained. The normal velocity boundary value in the evaporating region is then multiplied by $C_{\mathrm{tot}}/E_{\mathrm{tot}}$ everywhere to make the evaporation and condensation balance.

3.5 Applications

In this section, we apply the fluid-dynamic-type system summarized in Sec. 3.3 to a specific problem.

3.5.A Two-plate problem

We consider first a simple one-dimensional problem of a vapor-gas mixture contained between plane walls consisting of the condensed phase of the vapor and located between $0 \leq X_2 \leq D_0$. Let the temperature and saturated number density of vapor at the wall at $X_2 = 0$ be T_0 and n_0^{A}, and at $X_2 = D_0$ be T_1 and n_1^{A}. (We choose n_0^{A} as the reference number density, i.e. $n_0^{\mathrm{A}} = n_0$.) This problem has already been investigated for various parameter settings in Ref. [14], and our purpose is to verify the numerical method and clarify the necessary grid requirements. In Fig. 3.2 the barycentric flow velocity, the temperature, and the concentration of the vapor is shown for three different grids with the same number of control volumes but different degree of non-uniformness. The parameter setting is as follows: $m^{\mathrm{B}}/m^{\mathrm{A}}$=0.2, $d^{\mathrm{B}}/d^{\mathrm{A}}$=0.5, T_1/T_0=1.1, $n_1^{\mathrm{A}}/n_0^{\mathrm{A}}$=4 and $n_{\mathrm{av}}^{\mathrm{B}}$=0.2. Because the amount of noncondensable gas is relatively small this is quite an extreme case, in which almost all of the noncondensable gas gathers in the vicinity of the condensing plate. Furthermore, it was shown in [14] that when the molecules are not mechanically identical, the temperature profile is not monotonic. In the case shown in Fig. 3.2 this is examplified by an undershoot

in the temperature profile near the condensing plate. It is important that the grid is fine enough to accurately resolve this kind of large variations in the gas behavior near walls. Near the channel center, however, there is seldom need for high resolution, and since there is an adverse relation between the number of node points and the computational time, it is preferable to use a non-uniform grid. In Fig. 3.2 all the grids used have 120 node points, whereas the grid parameter r (see Fig. 2.1) is set to 0.5 (long dashed line), 0.4936 (short dashed line) and 0.4872 (solid line). The curves are shown together with black squares representing sample points from the solution of Ref. [14], which incidentally used a finite difference method and a uniform grid with 399 inner node points.

3.5.B Flow through a sinusoidal channel

Now let us consider a slightly rarefied gas mixture of a vapor and a noncondensable gas, contained between two walls of sinusoidal shape, located at

$$X_2 = \pm\frac{L_0}{2}\left(1 - \hat{D}\sin\frac{2\pi X_1}{L_0}\right), \tag{3.38}$$

where $0 \leq \hat{D} < 1$ (Fig. 3.3). Both walls, consisting of the condensed phase of the vapor, have a common temperature $T_{\rm w}$. We assume that the wall temperature $T_{\rm w}$ and the corresponding saturation number density $n_{\rm w}^{\rm A}$ have the following sinusoidal distribution:

$$T_{\rm w} = T_0\left(1 - \hat{T}_{\rm c}\cos\frac{2\pi X_1}{L_0}\right), \tag{3.39a}$$

$$n_{\rm w}^{\rm A} = n_0\left(1 - \hat{n}_{\rm c}^{\rm A}\cos\frac{2\pi X_1}{L_0}\right), \tag{3.39b}$$

where $0 \leq \hat{T}_{\rm c} < 1$ and $0 \leq \hat{n}_c^{\rm A} < 1$. In terms of the dimensionless variables, Eqs. (3.38), (3.39a), and (3.39b) become

$$x_2 = \pm(1/2)[1 - \hat{D}\sin(2\pi x_1)], \tag{3.40a}$$

$$\hat{T}_{\rm w} = 1 - \hat{T}_{\rm c}\cos(2\pi x_1), \tag{3.40b}$$

$$\hat{n}_{\rm w}^{\rm A} = 1 - \hat{n}_{\rm c}^{\rm A}\cos(2\pi x_1). \tag{3.40c}$$

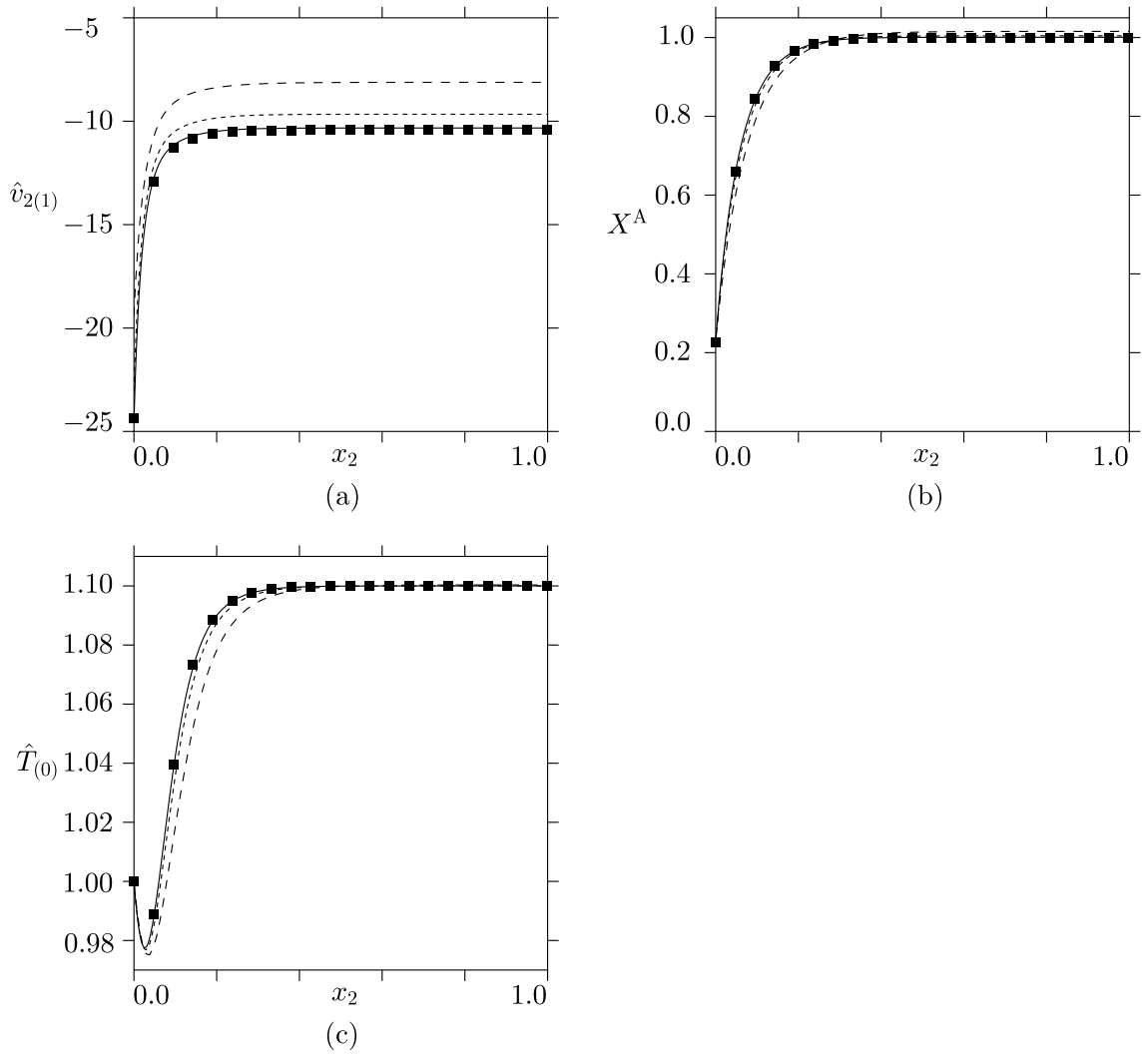

FIGURE 3.2: Two-surface problem of evaporation and condensation in the presence of a noncondensable gas [$m^{\mathrm{B}}/m^{\mathrm{A}}$=0.2, $d^{\mathrm{B}}/d^{\mathrm{A}}$=0.5, T_1/T_0=1.1, $n_1^{\mathrm{A}}/n_0^{\mathrm{A}}$=4 and $n_{\mathrm{av}}^{\mathrm{B}}$=0.2]; showing (a) flow velocity $\hat{v}_{2(2)}$, (b) concentration X^{A}, and (c) temperature $\hat{T}_{(0)}$. In all figures the long dashed line represents a uniform grid, the short dashed line a non-uniform grid with grid parameter r=0.4936, and the solid line r=0.4872. Comparison is made with the solution originally presented in Ref. [14], shown as black squares at sample points.

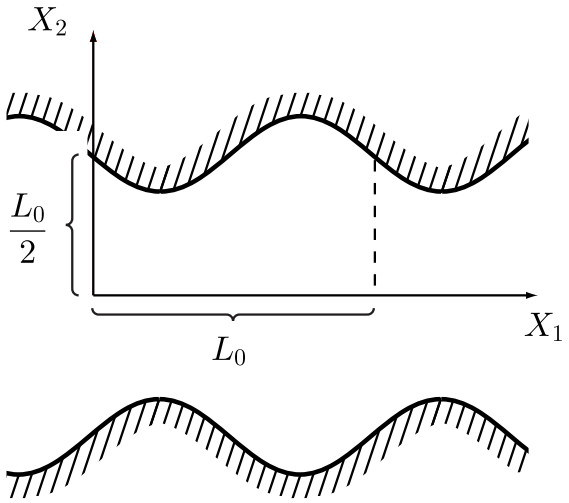

FIGURE 3.3: Geometry.

We assume that the solution is symmetric with respect to $x_2 = 0$ and is periodic with period 1 in x_1 and consider the domain $0 \leq x_1 \leq 1$ and $0 \leq x_2 \leq (1/2)[1 - \hat{D}\sin(2\pi x_1)]$, imposing the symmetry condition at $x_2 = 0$, and the periodic condition at $x_1 = 0$ and 1. Thus, $n^{\mathrm{B}}_{\mathrm{av}}$ is the average molecular number density in this domain. We analyze the behavior of the gas mixture numerically, using the fluid-dynamic-type system in Sec. 3.3, under the assumption that the amount of noncondensable gas is comparable to that of the vapor, i.e., $n^{\mathrm{B}}_{\mathrm{av}}/n_0$ is of the order of unity. If we take m^{A} and d^{A} as the reference molecular mass m_0 and diameter d_0, then the problem is characterized by the following dimensionless parameters: $m^{\mathrm{B}}/m^{\mathrm{A}}$, $d^{\mathrm{B}}/d^{\mathrm{A}}$, $\hat{D}$, $\hat{T}_{\mathrm{c}}$, $\hat{n}^{\mathrm{A}}_{\mathrm{c}}$, and $n^{\mathrm{B}}_{\mathrm{av}}/n_0$.

In the following, we mainly show the result in the case of plane ($\hat{D} = 0$) and isothermal ($\hat{T}_{\mathrm{c}} = 0$) walls. The assumption of isothermal walls seems unphysical because the saturation pressure $p^{\mathrm{A}}_{\mathrm{w}}$ (or the saturation number density $n^{\mathrm{A}}_{\mathrm{w}}$) depends on the temperature T_{w}. But, we consider an idealized case to simplify the physical situation. This idealization is acceptable because of the fact that in general a small variation of T_{w} results in a large variation of $p^{\mathrm{A}}_{\mathrm{w}}$.

In Figs. 3.4–3.8, we show some results for different mass ratios in the case of

$d^{\mathrm{B}}/d^{\mathrm{A}} = 1$, $\hat{D} = 0$ (plane walls), $\hat{T}_{\mathrm{c}} = 0$ (isothermal walls), $\hat{n}_{\mathrm{c}}^{\mathrm{A}} = 0.5$, and $n_{\mathrm{av}}^{\mathrm{B}}/n_0 = 0.8$. Figure 3.4 shows the first order coefficient of the vapor flow velocity $\hat{v}_{i(1)}^{\mathrm{A}}$, Fig. 3.5 that of the noncondensable gas flow velocity $\hat{v}_{i(1)}^{\mathrm{B}}$, and Fig. 3.6 that of the barycentric flow velocity $\hat{v}_{i(1)}$; in each figure, panel (a) shows the result for $m^{\mathrm{B}}/m^{\mathrm{A}} = 0.2$, panel (b) for $m^{\mathrm{B}}/m^{\mathrm{A}} = 1$, and panel (c) for $m^{\mathrm{B}}/m^{\mathrm{A}} = 5$. Since the flow field is symmetric with respect to $x_1 = 1/2$ in the case of plane walls, only the part $0 \le x_1 \le 1/2$ and $0 \le x_2 \le 1/2$ is shown in the figures. In the left-hand figures, the arrow indicates the flow velocity vector $\hat{v}_{i(1)}^{\mathrm{A}}$, $\hat{v}_{i(1)}^{\mathrm{B}}$, or $\hat{v}_{i(1)}$ in the x_1-x_2 plane at its starting point, and its scale is shown in each figure. The right-hand figures show the streamlines of the corresponding flow velocities. Figure 3.7, on the other hand, shows the isolines of the concentration of the vapor X^{A} based on the leading-order number density for $m^{\mathrm{B}}/m^{\mathrm{A}} = 0.2$, 1, and 5 in the same domain. Figure 3.8 shows the distribution of the leading-order temperature $\hat{T}_{(0)}$ along the lines $x_1 = 0$ and 0.5 for various values of $m^{\mathrm{B}}/m^{\mathrm{A}}$ in the case where the other parameters are the same as in Figs. 3.4–3.7.

The vapor evaporating from the part of the wall with high saturation number density, flows back to the wall forming half-loop streamlines, and condenses on the part with low saturation number density ($n_{\mathrm{w}}^{\mathrm{A}} < n_0$) (Fig. 3.4). This flow of the vapor induces a circulating flow of the noncondensable gas (Fig. 3.5). As the molecular mass of the noncondensable gas increases ($m^{\mathrm{B}}/m^{\mathrm{A}} = 0.2 \to 1 \to 5$), the speed of the vapor flow as well as that of the resulting noncondensable gas flow decreases because the impeding effect on evaporation and condensation caused by the presence of the noncondensable gas increases. The barycentric velocity is subject to the velocity slip on the wall described by Eq. (3.8d). In the case of isothermal walls, the velocity slip is due to the diffusion slip (the slip proportional to b_9). When $m^{\mathrm{B}}/m^{\mathrm{A}} = 1$ (and $d^{\mathrm{B}}/d^{\mathrm{A}} = 1$), the coefficient b_9 becomes zero, so that the tangential component of the barycentric flow velocity vanishes on the wall [Fig. 3.6(b)]. The diffusion slip is leftward in Fig. 3.6(a) and rightward in Fig. 3.6(c). As the result, a circulation appears

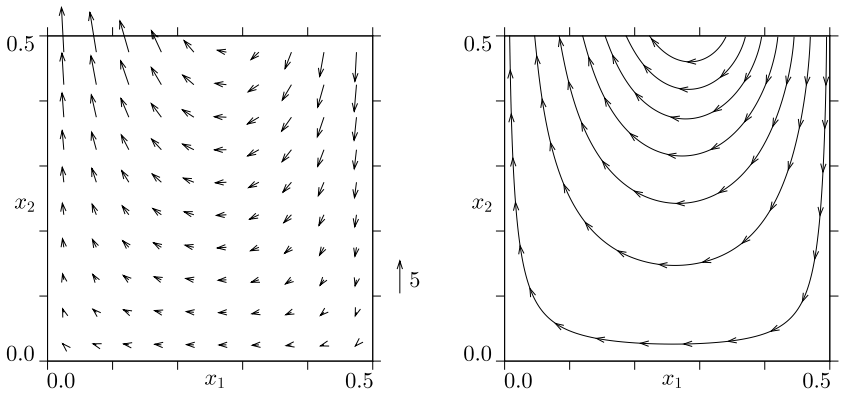

(a) $m^{\mathrm{B}}/m^{\mathrm{A}} = 0.2$

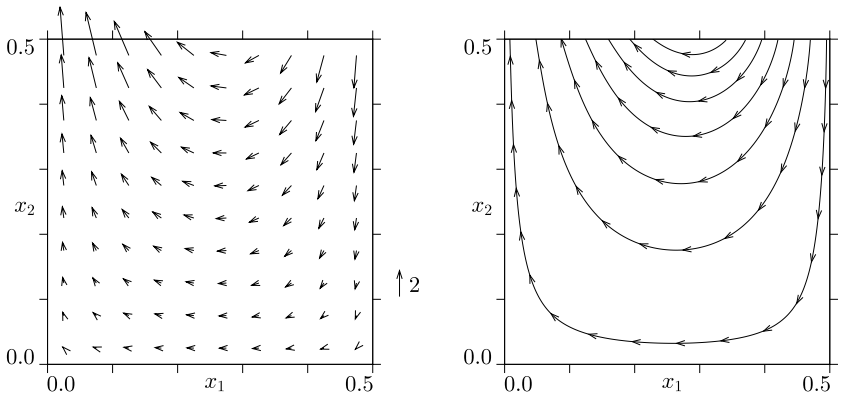

(b) $m^{\mathrm{B}}/m^{\mathrm{A}} = 1$

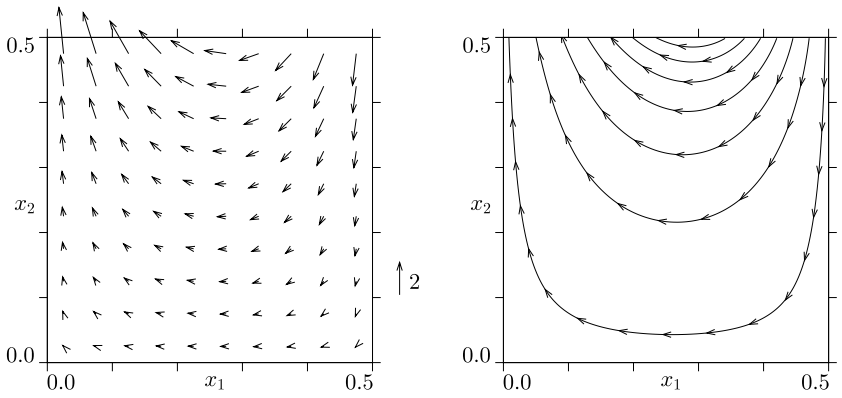

(c) $m^{\mathrm{B}}/m^{\mathrm{A}} = 5$

FIGURE 3.4: The first-order coefficient $\hat{v}^{\mathrm{A}}_{i(1)}$ of the flow velocity of the vapor for different $m^{\mathrm{B}}/m^{\mathrm{A}}$ in the domain $0 \le x_1 \le 1/2$ and $0 \le x_2 \le 1/2$ [$d^{\mathrm{B}}/d^{\mathrm{A}} = 1$, $\hat{D} = 0$ (plane walls), $\hat{T}_{\mathrm{c}} = 0$ (isothermal walls), $\hat{n}^{\mathrm{A}}_{\mathrm{c}} = 0.5$, and $n^{\mathrm{B}}_{\mathrm{av}}/n_0 = 0.8$]. (a) $m^{\mathrm{B}}/m^{\mathrm{A}} = 0.2$, (b) $m^{\mathrm{B}}/m^{\mathrm{A}} = 1$, (c) $m^{\mathrm{B}}/m^{\mathrm{A}} = 5$. In the left-hand figures, the arrow indicates the flow velocity vector $\hat{v}^{\mathrm{A}}_{i(1)}$ in the x_1-x_2 plane at its starting point, and its scale is shown in each figure. The right-hand figures show the streamlines of the corresponding flow velocities.

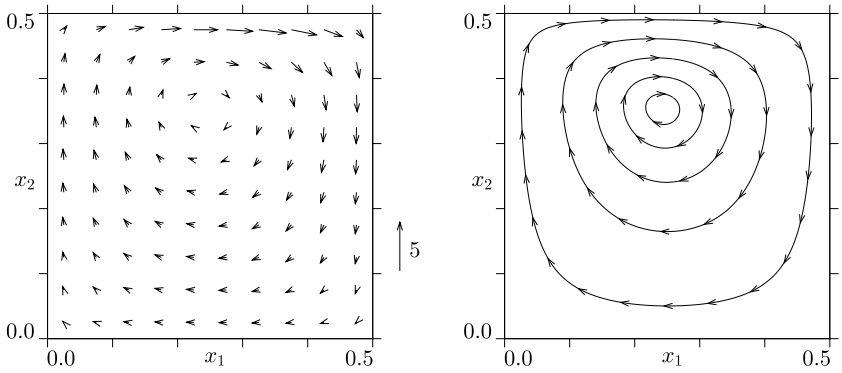

(a) $m^{\mathrm{B}}/m^{\mathrm{A}} = 0.2$

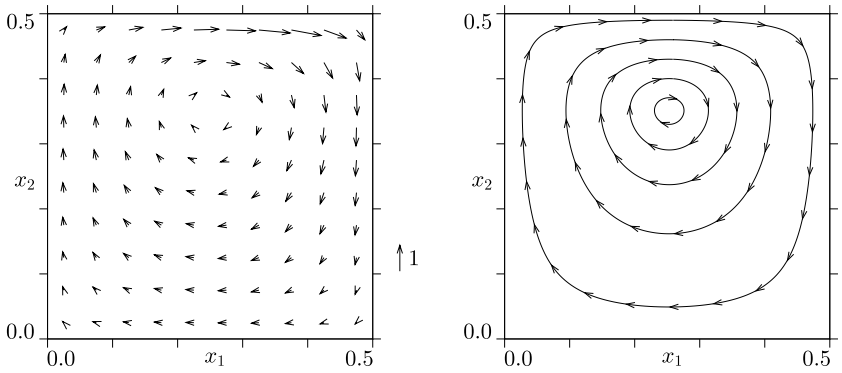

(b) $m^{\mathrm{B}}/m^{\mathrm{A}} = 1$

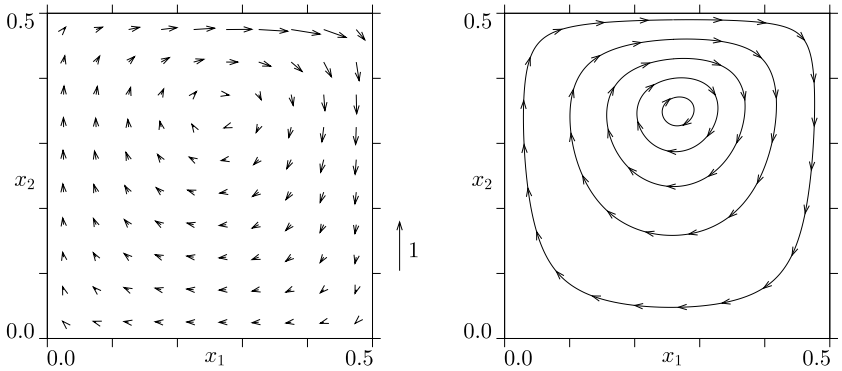

(c) $m^{\mathrm{B}}/m^{\mathrm{A}} = 5$

FIGURE 3.5: The first-order coefficient $\hat{v}^{\mathrm{B}}_{i(1)}$ of the flow velocity of the noncondensable gas for different $m^{\mathrm{B}}/m^{\mathrm{A}}$ in the domain $0 \le x_1 \le 1/2$ and $0 \le x_2 \le 1/2$ [$d^{\mathrm{B}}/d^{\mathrm{A}} = 1$, $\hat{D} = 0$ (plane walls), $\hat{T}_{\mathrm{c}} = 0$ (isothermal walls), $\hat{n}^{\mathrm{A}}_{\mathrm{c}} = 0.5$, and $n^{\mathrm{B}}_{\mathrm{av}}/n_0 = 0.8$]. (a) $m^{\mathrm{B}}/m^{\mathrm{A}} = 0.2$, (b) $m^{\mathrm{B}}/m^{\mathrm{A}} = 1$, (c) $m^{\mathrm{B}}/m^{\mathrm{A}} = 5$. In the left-hand figures, the arrow indicates the flow velocity vector $\hat{v}^{\mathrm{B}}_{i(1)}$ in the x_1-x_2 plane at its starting point, and its scale is shown in each figure. The right-hand figures show the streamlines of the corresponding flow velocities.

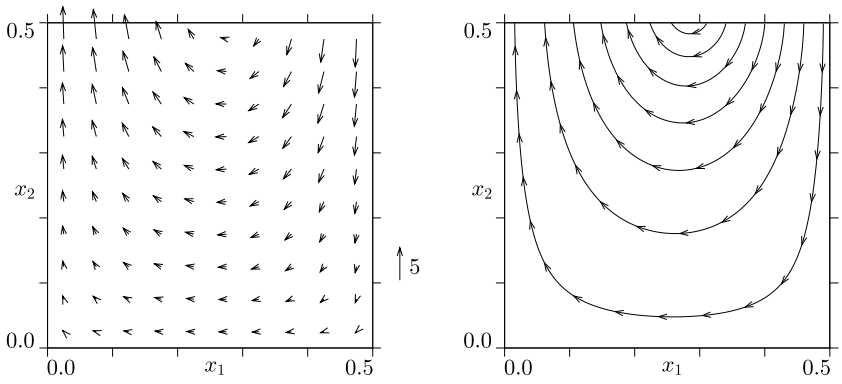

(a) $m^{\mathrm{B}}/m^{\mathrm{A}} = 0.2$

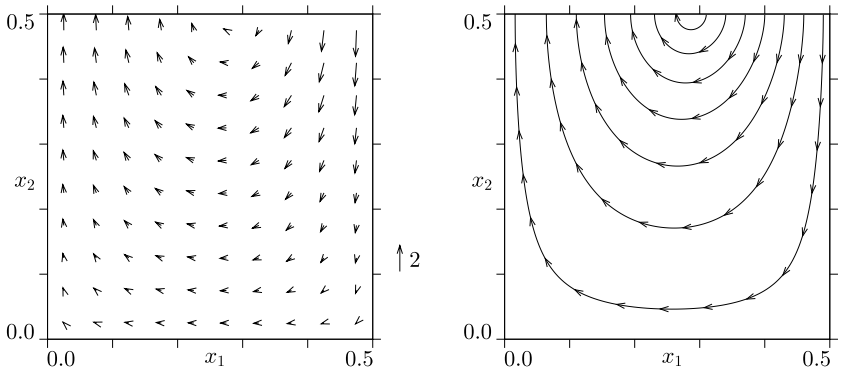

(b) $m^{\mathrm{B}}/m^{\mathrm{A}} = 1$

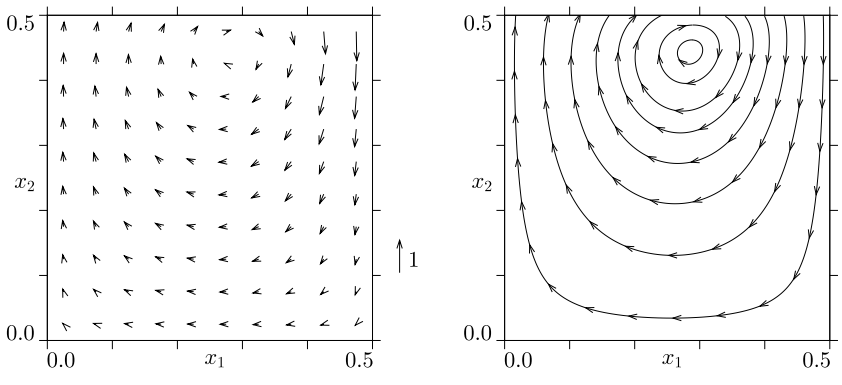

(c) $m^{\mathrm{B}}/m^{\mathrm{A}} = 5$

FIGURE 3.6: The first-order coefficient $\hat{v}_{i(1)}$ of the barycentric flow velocity for different $m^{\mathrm{B}}/m^{\mathrm{A}}$ in the domain $0 \leq x_1 \leq 1/2$ and $0 \leq x_2 \leq 1/2$ [$d^{\mathrm{B}}/d^{\mathrm{A}} = 1$, $\hat{D} = 0$ (plane walls), $\hat{T}_{\mathrm{c}} = 0$ (isothermal walls), $\hat{n}_{\mathrm{c}}^{\mathrm{A}} = 0.5$, and $n_{\mathrm{av}}^{\mathrm{B}}/n_0 = 0.8$]. (a) $m^{\mathrm{B}}/m^{\mathrm{A}} = 0.2$, (b) $m^{\mathrm{B}}/m^{\mathrm{A}} = 1$, (c) $m^{\mathrm{B}}/m^{\mathrm{A}} = 5$. In the left-hand figures, the arrow indicates the flow velocity vector $\hat{v}_{i(1)}$ in the x_1-x_2 plane at its starting point, and its scale is shown in each figure. The right-hand figures show the streamlines of the corresponding flow velocities.

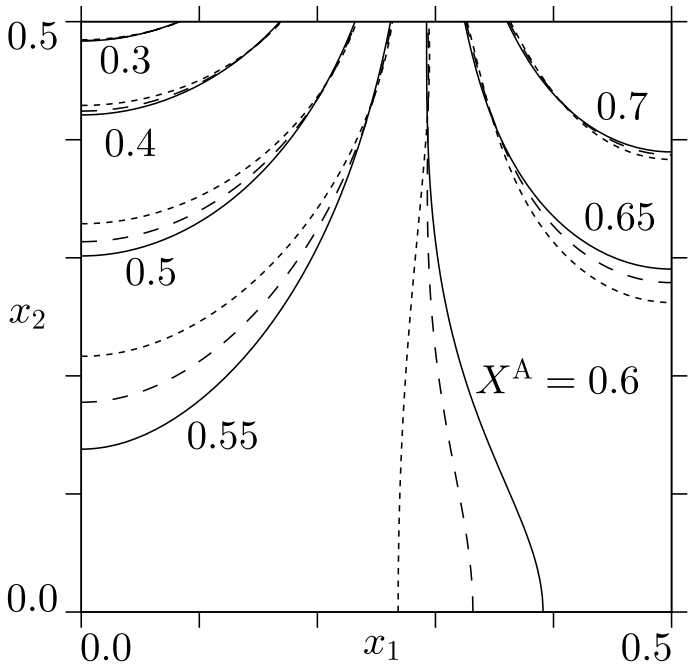

FIGURE 3.7: The isolines of the concentration of the vapor X^{A} based on the leading-order molecular number density for different $m^{\mathrm{B}}/m^{\mathrm{A}}$ in the domain $0 \le x_1 \le 1/2$ and $0 \le x_2 \le 1/2$ [$d^{\mathrm{B}}/d^{\mathrm{A}} = 1$, $\hat{D} = 0$ (plane walls), $\hat{T}_{\mathrm{c}} = 0$ (isothermal walls), $\hat{n}_{\mathrm{c}}^{\mathrm{A}} = 0.5$, and $n_{\mathrm{av}}^{\mathrm{B}}/n_0 = 0.8$]. The short dashed line indicates the result for $m^{\mathrm{B}}/m^{\mathrm{A}} = 0.2$, the long dashed line that for $m^{\mathrm{B}}/m^{\mathrm{A}} = 1$, and the solid line that for $m^{\mathrm{B}}/m^{\mathrm{A}} = 5$.

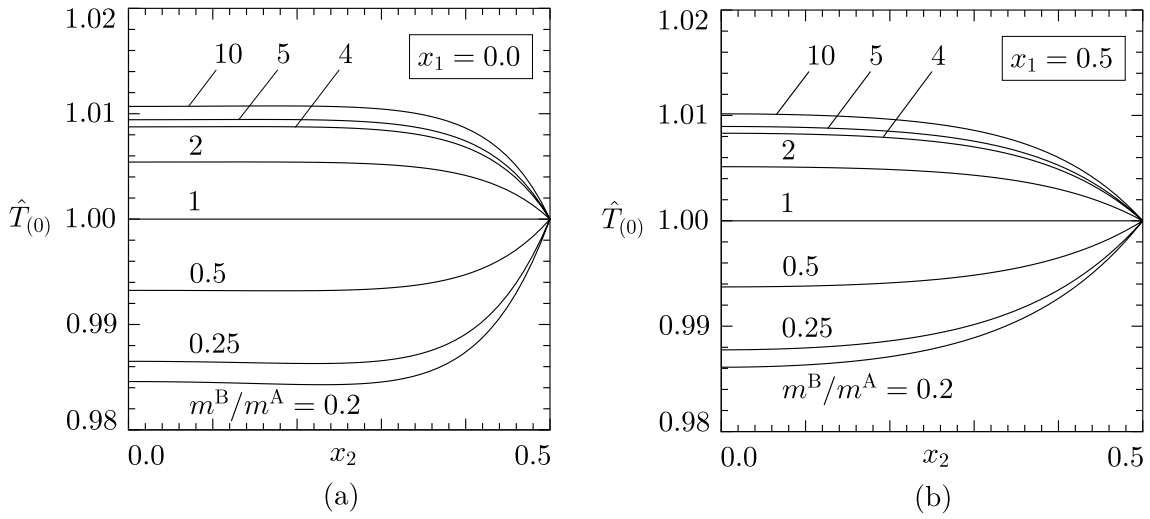

FIGURE 3.8: The distribution of the leading-order temperature $\hat{T}_{(0)}$ along the lines $x_1 = 0$ and 0.5 for various values of $m^{\mathrm{B}}/m^{\mathrm{A}}$ [$d^{\mathrm{B}}/d^{\mathrm{A}} = 1$, $\hat{D} = 0$ (plane walls), $\hat{T}_{\mathrm{c}} = 0$ (isothermal walls), $\hat{n}_{\mathrm{c}}^{\mathrm{A}} = 0.5$, and $n_{\mathrm{av}}^{\mathrm{B}}/n_0 = 0.8$]. (a) $x_1 = 0$, (b) $x_1 = 0.5$.

in the latter figure. According to Fig. 3.7, the distribution of the concentration of the vapor is almost independent of $m^{\mathrm{B}}/m^{\mathrm{A}}$ near the walls. Although the temperature of the walls is uniform, there appears a slight nonuniformity in the temperature $\hat{T}_{(0)}$, as shown in Fig. 3.8. That is, there is a slight heating for $m^{\mathrm{B}}/m^{\mathrm{A}} > 1$ and cooling for $m^{\mathrm{B}}/m^{\mathrm{A}} < 1$, the temperature being uniform for $m^{\mathrm{B}}/m^{\mathrm{A}} = 1$ (although the temperature distribution is shown only at $x_1 = 0$ and 0.5 in Fig. 3.8, the above statement is true for any other x_1).

If one tries to solve the present problem within the framework of continuum fluid dynamics, natural fluid-dynamic equations would be the compressible Navier–Stokes equations with slow motion, which is equivalent to Eqs. (3.5a)–(3.5e) with $\hat{\Upsilon}_1 = \hat{\Upsilon}_2 = \hat{\Upsilon}_3 = \hat{\Upsilon}_4 = \hat{\Upsilon}_5 = 0$. On the other hand, the boundary condition corresponding to Eq. (3.8a) is usually assumed from considerations on the physical nature of the surface of the condensed phase and the structure of the Navier–Stokes equations. Other boundary conditions based on macroscopic considerations would be the conditions equivalent to Eqs. (3.8b) and (3.8c), and the no-slip condition for the tangential flow velocity, i.e., Eq. (3.8d) with $b_7 = b_9 = 0$. Therefore, we call the system consisting of Eqs. (3.5a)–(3.5e) with $\hat{\Upsilon}_1 = \hat{\Upsilon}_2 = \hat{\Upsilon}_3 = \hat{\Upsilon}_4 = \hat{\Upsilon}_5 = 0$ and boundary conditions (3.8a)–(3.8d) with $b_7 = b_9 = 0$ the Navier–Stokes system.[52, 55, 56, 57, 58] An example of the difference between the full fluid-dynamic-type system and the Navier–Stokes system is demonstrated in Fig. 3.9. More specifically, the streamlines of $\hat{v}_{i(1)}$ [Fig. 3.9(a)] and the isolines of X^{A} [Fig. 3.9(b)] obtained by the respective systems are compared for $m^{\mathrm{B}}/m^{\mathrm{A}} = 5$, $d^{\mathrm{B}}/d^{\mathrm{A}} = 1$, $\hat{D} = 0$ (plane walls), $\hat{T}_{\mathrm{c}} = 0$ (isothermal walls), $\hat{n}^{\mathrm{A}}_{\mathrm{c}} = 0.5$, and $n^{\mathrm{B}}_{\mathrm{av}}/n_0 = 0.8$. A decisive difference is that there is a circulation in the barycentric velocity field in the case of the full fluid-dynamic-type system [Fig. 3.9(a)]. The difference in the concentration is less significant [Fig. 3.9(b)].

Figure 3.10 shows the result when a sinusoidal temperature distribution is imposed along the wall, i.e., when $\hat{T}_{\mathrm{c}} = 0.3$, in the case of $m^{\mathrm{B}}/m^{\mathrm{A}} = 5$, $d^{\mathrm{B}}/d^{\mathrm{A}} = 1$, $\hat{D} = 0$

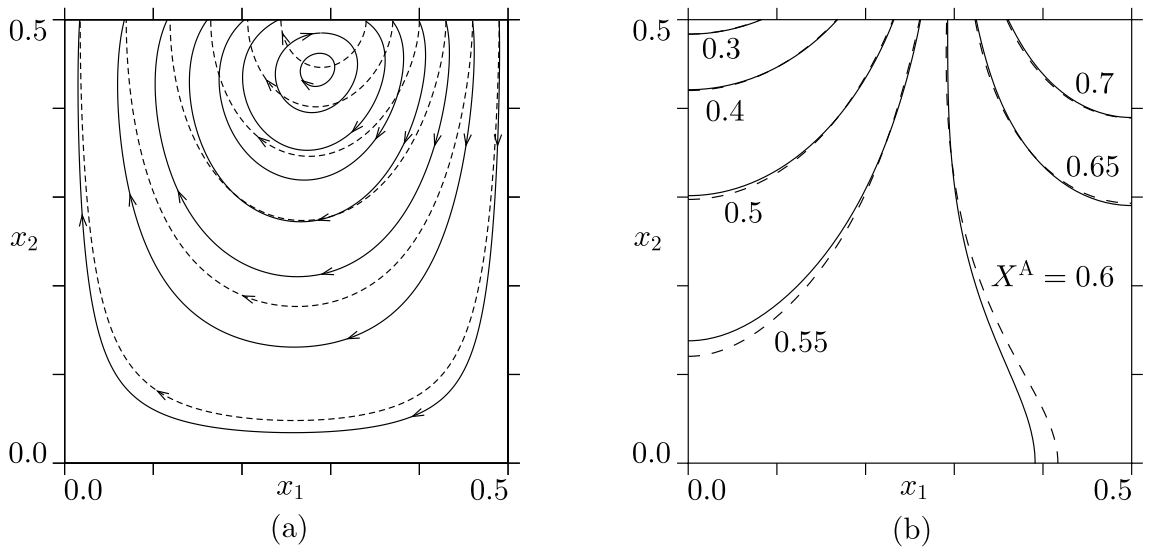

FIGURE 3.9: The difference between the full fluid-dynamic-type system and the Navier–Stokes system [$m^{\mathrm{B}}/m^{\mathrm{A}} = 5$, $d^{\mathrm{B}}/d^{\mathrm{A}} = 1$, $\hat{D} = 0$ (plane walls), $\hat{T}_{\mathrm{c}} = 0$ (isothermal walls), $\hat{n}_{\mathrm{c}}^{\mathrm{A}} = 0.5$, and $n_{\mathrm{av}}^{\mathrm{B}}/n_0 = 0.8$]. (a) streamlines of $\hat{v}_{i(1)}$, (b) isolines of X^{A}. Here, the solid line indicates the result by the full fluid-dynamic-type system, and the dashed line that by the Navier–Stokes system.

(plane walls), $\hat{n}_{\mathrm{c}}^{\mathrm{A}} = 0.5$, and $n_{\mathrm{av}}^{\mathrm{B}}/n_0 = 0.8$. Figure 3.10(a) shows the flow velocity vector of the barycentric velocity $\hat{v}_{i(1)}$, Fig. 3.10(b) the corresponding streamlines, Fig. 3.10(c), the isolines of the concentration of the vapor X^{A}, and Fig. 3.10(d) those of the temperature $\hat{T}_{(0)}$. The dashed line in Fig. 3.10(d) will be commented in the following paragraph. The corresponding isothermal case is shown in Figs. 3.6(c) and 3.7; more precisely, Fig. 3.6(c) corresponds to Figs. 3.10(a) and 3.10(b), and Fig. 3.7 (for $m^{\mathrm{B}}/m^{\mathrm{A}} = 5$) to Fig. 3.10(c). The flow pattern changes because the thermal slip [cf. Eq. (3.8d)] caused by the rightward temperature gradient enhances the velocity slip in the same direction.

Let us consider the continuum limit in the case of Fig. 3.10. As commented in Sec. 3.3.C, in this limit, the flow vanishes and the temperature field reduces to $\hat{T}_{(0)}$, which is shown by the solid line in Fig. 3.10(d). On the other hand, the dashed line in the same figure indicates the corresponding isolines of the temperature field given by the steady heat-conduction equation, that is, the solution of Eqs. (3.5d) and

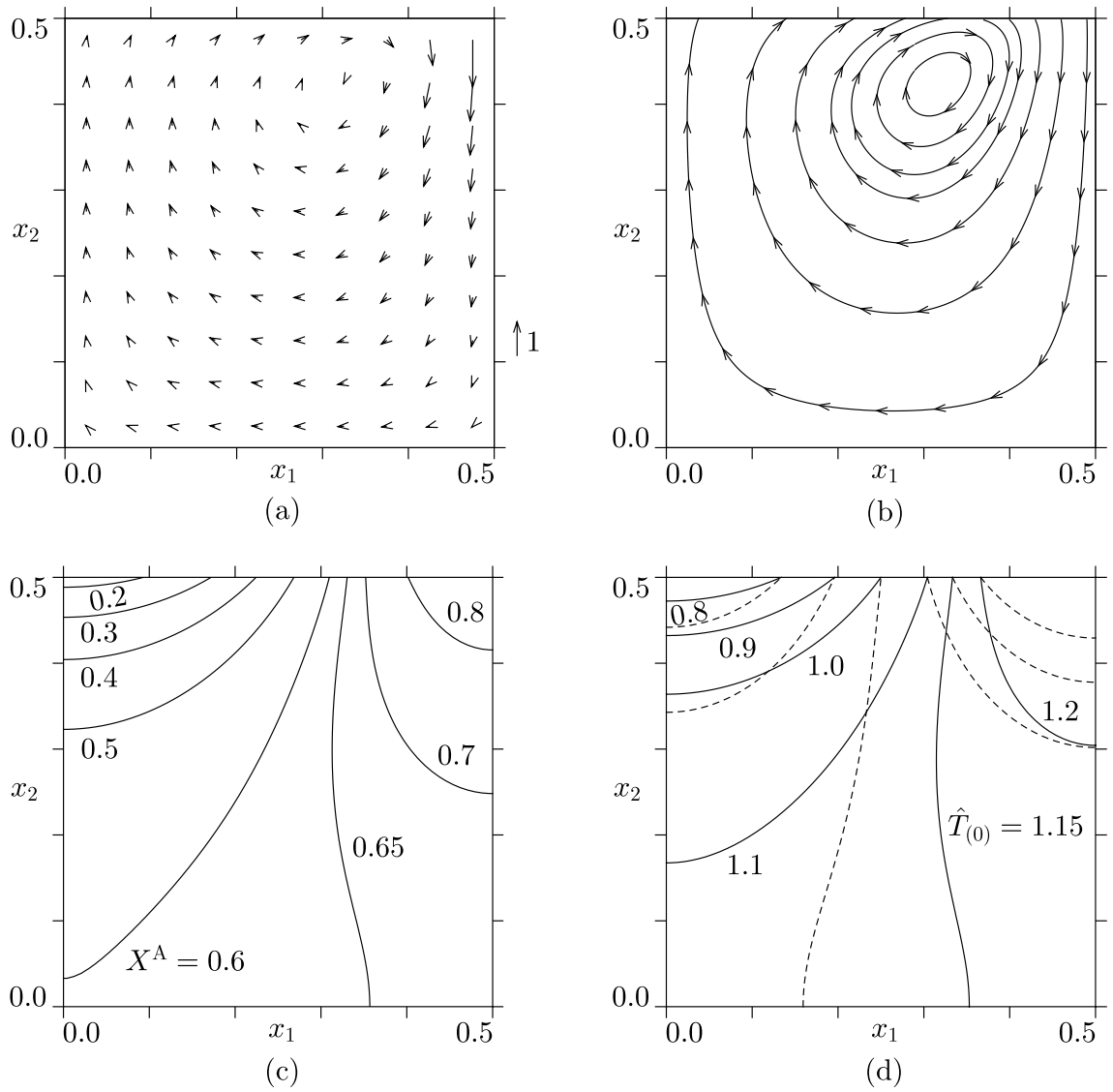

FIGURE 3.10: Flow field with a temperature variation along the walls [$m^{\mathrm{B}}/m^{\mathrm{A}} = 5$, $d^{\mathrm{B}}/d^{\mathrm{A}} = 1$, $\hat{D} = 0$ (plane walls), $\hat{T}_{\mathrm{c}} = 0.3$, $\hat{n}_{\mathrm{c}}^{\mathrm{A}} = 0.5$, and $n_{\mathrm{av}}^{\mathrm{B}}/n_0 = 0.8$]. (a) flow velocity field of $\hat{v}_{i(1)}$, (b) streamlines of $\hat{v}_{i(1)}$, (c) isolines of X^{A}, (d) isolines of $\hat{T}_{(0)}$ (solid line). In (a), the arrow indicates the flow velocity vector $\hat{v}_{i(1)}$ in the x_1-x_2 plane at its starting point, and its scale is shown in the figure. In (d), the dashed line indicates the corresponding isolines of the temperature field by the steady heat-conduction equation
.

(3.5e) with $\hat{v}^{\mathrm{A}}_{j(1)} = \hat{v}^{\mathrm{B}}_{j(1)} = 0$ and the boundary condition (3.8b) for the same values of the parameters. In this case, in place of the condition (3.8a), we need to specify a parameter associated with the amount of the component A. Here, the total amount of the component A is set to be equal to that of the vapor in the numerical result in the case of the mixture of the vapor and noncondensable gas. Since the dashed lines coincide with the corresponding solid lines on the wall, their labels are omitted. As is seen from the figure, the correct temperature field differs significantly from that given by the heat-conduction equation. This discrepancy is caused by the ghost effect.

In Figs. 3.11 and 3.13, the result for walls of sinusoidal shape ($\hat{D} = 0.1$) is shown for $\hat{T}_{\mathrm{c}} = 0$ (Fig. 3.11) and 0.3 (Fig. 3.13) in the case of $m^{\mathrm{B}}/m^{\mathrm{A}} = 5$, $d^{\mathrm{B}}/d^{\mathrm{A}} = 1$, $\hat{n}^{\mathrm{A}}_{\mathrm{c}} = 0.5$, and $n^{\mathrm{B}}_{\mathrm{av}}/n_0 = 0.8$. Since the flow field is not symmetric with respect to $x_1 = 0.5$, it is shown in the full period $0 \le x_1 \le 1$. In each figure, panel (a) shows the barycentric flow velocity vector $\hat{v}_{i(1)}$, panel (b) the corresponding streamlines, and panel (c) the isolines of the concentration of the vapor X^{A}. Figure 11(d) shows the isolines of the temperature $\hat{T}_{(0)}$. Since the temperature variation is very small in the case of Fig. 3.11, the isothermal lines are not shown there.

The fluid-dynamic-type system has been solved on a 240×120 nonuniform grid with finer control volumes near the wall (although for some cases the solution has been compared with the solution of double grid-size to ensure the accuracy). All computations were carried out on a Dell Workstation running an Intel Pentium 4 (2.2 GHz) CPU, or a computer of equivalent capacity.

3.5.C Comparison with DSMC result

We also investigate the same problem, in the case of plane ($\hat{D} = 0$) and isothermal ($\hat{T}_{\mathrm{c}} = 0$) walls, numerically on the basis of kinetic theory, using the DSMC method.[27, 28] In this subsection, we show some results, which will be compared with the results based on the fluid-dynamic-type system. Since the flow field is symmetric with respect to $x_2 = 0$, $x_1 = 0$, and $x_1 = 0.5$, the computation is performed in the domain

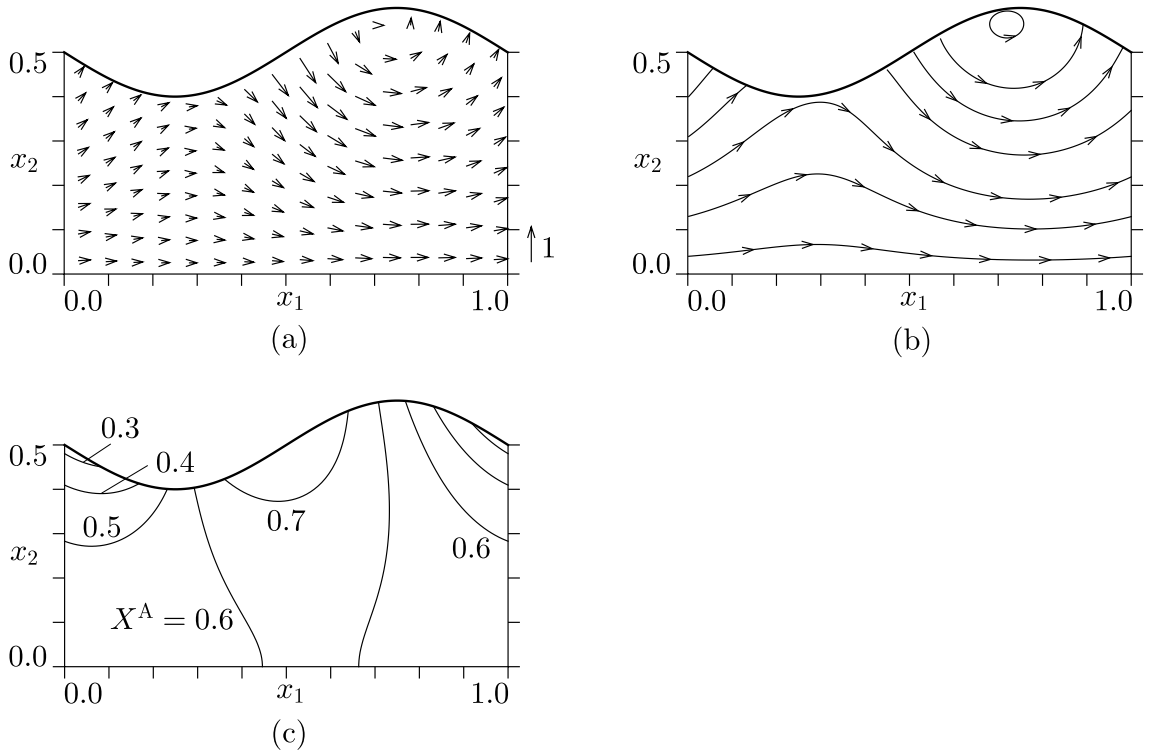

FIGURE 3.11: Flow field for isothermal walls of sinusoidal shape ($m^{\mathrm{B}}/m^{\mathrm{A}} = 5$, $d^{\mathrm{B}}/d^{\mathrm{A}} = 1$, $\hat{D} = 0.1$, $\hat{T}_{\mathrm{c}} = 0$, $\hat{n}_{\mathrm{c}}^{\mathrm{A}} = 0.5$, and $n_{\mathrm{av}}^{\mathrm{B}}/n_0 = 0.8$). (a) flow velocity field of $\hat{v}_{i(1)}$, (b) streamlines of $\hat{v}_{i(1)}$, (c) isolines of X^{A}. In (a), the arrow indicates the vector $\hat{v}_{i(1)}$, and its scale is shown in the figure.

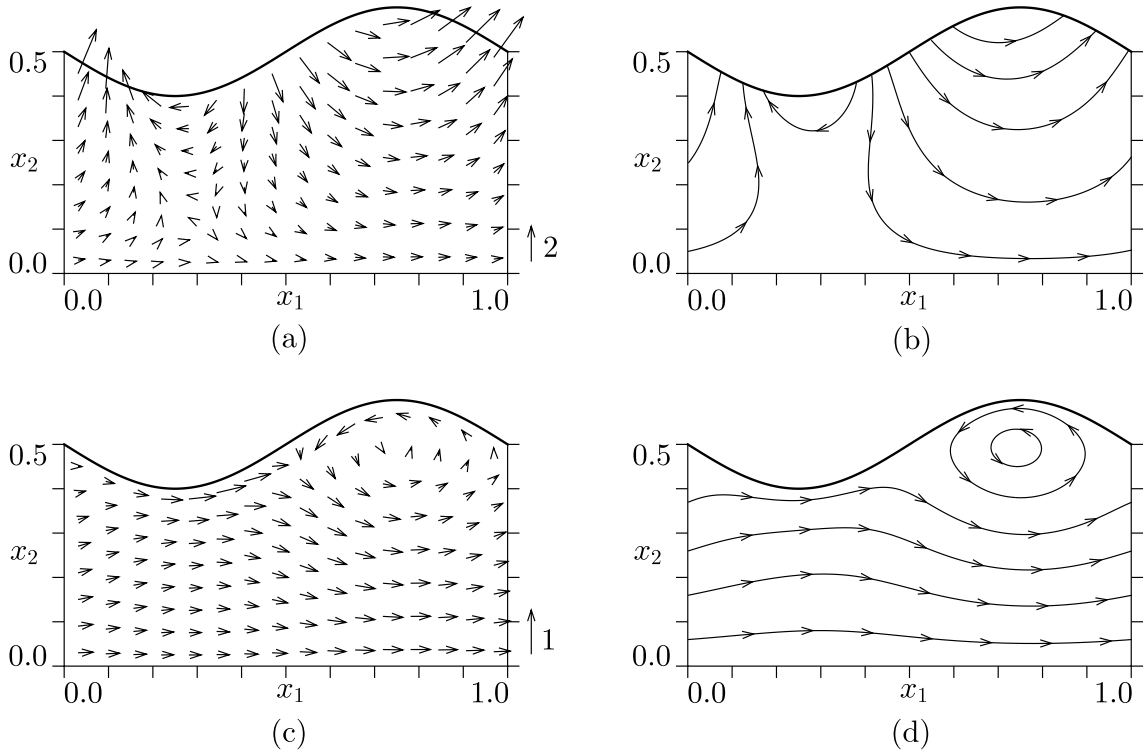

FIGURE 3.12: Flow velocity of individual gas components for isothermal walls of sinusoidal shape ($m^{\mathrm{B}}/m^{\mathrm{A}} = 5$, $d^{\mathrm{B}}/d^{\mathrm{A}} = 1$, $\hat{D} = 0.1$, $\hat{T}_{\mathrm{c}} = 0$, $\hat{n}_{\mathrm{c}}^{\mathrm{A}} = 0.5$, and $n_{\mathrm{av}}^{\mathrm{B}}/n_0 = 0.8$). (a) flow velocity field of $\hat{v}_{i(1)}^{\mathrm{A}}$, (b) streamlines of $\hat{v}_{i(1)}^{\mathrm{A}}$, (c) flow velocity field of $\hat{v}_{i(1)}^{\mathrm{B}}$, (d) streamlines of $\hat{v}_{i(1)}^{\mathrm{B}}$. In (a) and (c), the arrows indicate the vectors $\hat{v}_{i(1)}^{\mathrm{A}}$ and $\hat{v}_{i(1)}^{\mathrm{B}}$, respectively, and their scale are shown in the figures.

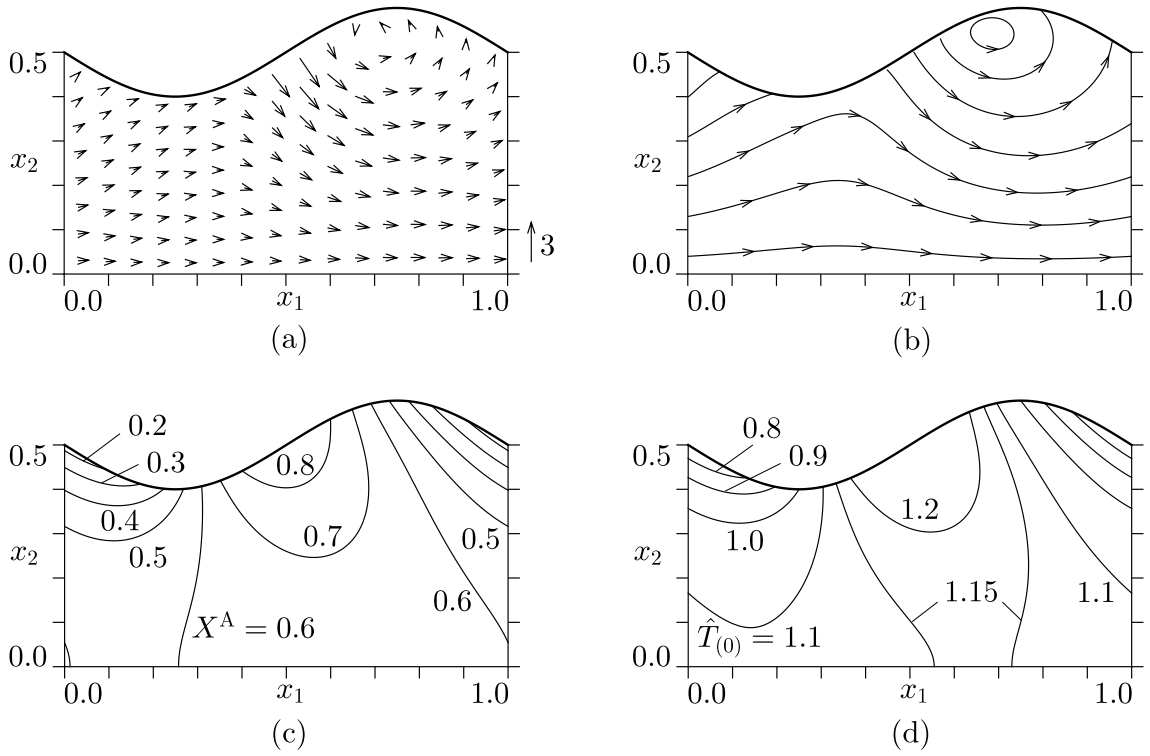

FIGURE 3.13: Flow field for non-isothermal walls of sinusoidal shape ($m^{\mathrm{B}}/m^{\mathrm{A}} = 5$, $d^{\mathrm{B}}/d^{\mathrm{A}} = 1$, $\hat{D} = 0.1$, $\hat{T}_{\mathrm{c}} = 0.3$, $\hat{n}_{\mathrm{c}}^{\mathrm{A}} = 0.5$, and $n_{\mathrm{av}}^{\mathrm{B}}/n_0 = 0.8$). (a) flow velocity field of $\hat{v}_{i(1)}$, (b) streamlines of $\hat{v}_{i(1)}$, (c) isolines of X^{A}, (d) isolines of $\hat{T}_{(0)}$. In (a), the arrow indicates the vector $\hat{v}_{i(1)}$, and its scale is shown in the figure.

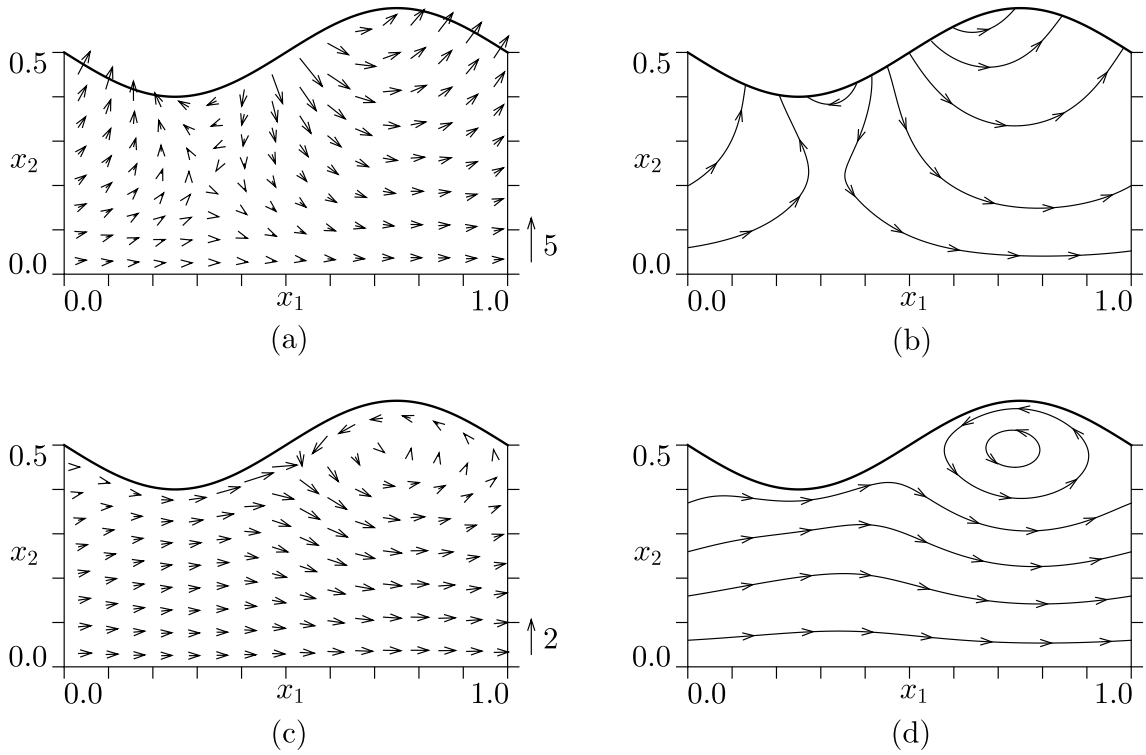

FIGURE 3.14: Flow field for non-isothermal walls of sinusoidal shape ($m^{\mathrm{B}}/m^{\mathrm{A}} = 5$, $d^{\mathrm{B}}/d^{\mathrm{A}} = 1$, $\hat{D} = 0.1$, $\hat{T}_{\mathrm{c}} = 0.3$, $\hat{n}_{\mathrm{c}}^{\mathrm{A}} = 0.5$, and $n_{\mathrm{av}}^{\mathrm{B}}/n_0 = 0.8$). (a) flow velocity field of $\hat{v}_{i(1)}^{\mathrm{A}}$, (b) streamlines of $\hat{v}_{i(1)}^{\mathrm{A}}$, (c) flow velocity field of $\hat{v}_{i(1)}^{\mathrm{B}}$, (d) streamlines of $\hat{v}_{i(1)}^{\mathrm{B}}$. In (a) and (c), the arrows indicate the vectors $\hat{v}_{i(1)}^{\mathrm{A}}$ and $\hat{v}_{i(1)}^{\mathrm{B}}$, respectively, and their scale are shown in the figures.

$0 \le x_1 \le 0.5$ and $0 \le x_2 \le 0.5$ with the specular reflection condition on $x_2 = 0$, $x_1 = 0$, and $x_1 = 0.5$. The DSMC method is explained in many places, so that we only show the results, omitting the description of the method.

Figures 3.15 and 3.16 contain the results for $m^{\mathrm{B}}/m^{\mathrm{A}} = 1$, $d^{\mathrm{B}}/d^{\mathrm{A}} = 1$, $\hat{n}_{\mathrm{c}}^{\mathrm{A}} = 0.5$, and $n_{\mathrm{av}}^{\mathrm{B}}/n_0 = 1$. Figure 3.15(a) shows the flow velocity vector magnified by the Knudsen number, i.e., $\hat{v}_i/\epsilon = (2/\sqrt{\pi})(\hat{v}_i/\mathrm{Kn})$, at $\mathrm{Kn} = 0.00625$ and the corresponding streamlines, and Fig. 3.15(b) the corresponding figure in the continuum limit, that is, $\lim_{\epsilon\to 0} \hat{v}_i/\epsilon = \hat{v}_{i(1)}$ obtained from the fluid-dynamic type system. Figure 3.15(c) shows the distribution of the normal component of the velocity, magnified by ϵ, i.e., $\hat{v}_2/\epsilon$, along the wall at $x_2 = 0.5$ for $\mathrm{Kn} = 0.1$, 0.05, 0.025, 0.0125, and 0.00625. In the figure, the result for the continuum limit, $\lim_{\epsilon\to 0} \hat{v}_2/\epsilon = \hat{v}_{2(1)}$, is also shown. Figure 3.16(a) shows the isolines of the concentration of the vapor, $\chi^{\mathrm{A}} = \hat{n}^{\mathrm{A}}/(\hat{n}^{\mathrm{A}}+\hat{n}^{\mathrm{B}})$, for $\mathrm{Kn} = 0.05$, 0.025, 0.0125, and 0.00625, together with the corresponding result in the continuum limit, $\lim_{\epsilon\to 0} \chi^{\mathrm{A}} = X^{\mathrm{A}}$. Figures 3.16(b) and 3.16(c) are, respectively, the distribution of the concentration of the vapor χ^{A} along $x_2 = 0.405$ and that along $x_2 = 0.105$ for $\mathrm{Kn} = 0.1$, 0.05, 0.025, 0.0125, and 0.00625. Figure 3.16(d) shows the average molecular number density of the vapor $n_{\mathrm{av}}^{\mathrm{A}}$ over the computational domain versus Kn. As is seen from Figs. 3.15 and 3.16, the DSMC result tends to approach the continuum limit obtained by the fluid-dynamic-type system as the Knudsen number becomes small. However, a closer look at Figs. 3.16(a) and 3.16(c) reveals that the speed of approach to the continuum limit is not monotonic near the center line ($x_2 = 0$). The curve in Fig. 3.16(d) also exhibits a slightly unnatural behavior for small Kn. Such behavior may be true physically. At the same time, we cannot exclude the possibility that it is attributed to insufficient accuracy of the DSMC computation. This point will be discussed below.

Figures 3.17–3.19 show the results for $m^{\mathrm{B}}/m^{\mathrm{A}} = 5$, $d^{\mathrm{B}}/d^{\mathrm{A}} = 1$, $\hat{n}_{\mathrm{c}}^{\mathrm{A}} = 0.5$, and $n_{\mathrm{av}}^{\mathrm{B}}/n_0 = 0.8$. Figure 3.17(a) shows the flow velocity vector magnified by the Knud-

sen number, i.e., $\hat{v}_i/\epsilon = (2/\sqrt{\pi})(\hat{v}_i/\mathrm{Kn})$, at Kn = 0.0125 and the corresponding streamlines, and Fig. 3.17(b) is the corresponding figure in the continuum limit, $\lim_{\epsilon\to 0} \hat{v}_i/\epsilon = \hat{v}_{i(1)}$, obtained by the fluid-dynamic type system. Figure 3.17(c) shows the distribution of the normal component of the velocity magnified by ϵ, i.e., $\hat{v}_2/\epsilon$, along the wall ($x_2 = 0.5$) for Kn = 0.1, 0.05, 0.025, and 0.0125, and Fig. 3.17(d) is the corresponding figure for the tangential component, i.e., $\hat{v}_1/\epsilon$. In the figures, the results for the continuum limit, $\lim_{\epsilon\to 0} \hat{v}_2/\epsilon = \hat{v}_{2(1)}$ and $\lim_{\epsilon\to 0} \hat{v}_1/\epsilon = \hat{v}_{1(1)}$, are also shown. Figure 3.18(a) shows the isolines of the concentration of the vapor, $\chi^{\mathrm{A}} = \hat{n}^{\mathrm{A}}/(\hat{n}^{\mathrm{A}}+\hat{n}^{\mathrm{B}})$, for Kn = 0.05, 0.025, and 0.0125, together with the corresponding result in the continuum limit, $\lim_{\epsilon\to 0} \chi^{\mathrm{A}} = X^{\mathrm{A}}$. Figures 3.18(b) and 3.18(c) are, respectively, the distribution of the concentration of the vapor χ^{A} along $x_2 = 0.405$ and that along $x_2 = 0.105$ for Kn = 0.1, 0.05, 0.025, and 0.0125. Figure 3.18(d) shows the average molecular number density of the vapor $n^{\mathrm{A}}_{\mathrm{av}}$ over the computational domain versus Kn. Figure 3.19 shows the distribution of the temperature $\hat{T}$ along $x_2 = 0.005$ at various Knudsen numbers. The tendency of approach of the DSMC result to the continuum limit based on the fluid-dynamic-type system is more or less similar to the previous case (Figs. 3.15 and 3.16). One thing to be stressed here is the fact that, as is clearly seen from Figs. 3.9(a) and 3.17, the DSMC velocity field does not approach the velocity field based on the Navier–Stokes system [the dashed line in Fig. 3.9(a)].

The aim of the present DSMC computation is to show that its results approach the continuum limit obtained by the correct fluid-dynamic-type system as the Knudsen number becomes small. As is well known, the DSMC method has difficulties for computation in the near continuum regime. However, in the present problem, additional and more serious difficulties associated with the ghost effect manifest themselves. As discussed in Sec. 3.3.C, when the Knudsen number is small, the density and temperature fields are affected by the flow velocity that is of the order of the Knudsen number

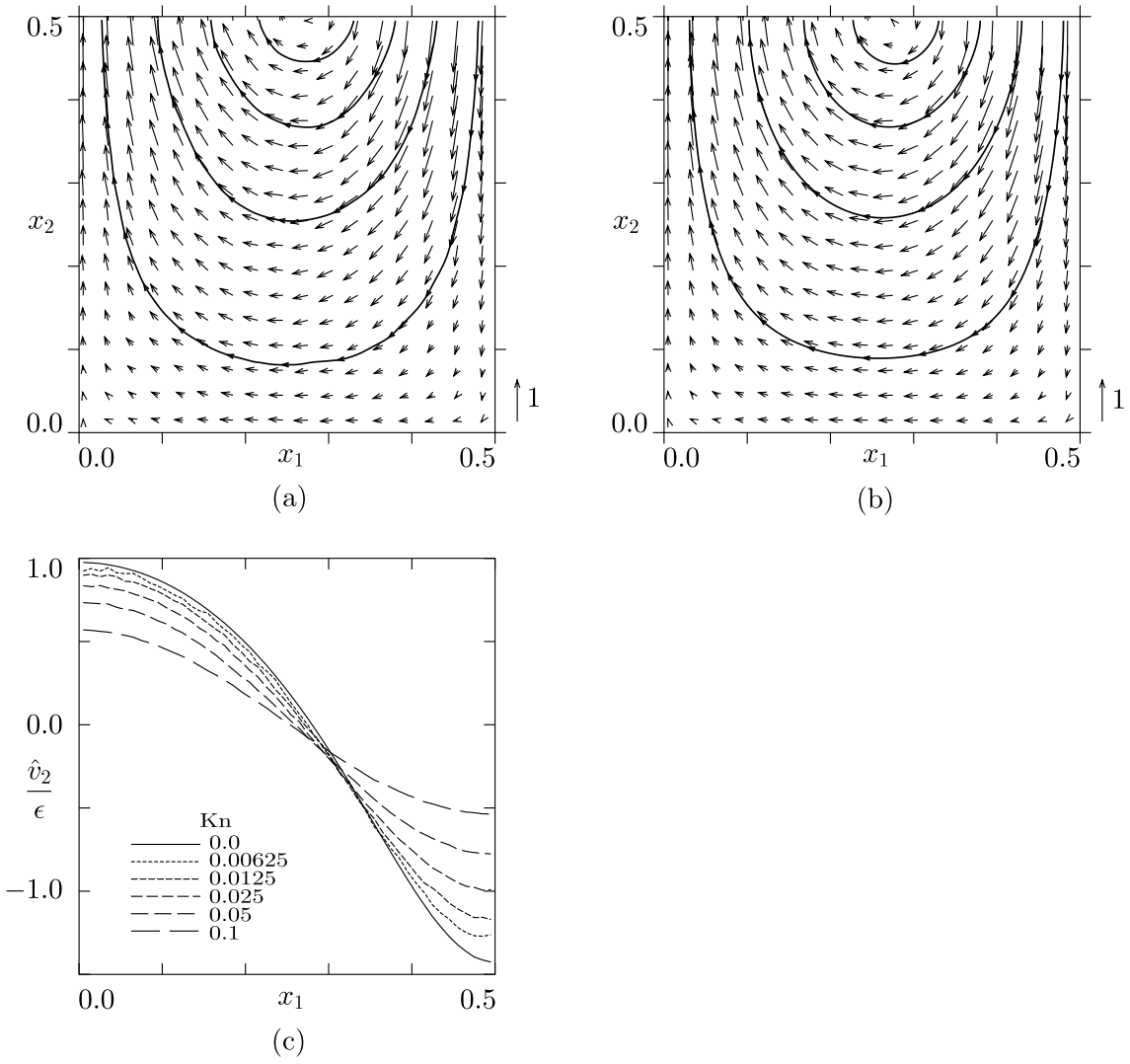

FIGURE 3.15: Comparison between the DSMC result and the continuum limit: barycentric flow velocity ($\hat{D} = \hat{T}_c = 0$, $m^B/m^A = d^B/d^A = 1$, $\hat{n}_c^A = 0.5$, and $n_{av}^B/n_0 = 1$). (a) $\hat{v}_i/\epsilon = (2/\sqrt{\pi})(\hat{v}_i/\mathrm{Kn})$ at $\mathrm{Kn} = 0.00625$, (b) $\hat{v}_{i(1)} = \lim_{\epsilon\to 0}(\hat{v}_i/\epsilon)$ obtained by the fluid-dynamic-type system, (c) distribution of $\hat{v}_2/\epsilon = (2/\sqrt{\pi})(\hat{v}_2/\mathrm{Kn})$ on the wall ($x_2 = 0.5$) at various Kn and the continuum limit $\hat{v}_{2(1)} = \lim_{\epsilon\to 0}(\hat{v}_2/\epsilon)$. In (a) and (b) the arrow indicates the vector $\hat{v}_i/\epsilon$ [(a)] or $\hat{v}_{i(1)} = \lim_{\epsilon\to 0}(\hat{v}_i/\epsilon)$ [(b)] at its starting point, and its scale is shown in the figures. The corresponding streamlines are also shown in the figures.

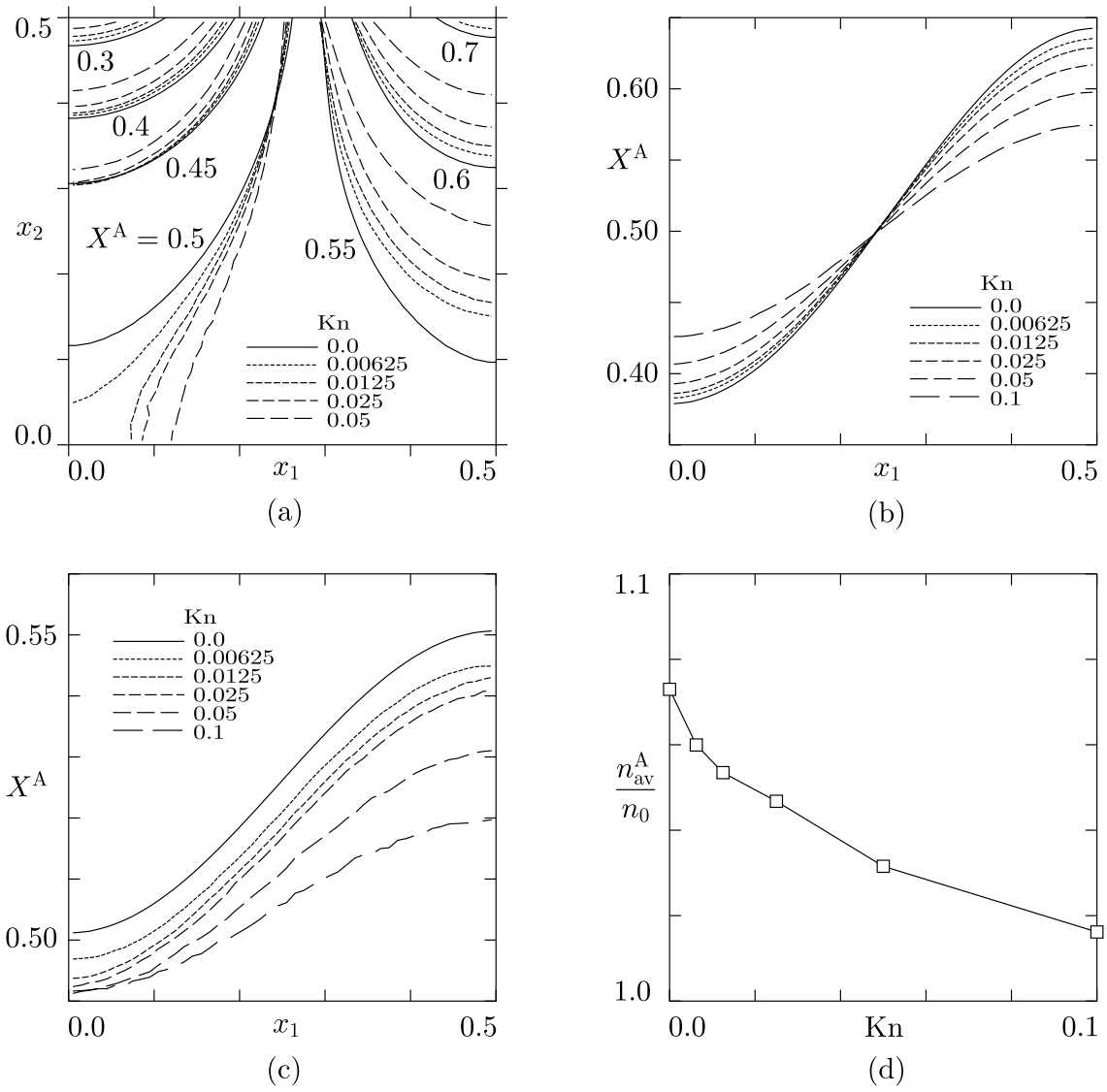

FIGURE 3.16: Comparison between the DSMC result and the continuum limit: concentration and average molecular number density of the vapor ($\hat{D} = \hat{T}_{\mathrm{c}} = 0$, $m^{\mathrm{B}}/m^{\mathrm{A}} = d^{\mathrm{B}}/d^{\mathrm{A}} = 1$, $\hat{n}^{\mathrm{A}}_{\mathrm{c}} = 0.5$, and $n^{\mathrm{B}}_{\mathrm{av}}/n_0 = 1$). (a) Isolines of the concentration of the vapor $\chi^{\mathrm{A}} = \hat{n}^{\mathrm{A}}/\hat{n}$ at various Kn including the continuum limit $\mathrm{Kn} \to 0$, (b) distribution of χ^{A} along $x_2 = 0.405$, (c) distribution of χ^{A} along $x_2 = 0.105$, (d) average molecular number density $n^{\mathrm{A}}_{\mathrm{av}}$ vs Kn.

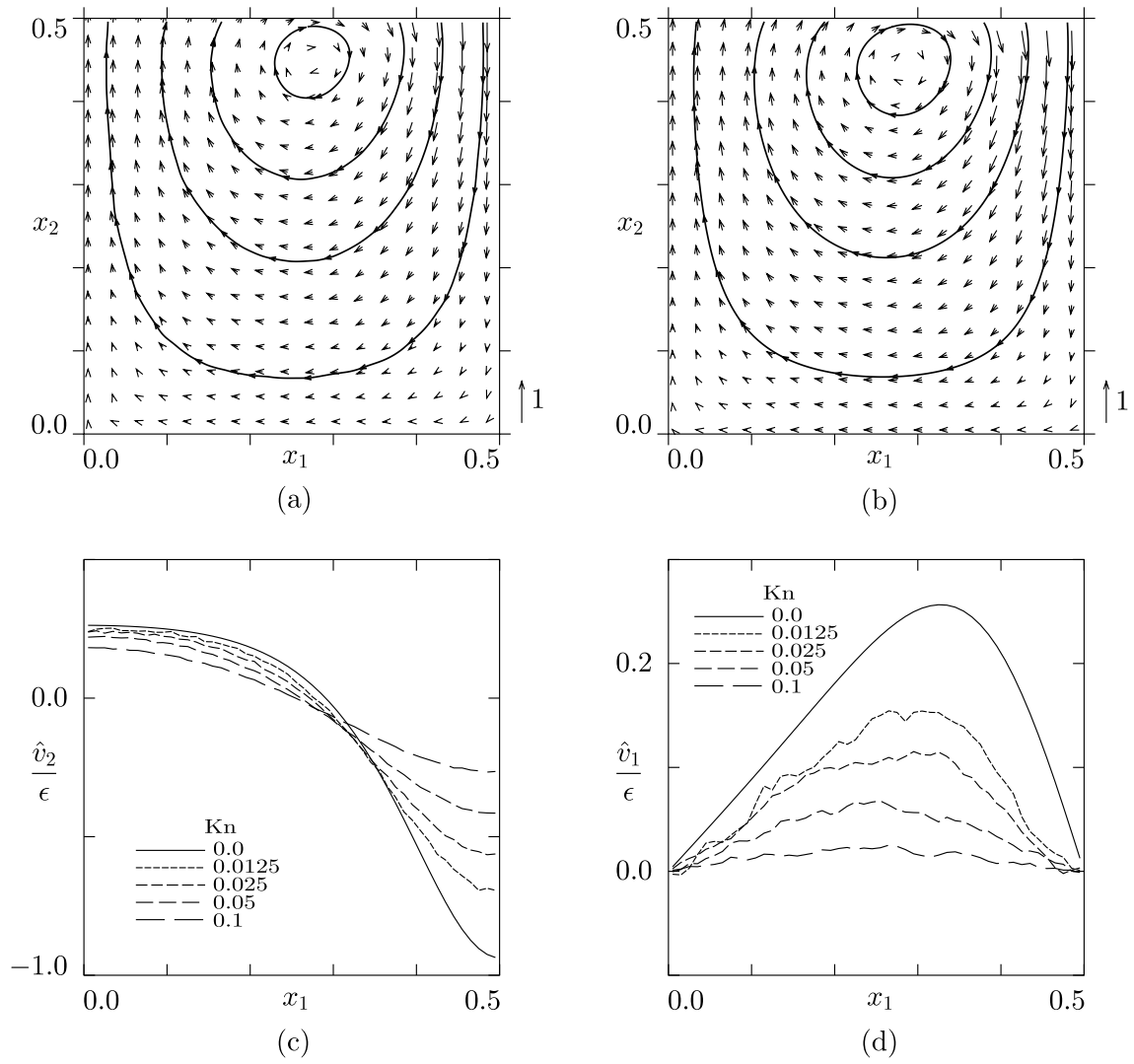

FIGURE 3.17: Comparison between the DSMC result and the continuum limit: barycentric flow velocity ($\hat{D} = \hat{T}_c = 0$, $m^B/m^A = 5$, $d^B/d^A = 1$, $\hat{n}_c^A = 0.5$, and $n_{av}^B/n_0 = 0.8$). (a) $\hat{v}_i/\epsilon = (2/\sqrt{\pi})(\hat{v}_i/\mathrm{Kn})$ at Kn = 0.0125, (b) $\hat{v}_{i(1)} = \lim_{\epsilon\to 0}(\hat{v}_i/\epsilon)$ obtained by the fluid-dynamic-type system, (c) distribution of $\hat{v}_2/\epsilon = (2/\sqrt{\pi})(\hat{v}_2/\mathrm{Kn})$ on the wall ($x_2 = 0.5$) at various Kn and the continuum limit $\hat{v}_{2(1)} = \lim_{\epsilon\to 0}(\hat{v}_2/\epsilon)$, (d) distribution of $\hat{v}_1/\epsilon = (2/\sqrt{\pi})(\hat{v}_1/\mathrm{Kn})$ on the wall ($x_2 = 0.5$) at various Kn and the continuum limit $\hat{v}_{1(1)} = \lim_{\epsilon\to 0}(\hat{v}_1/\epsilon)$. See the caption of Fig. 3.15. In (a) and (b) the arrow indicates the vector $\hat{v}_i/\epsilon$ [(a)] or $\hat{v}_{i(1)} = \lim_{\epsilon\to 0}(\hat{v}_i/\epsilon)$ [(b)] at its starting point, and the corresponding streamlines are also shown.

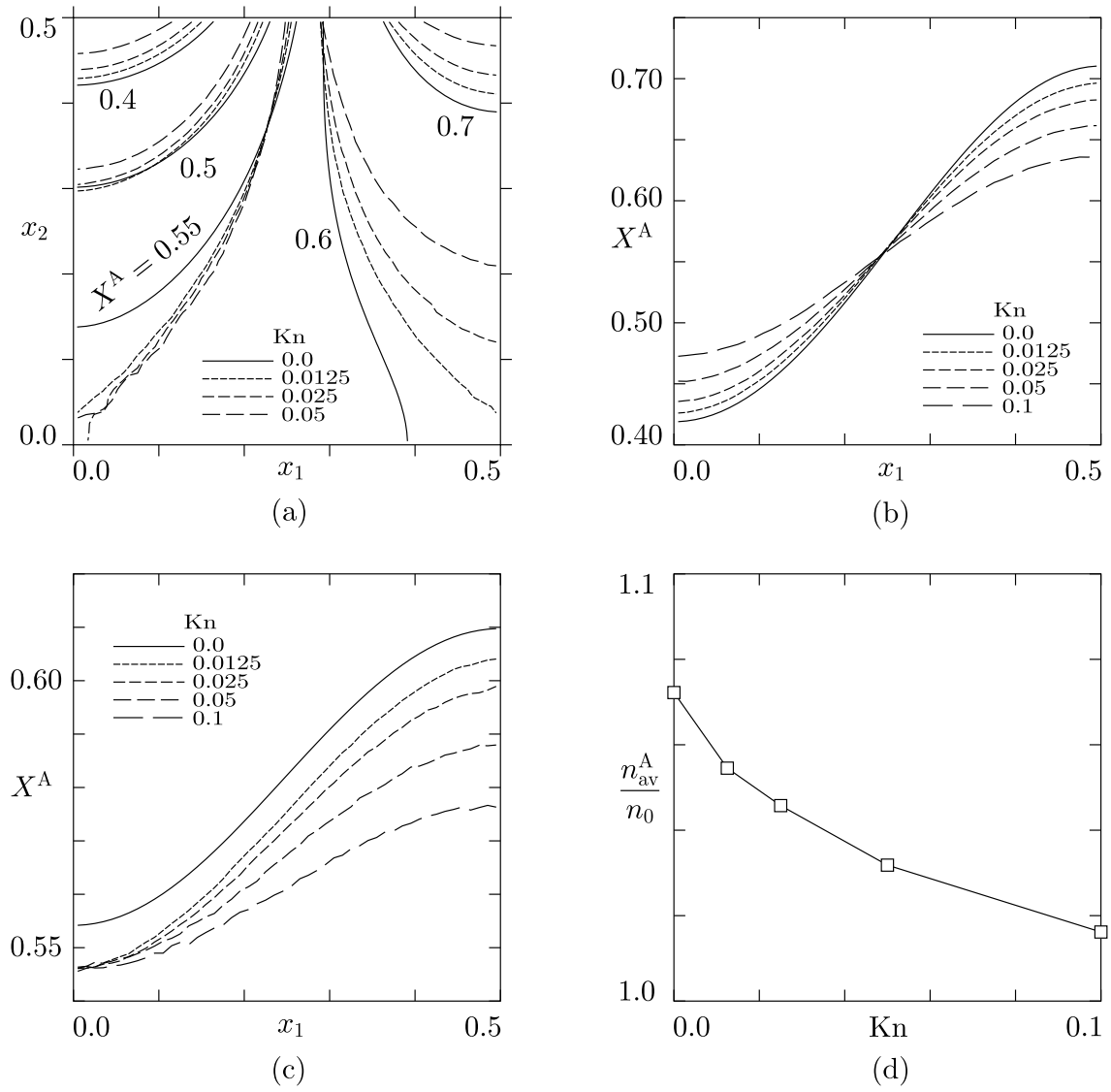

FIGURE 3.18: Comparison between the DSMC result and the continuum limit: concentration (or molecular number density) of the vapor ($\hat{D} = \hat{T}_c = 0$, $m^B/m^A = 5$, $d^B/d^A = 1$, $\hat{n}_c^A = 0.5$, and $n_{av}^B/n_0 = 0.8$). (a) Isolines of the concentration of the vapor $\chi^A = \hat{n}^A/\hat{n}$ at various Kn including the continuum limit Kn $\to 0$, (b) distribution of χ^A along $x_2 = 0.405$, (c) distribution of χ^A along $x_2 = 0.105$, (d) average molecular number density n_{av}^A vs Kn.

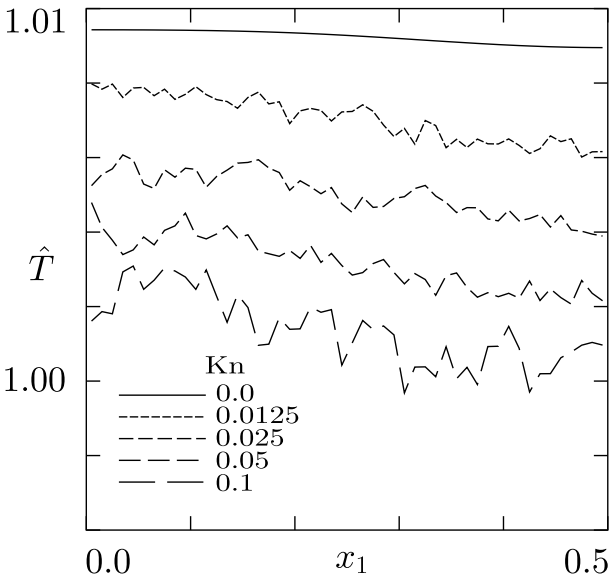

FIGURE 3.19: Comparison between the DSMC result and the continuum limit: temperature ($\hat{D} = \hat{T}_c = 0$, $m^B/m^A = 5$, $d^B/d^A = 1$, $\hat{n}_c^A = 0.5$, and $n_{av}^B/n_0 = 0.8$). The temperature $\hat{T}$ along $x_2 = 0.005$ is shown for various Kn including the continuum limit Kn $\to 0$.

and thus vanishes in the continuum limit. Therefore, in order to obtain reliable density and temperature fields by the DSMC method, we have to obtain the velocity field accurately in such a way that $\hat{v}_i^A/\mathrm{Kn}$, $\hat{v}_i^B/\mathrm{Kn}$, and $\hat{v}_i/\mathrm{Kn}$ are accurate enough. This requirement becomes increasingly difficult to fulfill as the Knudsen number approaches zero. In the present computation, the computational domain $0 \le x_1 \le 0.5$ and $0 \le x_2 \le 0.5$ is divided into 100×100 cells, and the average number of particles per cell in the final steady state is about 100 for the vapor and about 100 (or 80) for the noncondensable gas in the case of Figs. 3.15 and 3.16 (or Figs. 3.17–3.19). In the most difficult case of Kn = 0.00625 in Figs. 3.15 and 3.16, sixteen independent computations were carried out. The averages of necessary moments of the velocity distribution function are taken over 150×10^4 time steps, after a steady state seems to be established, for each of sixteen independent computations. Then, the averages of the sixteen time averages are regarded as the steady states of the moments. Each independent computation took 600 hours (including the time required to reach a steady

state) on a Pentium 4 3.6 GHz CPU. Other DSMC computations were carried out on a Dell Workstation running an Intel Pentium 4 2.2 GHz CPU.

As pointed out earlier, we cannot exclude the possibility that the approach to the continuum limit demonstrated in Figs. 3.16(a), 3.16(c), and 3.16(d) and in Figs. 3.18(a), 3.18(c), and 3.18(d), which seems to be slightly unnatural, is not true and is attributed to inaccuracy of the DSMC computation. However, noting the small scales of the ordinates in Figs. 3.16(c) and 3.18(c), one can claim that the present computation shows the approach to the continuum limit with a sufficient accuracy. In order to resolve the ambiguity, we need finer cells and more particles. However, such computation is quite hard with normally accessible computational environments. Keeping this in mind, we should stress that the fluid-dynamic-type system summarized in Sec. 3.3 is a very powerful and practical tool to deal with the problems described in Sec. 3.2.

3.6 Concluding remarks

In the present paper, we considered slow steady flows of a mixture of a vapor and a noncondensable gas, mainly caused by evaporation and condensation of the vapor, at small Knudsen numbers in the situation described in Sec. 3.2. A fluid-dynamic-type system that describes such flows was derived in Ref. [16] by a systematic asymptotic analysis for small Knudsen numbers on the basis of the Boltzmann system. However, the fluid-dynamic-type system could not be applied immediately to practical problems because it contained some coefficients whose numerical data were not available in the equations as well as the boundary conditions. Some years later, these coefficients were obtained numerically in separate papers,[24, 25] so that the fluid-dynamic-type system is now ready for application. One of the important purposes of the present paper was to summarize the fluid-dynamic-type system in a concise and usable form putting together the pieces of information obtained so far. This was done in Sec. 3.3 with the help of Appendices 3.7 and 3.8. Then in Sec. 3.4, we constructed a numerical solution

method for the fluid-dynamic-type system that is flexible for different geometries, with the help of the finite-volume method for the incompressible Navier–Stokes equations. The new method was applied to solving specific physical problems in Sec. 3.5, and the numerical results were discussed. Some results were also compared with the numerical results obtained from the original Boltzmann system by the DSMC method. As discussed in Sec. 3.5.C, because of the special structure of the physical situation under consideration, it becomes extremely hard to obtain a reliable result by the DSMC method as the Knudsen number decreases. Therefore, the fluid-dynamic-type system treated in the present paper is a powerful tool to analyze the flows of a mixture of a vapor and a noncondensable gas in the situation described in Sec. 3.2.

3.7 Appendix A: Transport coefficients and their database

In this appendix, we give the definitions of the transport coefficients occurring in Eqs. (3.5c)–(3.5e). In addition to α, other Greek letters β, γ, and κ will be used to indicate the labels A and B.

Let us denote by $A^\alpha(\zeta)$, $B^\alpha(\zeta)$, and $D^{(\beta)\alpha}(\zeta)$ the solutions of the following equations, where the independent variable ζ indicates the magnitude of a vector $(\zeta_1, \zeta_2, \zeta_3)$, i.e., $\zeta = (\zeta_i^2)^{1/2}$. That is, $A^\alpha(\zeta)$ is the solution of

$$\sum_{\beta=\mathrm{A,B}} \hat{K}^{\beta\alpha} X^\beta \widetilde{L}^{\beta\alpha}(\zeta_i A^\beta, \zeta_i A^\alpha) = -\zeta_i(\hat{m}^\alpha \zeta^2 - 5/2), \tag{3.41}$$

with the subsidiary condition

$$\sum_{\beta=\mathrm{A,B}} \hat{m}^\beta X^\beta I_4^\beta(A^\beta) = 0, \tag{3.42}$$

$B^\alpha(\zeta)$ is the solution of

$$\sum_{\beta=\mathrm{A,B}} \hat{K}^{\beta\alpha} X^\beta \widetilde{L}^{\beta\alpha}(c_{ij} B^\beta, c_{ij} B^\alpha) = -2\hat{m}^\alpha c_{ij}, \tag{3.43}$$

where

$$c_{ij} = \zeta_i\zeta_j - (1/3)\zeta^2\delta_{ij}, \tag{3.44}$$

and $D^{(\beta)\alpha}(\zeta)$ is the solution of

$$\sum_{\beta=\mathrm{A,B}} \hat{K}^{\beta\alpha} X^\beta X^\alpha \widetilde{L}^{\beta\alpha}(\zeta_i D^{(\gamma)\beta},\, \zeta_i D^{(\gamma)\alpha}) = -\zeta_i(\delta_{\alpha\gamma} - \hat{m}^\alpha \hat{n}^\alpha_{(0)}/\hat{\rho}_{(0)}), \tag{3.45}$$

with the subsidiary condition

$$\sum_{\beta=\mathrm{A,B}} \hat{m}^\beta X^\beta I_4^\beta(D^{(\alpha)\beta}) = 0. \tag{3.46}$$

Here,

$$\widetilde{L}^{\beta\alpha}(f,\, g) = [\hat{J}^{\beta\alpha}(fE^\beta,\, E^\alpha) + \hat{J}^{\beta\alpha}(E^\beta,\, gE^\alpha)](E^\alpha)^{-1}, \tag{3.47a}$$

$$\hat{J}^{\beta\alpha}(f,\, g) = \frac{1}{4\sqrt{2\pi}} \int [f(\zeta_{*i}^{\beta\alpha}) g(\zeta_i^{\beta\alpha}) - f(\zeta_{*i}) g(\zeta_i)]\, |e_j V_j|\, d\Omega(e_i)\, d^3\zeta_*, \tag{3.47b}$$

$$I_n^\alpha(F) = (8\pi/15) \int_0^\infty \zeta^n F(\zeta) E^\alpha(\zeta) d\zeta, \tag{3.47c}$$

$$E^\alpha(\zeta) = (\hat{m}^\alpha/\pi)^{3/2} \exp(-\hat{m}^\alpha \zeta^2), \tag{3.47d}$$

$$\zeta_i^{\beta\alpha} = \zeta_i + (\hat{\mu}^{\beta\alpha}/\hat{m}^\alpha)(e_j V_j) e_i, \tag{3.47e}$$

$$\zeta_{*i}^{\beta\alpha} = \zeta_{*i} - (\hat{\mu}^{\beta\alpha}/\hat{m}^\beta)(e_j V_j) e_i, \tag{3.47f}$$

$$V_i = \zeta_{*i} - \zeta_i, \tag{3.47g}$$

$$\hat{K}^{\beta\alpha} = [(\hat{d}^\beta + \hat{d}^\alpha)/2]^2, \tag{3.47h}$$

$$\hat{\mu}^{\beta\alpha} = 2\hat{m}^\beta \hat{m}^\alpha/(\hat{m}^\beta + \hat{m}^\alpha), \tag{3.47i}$$

$$d^3\zeta_* = d\zeta_{*1}\, d\zeta_{*2}\, d\zeta_{*3}. \tag{3.47j}$$

In Eq. (3.47b), which is the collision integral of the Boltzmann equation for a binary gas mixture, ζ_{*i} is the integration variable for ζ_i, e_i is the unit vector, $d\Omega(e_i)$ is

the solid-angle element in the direction of e_i, and the domain of integration is all the directions of e_i and the whole space of ζ_{*i}. The $\widetilde{L}^{\beta\alpha}$ is the linearized collision operator. Note that $\hat{\rho}_{(0)} = (\hat{m}^{\mathrm{A}} X^{\mathrm{A}} + \hat{m}^{\mathrm{B}} X^{\mathrm{B}})\hat{n}_{(0)}$ and $\hat{n}^{\alpha}_{(0)} = X^{\alpha}\hat{n}_{(0)}$. We should also recall that X^{A} and X^{B} are not independent ($X^{\mathrm{A}} + X^{\mathrm{B}} = 1$) and note that A^{α}, B^{α}, and $D^{(\beta)\alpha}$ depend on X^{A} (or X^{B}), $\hat{m}^{\alpha}$, and $\hat{d}^{\alpha}$.

Then we define the functions $A_1^{\alpha}(\zeta)$, $A_2^{\alpha}(\zeta)$, $D_1^{(\gamma,\kappa)\alpha}(\zeta)$, $D_2^{(\gamma,\kappa)\alpha}(\zeta)$, $D_{A1}^{(\gamma)\alpha}(\zeta)$, and $D_{A2}^{(\gamma)\alpha}(\zeta)$, which also depend on X^{A} (or X^{B}), $\hat{m}^{\alpha}$, and $\hat{d}^{\alpha}$, by the following integrals.

$$\zeta_i\zeta_j A_1^{\alpha} + A_2^{\alpha}\delta_{ij} = \sum_{\beta=\mathrm{A,B}} \hat{K}^{\beta\alpha} X^{\beta} \widetilde{J}^{\beta\alpha}(\zeta_i A^{\beta},\, \zeta_j A^{\alpha}), \tag{3.48}$$

$$\zeta_i\zeta_j D_1^{(\gamma,\kappa)\alpha} + D_2^{(\gamma,\kappa)\alpha}\delta_{ij} = \sum_{\beta=\mathrm{A,B}} \hat{K}^{\beta\alpha} X^{\beta} \widetilde{J}^{\beta\alpha}(\zeta_i D^{(\gamma)\beta},\, \zeta_j D^{(\kappa)\alpha}), \tag{3.49}$$

$$\zeta_i\zeta_j D_{A1}^{(\gamma)\alpha} + D_{A2}^{(\gamma)\alpha}\delta_{ij} = \sum_{\beta=\mathrm{A,B}} \hat{K}^{\beta\alpha} X^{\beta} [\widetilde{J}^{\beta\alpha}(\zeta_i A^{\beta},\, \zeta_j D^{(\gamma)\alpha}) + \widetilde{J}^{\beta\alpha}(\zeta_i D^{(\gamma)\beta},\, \zeta_j A^{\alpha})], \tag{3.50}$$

where

$$\widetilde{J}^{\beta\alpha}(f,\, g) = \hat{J}^{\beta\alpha}(fE^{\beta},\, gE^{\alpha})(E^{\alpha})^{-1}. \tag{3.51}$$

The transport coefficients are defined with the aid of the functions introduced above. The $\hat{\mu}$, $\hat{D}_{\mathrm{AB}}$, k_T, and $\hat{\lambda}$ are defined as follows:

$$\hat{\mu} = \sum_{\beta=\mathrm{A,B}} \hat{m}^{\beta} X^{\beta} I_6^{\beta}(B^{\beta}), \tag{3.52a}$$

$$\hat{D}_{\mathrm{AB}} = X^{\mathrm{A}} X^{\mathrm{B}} (\hat{\Delta}_{\mathrm{AA}} + \hat{\Delta}_{\mathrm{BB}} - \hat{\Delta}_{\mathrm{AB}} - \hat{\Delta}_{\mathrm{BA}}), \tag{3.52b}$$

$$k_T = \hat{D}_T / \hat{D}_{\mathrm{AB}}, \tag{3.52c}$$

$$\hat{\lambda} = \hat{\lambda}' - k_T \hat{D}_T / X^{\mathrm{A}} X^{\mathrm{B}}, \tag{3.52d}$$

where

$$\hat{\Delta}_{\alpha\beta} = \frac{5}{2} I_4^{\alpha}(D^{(\beta)\alpha}), \tag{3.53a}$$

$$\hat{D}_T = \frac{5}{2} X^{\mathrm{A}} X^{\mathrm{B}} [I_4^{\mathrm{A}}(A^{\mathrm{A}}) - I_4^{\mathrm{B}}(A^{\mathrm{B}})], \tag{3.53b}$$

$$\hat{\lambda}' = \frac{5}{2} \sum_{\beta=\mathrm{A,B}} X^{\beta} I_4^{\beta} \left((\hat{m}^{\beta}\zeta^2 - \frac{5}{2}) A^{\beta} \right). \tag{3.53c}$$

As mentioned in the second paragraph in Sec. 3.3.A, $\hat{\mu}$, $\hat{\lambda}$, and $\hat{D}_{\rm AB}$ correspond to the viscosity μ, thermal conductivity λ, and mutual-diffusion coefficient $D_{\rm AB}$, i.e., they are related as $\mu = (\sqrt{\pi}/2)(2kT_0/m_0)^{-1/2}\, p_0 l_0 \hat{T}_{(0)}^{1/2} \hat{\mu}$, $\lambda = (\sqrt{\pi}k/m_0)(2kT_0/m_0)^{-1/2} p_0 l_0 \hat{T}_{(0)}^{1/2} \hat{\lambda}$, and $D_{\rm AB} = (\sqrt{\pi}/2)(2kT_0/m_0)^{1/2} l_0 (\hat{T}_{(0)}^{1/2}/\hat{n}_{(0)}) \hat{D}_{\rm AB}$. The $\hat{D}_T$ corresponds to the thermal-diffusion coefficient D_T, i.e., $D_T = (\sqrt{\pi}/2)(2kT_0/m_0)^{1/2} l_0 \times (\hat{T}_{(0)}^{1/2}/\hat{n}_{(0)}) \hat{D}_T$. The $\hat{\Upsilon}_1$, $\hat{\Upsilon}_2$, $\hat{\Upsilon}_3$, $\hat{\Upsilon}_4$, and $\hat{\Upsilon}_5$ are defined by

$$\hat{\Upsilon}_1 = \frac{1}{2} \sum_{\beta={\rm A,B}} X^\beta I_6^\beta \left(B^\beta \left[A_1^\beta + (\hat{m}^\beta \zeta^2 - 3) A^\beta - \frac{\zeta}{2} \frac{\partial A^\beta}{\partial \zeta} \right] \right), \tag{3.54a}$$

$$\hat{\Upsilon}_2 = \frac{1}{2} \sum_{\beta={\rm A,B}} X^\beta I_6^\beta (A^\beta B^\beta), \tag{3.54b}$$

$$\hat{\Upsilon}_3 = \hat{\Upsilon}_3^{({\rm A,A})} + \hat{\Upsilon}_3^{({\rm B,B})} - \hat{\Upsilon}_3^{({\rm A,B})} - \hat{\Upsilon}_3^{({\rm B,A})}, \tag{3.54c}$$

$$\hat{\Upsilon}_4 = \hat{\Upsilon}_4^{({\rm A})} - \hat{\Upsilon}_4^{({\rm B})}, \tag{3.54d}$$

$$\hat{\Upsilon}_5 = \hat{\Upsilon}_5^{({\rm A})} - \hat{\Upsilon}_5^{({\rm B})}, \tag{3.54e}$$

where

$$\hat{\Upsilon}_3^{(\alpha,\gamma)} = \frac{1}{2} \sum_{\beta={\rm A,B}} X^\beta \times I_6^\beta \left(B^\beta D_1^{(\alpha,\gamma)\beta} - D^{(\alpha)\beta} \frac{\partial B^\beta}{\partial X^\gamma} \right), \tag{3.55a}$$

$$\hat{\Upsilon}_4^{(\alpha)} = \frac{1}{2} \sum_{\beta={\rm A,B}} X^\beta \times I_6^\beta \left(B^\beta \left[D_{A1}^{(\alpha)\beta} + (\hat{m}^\beta \zeta^2 - 2) D^{(\alpha)\beta} - \frac{\zeta}{2} \frac{\partial D^{(\alpha)\beta}}{\partial \zeta} \right] - A^\beta \frac{\partial B^\beta}{\partial X^\alpha} \right), \tag{3.55b}$$

$$\hat{\Upsilon}_5^{(\alpha)} = \frac{1}{2} \sum_{\beta={\rm A,B}} X^\beta I_6^\beta (B^\beta D^{(\alpha)\beta}). \tag{3.55c}$$

It should be noted that the partial derivatives of B^α with respect to the concentration $X^{\rm A}$ or $X^{\rm B}$ appear in Eq. (3.55). Their meaning is as follows. Since Eq. (3.43) is also

valid for $X^{\rm A}$ and $X^{\rm B}$ that are independent of each other, the solution B^α can be regarded as functions of two independent variables $X^{\rm A}$ and $X^{\rm B}$. We first take partial derivatives of such B^α and then introduce the restriction $X^{\rm A} + X^{\rm B} = 1$.

A database that gives accurate values of $\hat{\mu}$, $\hat{\lambda}$, $\hat{D}_{\rm AB}$, k_T, $\hat{\Upsilon}_1$, $\hat{\Upsilon}_2$, $\hat{\Upsilon}_3$, $\hat{\Upsilon}_4$, and $\hat{\Upsilon}_5$ immediately for any value of $X^{\rm A}$ in the case of $d^{\rm B}/d^{\rm A} = 0.5$, 1, and 2 and for many values of $m^{\rm B}/m^{\rm A}$, was constructed in Ref. [24]. The database is available from the present authors.

3.8 Appendix B: Slip coefficients and their database

The slip coefficients b_7 and b_9 contained in Eq. (3.8d) can be obtained by analyzing the two fundamental half-space boundary-value problems for the linearized Boltzmann equation for a binary gas mixture, that is, the thermal-slip (or thermal-creep) problem and the diffusion-slip problem. In Ref. [25], these problems were studied numerically on the basis of the linearized Boltzmann equation and the diffuse-reflection boundary condition. In the present study, the vapor molecules obey the boundary condition (iii) in Sec. 3.2, which is different from the diffuse reflection. However, the values of b_7 and b_9 are unchanged. In Ref. [25], these coefficients are expressed in the following form:

$$
\begin{aligned}
&b_7\ [= -b_I\ \text{(Ref. [25])}] \\
&= -\frac{1}{(\hat{m}^{\rm A} - \hat{m}^{\rm B})X^{\rm A} + \hat{m}^{\rm B}} \sum_{n=0}^{N} b_I^{(n)} T_n(2X^{\rm A} - 1), \qquad (3.56) \\
&b_9\ [= -b_{II}\ \text{(Ref. [25])}] \\
&= -\frac{1}{(\hat{m}^{\rm A} - \hat{m}^{\rm B})X^{\rm A} + \hat{m}^{\rm B}} \sum_{n=0}^{N} b_{II}^{(n)} T_n(2X^{\rm A} - 1), \qquad (3.57)
\end{aligned}
$$

where $T_n(x)$ is the Chebyshev polynomial defined by

$$
T_n(\cos\theta) = \cos n\theta, \qquad (3.58)
$$

for $0 \le \theta \le \pi$. The numerical values of $b_I^{(n)}$ and $b_{II}^{(n)}$ are tabulated for $m^{\rm B}/m^{\rm A} = 2$, 4, 5, and 10 and for $d^{\rm B}/d^{\rm A} = 1$ in Tables 3.1 and 3.2, which are taken from Ref. [25]. For $m^{\rm B}/m^{\rm A} = 1/2$, 1/4, 1/5, and 1/10 in the case of $d^{\rm B}/d^{\rm A} = 1$, the corresponding b_7 and b_9 are obtained from Tables 3.1 and 3.2 with the help of the following simple relation derived by interchanging the roles of A and B components: when $d^{\rm B}/d^{\rm A} = 1$,

$$b_7\left(X^{\rm A}, \frac{m^{\rm B}}{m^{\rm A}}\right) = b_7\left(1 - X^{\rm A}, \left(\frac{m^{\rm B}}{m^{\rm A}}\right)^{-1}\right)\left(\frac{m^{\rm B}}{m^{\rm A}}\right)^{-1/2}, \tag{3.59a}$$

$$b_9\left(X^{\rm A}, \frac{m^{\rm B}}{m^{\rm A}}\right) = -b_9\left(1 - X^{\rm A}, \left(\frac{m^{\rm B}}{m^{\rm A}}\right)^{-1}\right)\left(\frac{m^{\rm B}}{m^{\rm A}}\right)^{-1/2}. \tag{3.59b}$$

With Eqs. (3.56) and (3.57), we can obtain accurate values of b_7 and b_9 instantaneously for any $X^{\rm A}$.

TABLE 3.1: Coefficient $b_I^{(n)}$ $(n = 0, \ldots, N)$ in Eq. (3.56) for the thermal-slip coefficient b_7 for hard-sphere molecules $(d^{\rm B}/d^{\rm A} = 1)$.

	$m^{\rm B}/m^{\rm A}$			
n	2 (N=5)	4 (N=8)	5 (N=8)	10 (N=16)
0	7.63642(−1)[a]	9.17923(−1)	9.84826(−1)	1.27740
1	−1.32632(−1)	−3.17398(−1)	−3.92397(−1)	−6.90326(−1)
2	1.66396(−2)	5.12603(−2)	6.06550(−2)	6.84937(−2)
3	−1.25175(−3)	−5.74465(−3)	−7.00442(−3)	−8.19729(−3)
4	1.02588(−4)	5.45554(−4)	5.60533(−4)	−3.54147(−4)
5	−8.94758(−6)	−1.01207(−4)	−1.47912(−4)	−3.84175(−4)
6	–	8.14885(−6)	4.05181(−6)	−8.99259(−5)
7	–	−1.85388(−6)	−3.97989(−6)	−3.47191(−5)
8	–	1.63769(−7)	−1.31647(−7)	−1.14587(−5)
9	–	–	–	−4.32605(−6)
10	–	–	–	−1.59296(−6)
11	–	–	–	−5.67010(−7)
12	–	–	–	−1.86957(−7)
13	–	–	–	−8.23480(−8)
14	–	–	–	−4.14764(−8)
15	–	–	–	−1.55678(−8)
16	–	–	–	8.94466(−10)

[a] Read as 7.63642×10^{-1}.

TABLE 3.2: Coefficient $b_{II}^{(n)}$ $(n = 0, \ldots, N)$ in Eq. (3.57) for the diffusion-slip coefficient b_9 for hard-sphere molecules $(d^{\mathrm{B}}/d^{\mathrm{A}} = 1)$.

	$m^{\mathrm{B}}/m^{\mathrm{A}}$			
n	2 (N=8)	4 (N=12)	5 (N=12)	10 (N=16)
0	2.49793(−1)[a]	6.73235(−1)	8.66287(−1)	1.71982
1	5.31606(−2)	2.55179(−1)	3.68719(−1)	9.66600(−1)
2	4.27174(−3)	4.68653(−2)	8.07502(−2)	3.14293(−1)
3	5.14404(−4)	1.01504(−2)	2.00150(−2)	1.09560(−1)
4	4.72189(−5)	2.12351(−3)	4.94761(−3)	3.94440(−2)
5	5.62893(−6)	4.69641(−4)	1.26793(−3)	1.45152(−2)
6	5.54615(−7)	1.03165(−4)	3.27088(−4)	5.42339(−3)
7	6.63470(−8)	2.31888(−5)	8.56221(−5)	2.04847(−3)
8	6.74049(−9)	5.21745(−6)	2.25515(−5)	7.80244(−4)
9	–	1.18834(−6)	5.98659(−6)	2.99082(−4)
10	–	2.70543(−7)	1.60365(−6)	1.15247(−4)
11	–	6.44901(−8)	4.58402(−7)	4.46001(−5)
12	–	1.42769(−8)	1.14978(−7)	1.73405(−5)
13	–	–	–	6.77619(−6)
14	–	–	–	2.70263(−6)
15	–	–	–	1.19130(−6)
16	–	–	–	4.12502(−7)

[a] Read as 2.49793×10^{-1}.

3.9 Appendix C: Boundary conditions for binary mixtures of two noncondensable gases

In the case of two non-condensable gases, the boundary condition for the normal component of the barycentric flow velocity simply becomes that it should be equal to zero. On the other hand, in this case the concentration of the gases at the boundary is unknown. To obtain a boundary condition for X^{A} we note that equation (3.5e) with both velocity components set to zero implies that

$$\frac{\partial X^{\mathrm{A}}}{\partial x_i} = -\frac{k_T}{\hat{T}_{(0)}} \frac{\partial \hat{T}_{(0)}}{\partial x_i}, \tag{3.60}$$

so for a given temperature field the derivative of X^{A} normal to the wall is given by the above expression.

In this case we let the reference number density be the total amount of gas inside the domain. In other words $n_0 = n_{\rm av}$, which means that

$$\hat{p}_{(0)} = \left(\int \frac{1}{\hat{T}_{(0)}} \mathrm{d}V \right)^{-1} V. \tag{3.61}$$

We still need to specify the ratio of the different gas components. If we have specified $n^{\rm B}_{\rm av}/n^{\rm A}_{\rm av}$ then $\hat{p}_{(0)}$, $\hat{T}_{(0)}$ and $X^{\rm A}$ must satisfy

$$\frac{n^{\rm B}_{\rm av}}{n^{\rm A}_{\rm av}} = \frac{\int_V \hat{p}_{(0)} \hat{T}^{-1}_{(0)} (1 - X^{\rm A}) \mathrm{d}V}{\int_V \hat{p}_{(0)} \hat{T}^{-1}_{(0)} X^{\rm A} \mathrm{d}V}. \tag{3.62}$$

Given a concentration field $X^{\rm A*}$ we look for a constant correction $X^{\rm A\prime}$ so that $X^{{\rm A}m}$ satisfies Eq (3.62) for $\hat{T}^m_{(0)}$ and $\hat{p}^m_{(0)}$.

$$X^{\rm A\prime} = \frac{1}{1 + n^{\rm B}_{\rm av}/n^{\rm A}_{\rm av}} - \frac{1}{V} \int_V \frac{\hat{p}^m_{(0)}}{\hat{T}^m_{(0)}} X^{\rm A*} \mathrm{d}V. \tag{3.63}$$

References

[1] M. N. Kogan, "Kinetic theory in aerothermodynamics," Prog. Aerospace Sci. **29**, 271 (1992).

[2] T. Ytrehus, "Molecular-flow effects in evaporation and condensation at interfaces," Multiphase Science and Technology **9**, 205 (1997).

[3] C. Cercignani, *Rarefied Gas Dynamics: From Basic Concepts to Actual Calculations* (Cambridge Univ. Press, Cambridge, 2000).

[4] A. K. Rebrov, "Nonequilibrium processes at evaporating and condensing surfaces," in *Rarefied Gas Dynamics*, edited by T. J. Bartel and M. A. Gallis (AIP, Melville, 2001), p. 557.

[5] Y. Sone, *Kinetic Theory and Fluid Dynamics*, Modeling and Simulation in Science, Engineering and Technology (Birkhäuser, Boston, 2002).

[6] Y. Sone, *Molecular Gas Dynamics: Theory, Techniques, and Applications*, Modeling and Simulation in Science, Engineering and Technology (Birkhäuser, Boston, 2006).

[7] Y. Sone and Y. Onishi, "Kinetic theory of evaporation and condensation — Hydrodynamic equation and slip boundary condition —," J. Phys. Soc. Jpn. **44**, 1981 (1978).

[8] Y. Onishi and Y. Sone, "Kinetic theory of slightly strong evaporation and condensation — Hydrodynamic equation and slip boundary condition for finite Reynolds number —," J. Phys. Soc. Jpn. **47**, 1676 (1979).

[9] Y. Sone, "Asymptotic theory of a steady flow of a rarefied gas past bodies for small Knudsen numbers," in *Advances in Kinetic Theory and Continuum Mechanics*, edited by R. Gatignol and Soubbaramayer (Springer-Verlag, Berlin, 1991), p. 19.

[10] K. Aoki and Y. Sone, "Gas flows around the condensed phase with strong evaporation or condensation — Fluid dynamic equation and its boundary condition on the interface and their application —," in *Advances in Kinetic Theory and Continuum Mechanics*, edited by R. Gatignol and Soubbaramayer (Springer-Verlag, Berlin, 1991), p. 43.

[11] Y. Onishi, "Kinetic theory based nonlinear treatment for motions of a binary gas mixture involving slightly strong evaporation and condensation processes–A system of macroscopic equations, the boundary conditions and the Knudsen-layer corrections," Z. Angew. Math. Phys. **43**, 875 (1992).

[12] Y. Onishi, "Kinetic theory based nonlinear treatment for motions of a binary gas mixture involving slightly strong evaporation and condensation processes II–A system of macroscopic equations, the boundary conditions and the Knudsen-layer corrections," Z. Angew. Math. Phys. **44**, 828 (1993).

[13] K. Aoki, S. Takata, and S. Kosuge, "Vapor flows caused by evaporation and condensation on two parallel plane surfaces: Effect of the presence of a noncondensable gas," Phys. Fluids **10**, 1519 (1998).

[14] S. Takata, K. Aoki, and T. Muraki, "Behavior of a vapor-gas mixture between two parallel plane condensed phases in the continuum limit," in *Rarefied Gas Dynamics*, edited by R. Brun, R. Campargue, R. Gatignol, and J.-C. Lengrand (Cépaduès–Éditions, Toulouse, 1999), Vol. 1, p. 479.

[15] S. Takata and K. Aoki, "Two-surface problems of a multicomponent mixture of vapors and noncondensable gases in the continuum limit in the light of kinetic theory," Phys. Fluids **11**, 2743 (1999).

[16] S. Takata and K. Aoki, "The ghost effect in the continuum limit for a vapor-gas mixture around condensed phases: Asymptotic analysis of the Boltzmann equation," Transp. Theory Stat. Phys. **30**, 205 (2001); Erratum: Transp. Theory Stat. Phys. **31**, 289 (2002).

[17] K. Aoki, S. Takata, and S. Taguchi, "Vapor flows with evaporation and condensation in the continuum limit: Effect of a trace of noncondensable gas," Eur. J. Mech. B/Fluids **22**, 51 (2003).

[18] S. Taguchi, K. Aoki, and S. Takata, "Vapor flows in the continuum limit in the presence of a small amount of noncondensable gas," Phys. Fluids **16**, 4105 (2004).

[19] Y. Sone, K. Aoki, S. Takata, H. Sugimoto, and A. V. Bobylev, "Inappropriateness of the heat-conduction equation for description of a temperature field of a stationary gas in the continuum limit: Examination by asymptotic analysis and numerical computation of the Boltzmann equation," Phys. Fluids **8**, 628 (1996); Erratum: *ibid* **8**, 841 (1996).

[20] Y. Sone, "Continuum gas dynamics in the light of kinetic theory and new features of rarefied gas flows," in *Rarefied Gas Dynamics*, edited by C. Shen (Peking University Press, Beijing, 1997), p. 3.

[21] Y. Sone, "Flows induced by temperature fields in a rarefied gas and their ghost effect on the behavior of a gas in the continuum limit," Annu. Rev. Fluid Mech. **32**, 779 (2000).

[22] S. Chapman and T. G. Cowling, *The Mathematical Theory of Non-Uniform Gases*, 3rd Ed. (Cambridge University Press, Cambridge, 1995).

[23] V. S. Galkin, M. N. Kogan, and O. G. Fridlender, "Concentration-stress convection and the properties of slow flows of mixtures of gases," *Fluid Dyn.* **7**, 287 (1972).

[24] S. Takata, S. Yasuda, K. Aoki, and T. Shibata, "Various transport coefficients occurring in binary gas mixtures and their database," in *Rarefied Gas Dynamics*, edited by A. D. Ketsdever and E. P. Muntz (AIP, Melville, 2003), p. 106.

[25] S. Takata, S. Yasuda, S. Kosuge, and K. Aoki, "Numerical analysis of thermal-slip and diffusion-slip flows of a binary mixture of hard-sphere molecular gases," Phys. Fluids **15**, 3745 (2003).

[26] J. H. Ferziger, M. Perić, *Computational Methods for Fluid Dynamics*, Springer Verlag, Berlin, 2002.

[27] G. A. Bird, *Molecular Gas Dynamics* (Oxford University Press, Oxford, 1976).

[28] G. A. Bird, *Molecular Gas Dynamics and the Direct Simulation of Gas Flows* (Oxford University Press, Oxford, 1994).

[29] Y. Sone, "Asymptotic theory of flow of rarefied gas over a smooth boundary I," in *Rarefied Gas Dynamics*, edited by L. Trilling and H. Y. Wachman (Academic Press, New York, 1969), p. 243.

[30] Y. Sone, "Asymptotic theory of flow of rarefied gas over a smooth boundary II," in *Rarefied Gas Dynamics*, edited by D. Dini (Editrice Tecnico Scientifica, Pisa, Italy, 1971), Vol. II, p. 737.

[31] E. H. Kennard, *Kinetic Theory of Gases*, (McGraw-Hill, New York, 1938).

[32] Y. Sone, "Thermal creep in rarefied gas," J. Phys. Soc. Jpn. **21**, 1836 (1966).

[33] T. Ohwada, Y. Sone, and K. Aoki, "Numerical analysis of the shear and thermal creep flows of a rarefied gas over a plane wall on the basis of the linearized Boltzmann equation for hard-sphere molecules," Phys. Fluids A **1**, 1588 (1989).

[34] S. K. Loyalka, "Temperature jump and thermal creep slip: Rigid sphere gas," Phys. Fluids A **1**, 403 (1989).

[35] F. Sharipov and V. Seleznev, "Data on internal rarefied gas flows," J. Phys. Chem. Ref. Data **27**, 657 (1998).

[36] C. E. Siewert, "Viscous-slip, thermal-slip and temperature-jump coefficients as defined by the linearized Boltzmann equation and the Cercignani-Lampis boundary condition," Physics of Fluids **15**, 1696 (2003).

[37] C.-C. Chen, I.-K. Chen, T.-P. Liu, and Y. Sone, "Thermal transpiration for the linearized Boltzmann equation," Commn. Pure Appl. Math. **60**, 147 (2007).

[38] I. V. Volkov and V. S. Galkin, "Analysis of slip and temperature jump coefficients in a binary gas mixture," Fluid Dynamics **25**, 937 (1990).

[39] C. M. Huang, R. V. Tompson, T. K. Ghosh, I. N. Ivchenko, and S. K. Loyalka, "Measurements of thermal creep in binary gas mixtures," Phys. Fluids **11**, 1662 (1999).

[40] I. N. Ivchenko, S. K. Loyalka, and R. V. Tompson, "Boundary slip phenomena in a binary gas mixture," Z. Angew. Math. Phys. **53**, 58 (2002).

[41] F. Sharipov and D. Kalempa, "Velocity slip and temperature jump coefficients for gaseous mixtures. II. Thermal slip coefficient," Phys. Fluids **16**, 759 (2004).

[42] R. D. M. Garcia and C. E. Siewert, "The viscous-slip, diffusion-slip, and thermal-creep problems for a binary mixture of rigid spheres described by the linearized Boltzmann equation," Eur. J. Mech. B/Fluids (to be published).

[43] V. M. Zhdanov, "Theory of slip at the boundary of a gaseous mixture," Sov. Phys. Tech. Phys. **12**, 134 (1967).

[44] S. K. Loyalka, "Velocity slip coefficient and the diffusion slip velocity for a multicomponent gas mixture," Phys. Fluids **14**, 2599 (1971).

[45] S. Takata "Diffusion slip for a binary mixture of hard-sphere molecular gases: Numerical analysis based on the linearized Boltzmann equation," in *Rarefied Gas Dynamics*, edited by T. J. Bartel and M. A. Gallis (AIP, Melville, 2001), p. 22.

[46] F. Sharipov and D. Kalempa, "Velocity slip and temperature jump coefficients for gaseous mixtures. III. Diffusion slip coefficient," Phys. Fluids **16** 3779 (2004).

[47] Y. Sone, M. Handa, and T. Doi, "Ghost effect and bifurcation in a gas between coaxial circular cylinders with different temperatures," Phys. Fluids **15**, 2903 (2003).

[48] Y. Sone and T. Doi, "Ghost effect of infinitesimal curvature in the plane Couette flow of a gas in the continuum limit," Phys. Fluids **16**, 952 (2004).

[49] S. Takata, "Kinetic theory analysis of the two-surface problem of a vapor-vapor mixture in the continuum limit," Phys. Fluids **16**, 2182 (2004).

[50] H. Yoshida and K. Aoki, "Cylindrical Couette flow of a vapor-gas mixture: Ghost effect and bifurcation in the continuum limit," Phys. Fluids **18**, 087103 (2006).

[51] S. V. Patankar, D. B. Spalding, "A Calculation Procedure for Heat, Mass and Momentum Transfer in Three-dimensional Parabolic Flows," Int. J. Heat Mass Transfer, **15**, 1787 (1972).

[52] E. Saatdjian, *Transport Phenomena, Equations and Numerical Solutions* (John Wiley & Sons, Chichester, 2000).

[53] S. Muzaferija, "Adaptive finite volume method for flow predictions using unstructured meshes and multigrid approach," PhD Thesis, University of London, 1994.

[54] C. M. Rhie, W. L. Chow, "A numerical study of the turbulent flow past an isolated airfoil with trailing edge separation," AIAA J. **21**, 1525 (1983).

[55] R. B. Bird, W. E. Stewart, and E. N. Lightfoot, *Transport Phenomena*, 2nd edition (Wiley & Sons, New York, 2002).

[56] A. Tamir, Y. Taitel, and E. U. Schlünder, "Direct contact condensation of binary mixtures", Int. J. Heat Mass Transfer **17**, 1253 (1974).

[57] V. Srzic, H. M. Soliman, and S. J. Ormiston, "Analysis of laminar mixed-convection condensation on isothermal plates using the full boundary-layer equations: mixtures of a vapor and a lighter gas", Int. J. Heat Mass Transfer **42**, 685 (1999).

[58] E. C. Siow, S. J. Ormiston, and H. M. Soliman, "Two-phase modelling of laminar film condensation from vapour-gas mixtures in declining parallel-plate channels", Int. J. Thermal Sci. **46**, 458 (2007).

Conclusion

It has recently been demonstrated that there exists a discrepancy between the behaviour of a gas as predicted by conventional fluid-dynamics, and a description based on the kinetic theory of gases. The kinetic theory has a long history and although sometimes fallen out of favor, it has consistently proven its worth by providing straight-forward explanations to established physical phenomena and occasionally making startling predictions later proven correct. On the other hand, the customary approach typified by carelessly applying the Navier-Stokes equations to describe gas behaviour has questionable theoretical foundation remembering that on a microscopic level the continuum assumption does not accurately reflect reality.

The present study was built on the groundwork made over several decades by Sone and coworkers. It took as its starting point the fluid-dynamic-systems derived through systematic asymptotic analysis of the Boltzmann equation, describing the near-continuum slow flows of a gas or a mixture of gases under the influence of large variations in temperature. Noting the mathematical similarities with the incompressible Navier-Stokes equation, we constructed a general numerical solution method based on the finite volume method and the SIMPLE algorithm for pressure-linked equations. We showed applications, primarily connected to microflows with a small but finite Knudsen number, where a purely kinetic approach would carry with it daunting computational requirements. For a single-component gas we described how to construct micropumps without moving parts using thermal creep and channel geometry to induce one-way mass flows.

For a binary mixture of gases, for example consisting of a vapor and a noncondensable gas, the coupled set of partial differential equations is considerably more complicated, and had not previously been solved, in part due to the many transport

coefficients that cannot be written on explicit form, but must be obtained through time-consuming numerical computation. Recently, however, a numerical database has been made available allowing instant access to the values of the coefficient through the method of interpolation. Thus we were able to expand the numerical method for the single-component gas so that results could also be obtained for gas mixtures. We showed the validity of the solution method and the fluid-dynamic-type system itself by making comparison with DSMC computations.

Thus we can conclude that it is now possible to quickly obtain solutions of these fluid-mechanic-type systems describing slow steady gas flows in the near-continuum regime.

Acknowledgements

First of all, I would like to express my deep gratitude to my advisor Professor Kazuo Aoki, not only for his guidance and for letting me sample some of his great knowledge about kinetic theory and fluid dynamics, but also for creating the opportunity for me to come to Japan, and never failing to quickly find a solution to any problem I encountered during my stay. I would also like to thank Associate Professor Shigeru Takata for all his precious help and advice.

In addition, I want to thank my very considerate *senpai*, Dr. Masato Handa and Dr. Hiroaki Yoshida, for invaluable discussions about my research, and for their friendship. I'm also grateful to Kazuaki Hiwatashi and Hiroyasu Shimizu, for helping me overcome many of the everyday difficulties that life as a foreigner in Japan entails.

Finally, I would like to thank Li Shuyi, for being my sunshine whenever skies were gray.